COMBINING NATURAL AND SYNTHETIC MATERIALS TO PRODUCE MULTIFUNCTIONAL COMPOSITES

By

Mariana Desireé Reale Batista

A DISSERTATION

Submitted to
Michigan State University
in partial fulfillment of the requirements
for the degree of

Materials Science and Engineering – Doctor of Philosophy

2019

ABSTRACT

COMBINING NATURAL AND SYNTHETIC MATERIALS TO PRODUCE MULTIFUNCTIONAL COMPOSITES

By

Mariana Desireé Reale Batista

Synthetic fiber reinforced composites offer excellent mechanical properties and performance. However, due to the environment awareness and the growing requirement for fuel economy there is a growing urgency for combining a polymer with natural materials to create an eco-friendly composite that is also light-weight and low cost. This research investigates multiple ways of using cellulose fibers in applications ranging from composites for automotive applications to their use on electronic devices, so the broad potential of cellulose can be exploited.

The first investigation involves adding cellulose nanocrystals (CNCs) to a conventional carbon fiber-epoxy composite to simultaneously strengthen and toughen the composite. CNCs were functionalized with 3-aminopropyltriethoxysilane (APTES) and distributed at the interphase between a carbon fiber (CF) and an epoxy matrix. Stronger fiber/matrix adhesion was achieved by sizing CFs with a layer of epoxy, and further increase in interfacial shear strength (IFSS) was achieved by adding the functionalized CNCs (APTES-CNCs) at the interphase. Sizing CFs with APTES-CNCs at a concentration of 1.0 wt% resulted in 81% increase in IFSS compared to unsized CFs due to the establishment of covalent bonding and the stiffness of the interphase modulus.

Cellulose fibers were investigated at the macro scale when combined with inorganic reinforcements (glass fiber or talc) in a hybrid composite. Hybrid composites were injected molded with total fiber content kept constant at 30 wt% and the properties of the composites were characterized over 0–30 wt% of cellulose in a polypropylene (PP) matrix. Tensile, flexural and notched Izod impact tests revealed that in general the mechanical properties decreased with

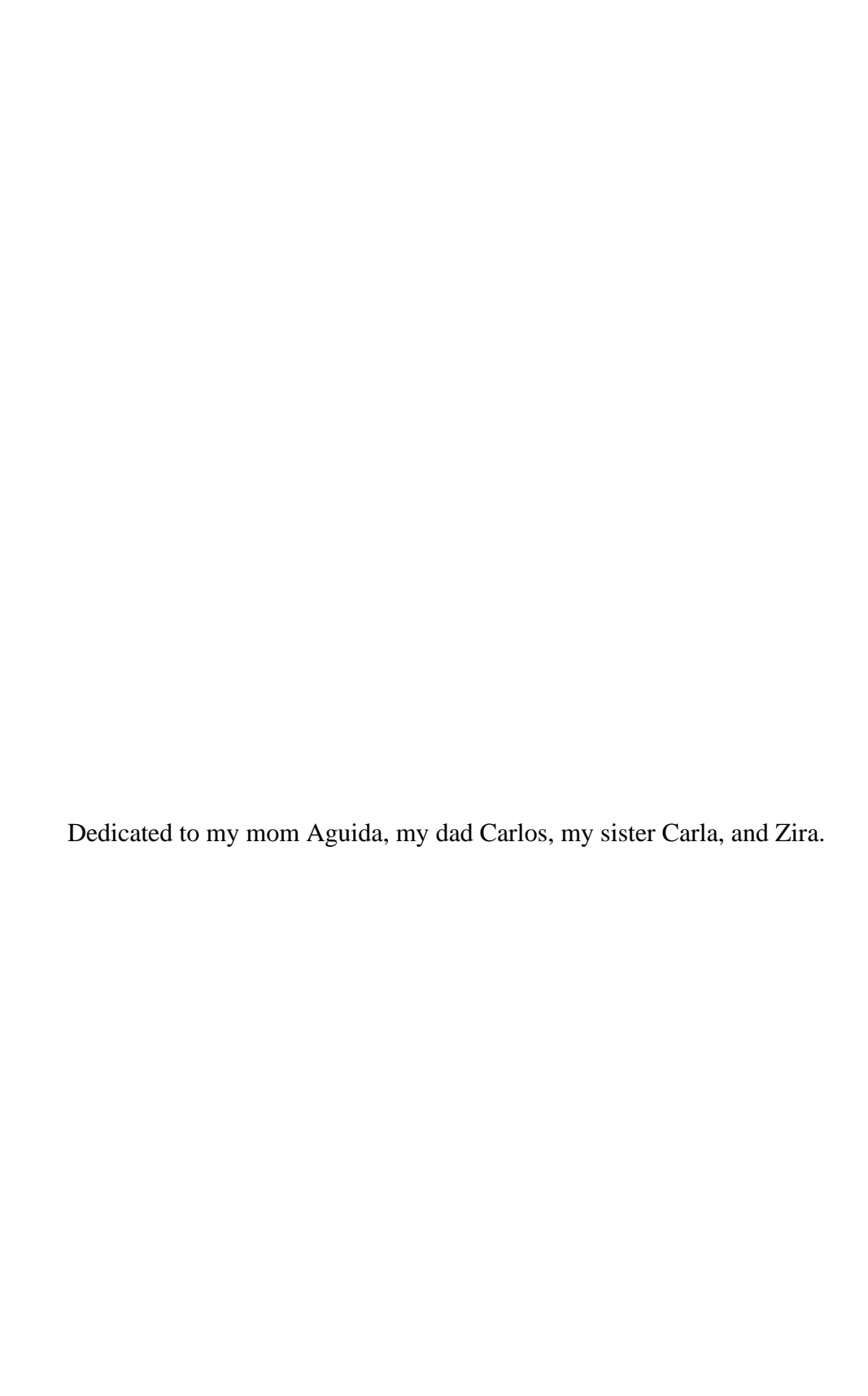
increasing cellulose content. The crystallization temperature (T_c) of the composites increased compared to neat PP, revealing the fibers ability to act as nucleating agents and speed rate of part production which will result in lowering the manufacturing cost. Overall, combining an optimum concentration of cellulose fiber with glass or talc is a promising alternative to reduce or replace the use of inorganic reinforcements on automotive under-the-hood and body interior components.

The use of cellulose fiber in electronic devices was investigated. Sensors to detect ultraviolet (UV) radiation were fabricated on a rigid glass substrate as well as on flexible substrates composed of cellulose fiber in the form of a paper or a polyimide film (PI). Carbon Nanotubes (CNTs) were drop-cast between the electrodes of the sensor on each substrate. All sensors respond immediately to UV On/Off cycles with a change in resistance due to the ability of CNTs to adsorb and desorb oxygen on their surface. Although the PI substrate yielded a sensor with the greater response, the cellulose paper proved to be effective to detect UV radiation, keeping its functionality even after being mechanically bent 1000 times, which is an advantage for practical applications.

The final project investigated the use of bamboo fibers (BFs) as the main reinforcement in a high-fiber volume fraction composite. Unidirectional long BF reinforced epoxy composites were made by compression molding and a process to surface treat the BF with sodium hydroxide (NaOH) was performed. Composites with 40v% NaOH modified BFs show a considerable increase of 29% for flexural modulus and 26% for flexural strength, compared to 40v% untreated BF reinforced composites. Coating the NaOH modified BF with Graphene Oxide (GO) resulted in composites with greater flexural properties, increasing modulus at 43% and strength at 29%.

This research has explored using cellulose fibers at both the nano and macro scales as an addition to synthetic fibers and also as a potential ecofriendly alternative to replace synthetic fiber in reinforced composites.

Copyright by MARIANA DESIREÉ REALE BATISTA 2019



ACKNOWLEDGEMENTS

There are many people that have made completing my graduate studies possible. I thank you Dr. Lawrence Drzal for being so patient with me and giving me all the guidance, encouragement and support to build on me confidence to finish my doctoral program. It has always been a pleasure learning from his experience. Thanks to my committee members Dr. Ramani Narayan, Dr. Mahmoodul Haq and Dr. K. Jayaraman for their advices and for their willingness to guide me.

Many thanks to the Coordenação de Aperfeiçoamento de Pessoal de Nível Superior (CAPES) for sponsoring the research conducted in this dissertation through the Brazil Scientific Mobility Program [99999.013655/2013-02]. I would like to thank NASA and Ford Motor Company for allowing me to improve my skills through internships. I am also grateful to the Agência Espacial Brasileira (AEB).

To all the CMSC research members, Per Askeland, Mike Rich, Brian Rook and Ed Drown who were always so helpful in discussing the projects and setting up the experiments. To the CHEMS office and the other graduate students at the CMSC who were there to support each other Zeyang, Markus, Nick, Keith, Yan, Dee. I am grateful for my friends, specially Erick, Lívia, Juliana, Thaís and Steven for the fun moments and for always supporting me. I also express my deepest gratitude to all the professors that taught me through my life.

Lastly, I am extremely thankful to my beloved parents, sister, David, Mirian, Adna and all my family who were always there to give me emotional support and for the care and guidance throughout my life. I am also thankful to God who gave me faith to finish this journey.

TABLE OF CONTENTS

LIST OF TABLES	X
LIST OF FIGURES	xi
CHAPTER 1: INTRODUCTION AND LITERATURE REVIEW	1
1.1 Introduction	
1.2 Motivation	
1.3 Significant research proposal	
1.3.1 Chapter 2: Carbon Fiber/Epoxy Matrix Composite Interphases Modified with	
Cellulose Nanocrystals	
1.3.2 Chapter 3: Hybrid Cellulose-Inorganic Reinforcement Polypropylene Compos	
Lightweight Materials for Automotive Applications	
1.3.3 Chapter 4: Flexible Ultraviolet Sensor based on Carbon Nanotubes	
1.3.4 Chapter 5: Surface Modification of Bamboo in Epoxy Composites	
1.4 Literature review	
1.4.1 Composite materials	
1.4.1 Composite materials	
1.4.2.1 Natural fiber treatments	
1.4.2.1 Natural fiber treatments	
· · · · · · · · · · · · · · · · · · ·	
1.4.4 Epoxy	
·	
1.4.5.1 Epoxy/amine curing	
1.4.6 Carbon fibers (CFs)	
1.4.6.1 Carbon fiber reinforced epoxy composites	
1.4.6.2 Fiber surface treatments	
1.4.6.3 Interphase tailoring via sizing or coating	
1.4.6.4 Functional interphase: effects of adding nanoparticles in the sizing	
1.4.7 Polypropylene (PP)	
1.4.8 Carbon Nanotubes (CNTs)	
REFERENCES	30
CHAPTER 2: CARBON FIBER/EPOXY MATRIX COMPOSITE INTERPHASES MOI	DIEIED
WITH CELLULOSE NANOCRYSTALS	
2.1 Abstract	
2.2 Introduction	
2.3 Experimental	
2.3.1 Materials	
2.3.2 Methods	
2.3.2.1 Surface treatment of CNCs	
2.3.2.2 Sizing of CFs with APTES-CNC	
2.3.2.3 Preparation of SFFT coupon	
2.3.3 Characterization methods	
2.3.3.1 Fourier transform infrared (FTIR) spectroscopy	45

2.3.3.2 X-ray photoelectron spectroscopy (XPS)	46
2.3.3.3 Scanning Electron Microscopy (SEM)	46
2.3.3.4 Single Fiber Fragmentation Test (SFFT)	
2.4 Results and discussion	
2.4.1 CNC surface modification with APTES	48
2.4.2 Characterization of APTES-CNC sized CFs	53
2.4.3 Evaluation of the IFSS by adding APTES-CNCs at the composite interphase	56
2.4.4 Interfacial failure mode analysis	
2.5 Conclusions	
REFERENCES	
CHAPTER 3: HYBRID CELLULOSE-INORGANIC REINFORCEMENT POLYPROPY	LENE
COMPOSITES: LIGHTWEIGHT MATERIALS FOR AUTOMOTIVE APPLICATIONS.	67
3.1 Abstract	67
3.2 Introduction	68
3.3 Experimental	69
3.3.1 Materials	69
3.3.2 Processing	
3.3.3 Testing procedure and characterization	
3.3.3.1 Mechanical test	
3.3.3.2 Scanning electron microscopy (SEM)	73
3.3.3.3 Thermal characterization	
3.4 Results and discussion	
3.4.1 Mechanical properties	
3.4.1.1 Tensile properties	
3.4.1.2 Flexural properties	
3.4.1.3 Impact properties	
3.4.2 Morphological properties	
3.4.3 Thermal properties	
3.4.3.1 Thermal Gravimetric Analysis (TGA)	
3.4.3.2 Differential Scanning Calorimetry (DSC)	
3.5 Conclusions	
REFERENCES	07
CHAPTER 4: FLEXIBLE ULTRAVIOLET SENSOR BASED ON CARBON NANOTUE	BES
	100
4.1 Abstract	100
4.2 Introduction	
4.3 Experimental section	
4.3.1 Materials	
4.3.2 Methods	
4.4 Results and discussion	
4.4.1 CNT distribution on sensor substrate	
4.4.2 Sensor response to UV light	
4.4.3 Sensor mechanical robustness	
4.4.4 Sensor response under natural sunlight	116

4.5 Conclusions	118
4.6 Acknowledgements	119
REFERENCES	120
CHAPTER 5: SURFACE MODIFICATION OF BAMBOO IN EPOXY COMPOSITES	123
5.1 Abstract	
5.2 Introduction	
5.3 Experimental	
5.3.1 Materials	
5.3.2 Methods	
5.3.2.1 Surface treatment of BFs with NaOH	
5.3.2.2 Surface treatment of NaOH modified BFs with GO	
5.3.2.3 Processing of unidirectional composites	
5.3.3 Characterization methods	
5.3.3.1 Scanning Electron Microscopy (SEM)	
5.3.3.2 X-ray photoelectron spectroscopy (XPS)	
5.3.3.3 Flexural test	
5.3.3.4 SBSS test	132
5.4 Results and discussion	132
5.4.1 Characterization of surface treated BFs	132
5.4.2 Mechanical properties of BF reinforced epoxy composites at 22 v%, 40 v% a	nd 50
v% BFs	
5.4.3 Mechanical properties of NaOH and NaOH/GO modified BF reinforced epox	кy
composites at 40 v% BFs	
5.4.4 SEM observation of composites fracture surface	144
5.4.5 Evaluation of the short beam strength	
5.5 Conclusions	
REFERENCES	150
CHAPTER 6: SUMMARY AND FUTURE WORK	154
6.1 Summary	
6.2 Future work	
6.2.1 Sizing CF with APTES-CNC	
6.2.2 Adding compatibilizer to hybrid composites	
6.2.3 Improving recovery time of UV sensors	
6.2.4 Increasing the concentration of GO on BF reinforced epoxy composites	

LIST OF TABLES

Table 1.1: Comparison between plant and synthetic fibers [12]
Table 1.2: Density and properties of some plant based fibers [7]
Table 1.3: EPON 828 properties [40]
Table 1.4: mPDA properties [43]
Table 1.5: Typical CF properties [48]
Table 2.1: O/C ratio and element composition in percent for CNC and APTES-CNC 51
Table 2.2: Relative amount of C1s components (%) for CNC and APTES-CNC
Table 2.3: Fiber fragment aspect ratio (l _c /d) and IFSS for 12k tow sized CFs
Table 2.4: Fiber fragment aspect ratio (l _c /d) and IFSS for individually sized CFs
Table 3.1: As received pellets compositions
Table 3.2: Sample identification codes and composite composition for each constituent source.71
Table 3.3: Enthalpies of crystallization for neat PP and composites
Table 3.4: Enthalpies of melting for neat PP and composites
Table 4.1: Roughness of CNT coated substrates by AFM (nm) on a 5 μm x 5 μm area 107
Table 4.2: Roughness of CNT coated substrates by AFM (nm) on a 1 μm x 1 μm area 108
Table 4.3: Resistance change (%) of sensors for varying radius of curvature
Table 5.1: Bamboo Fiber Material Specifications
Table 5.2: Composites composition and fiber surface treatment
Table 5.3: Percent element composition for BF, NaOH modified BF and NaOH/GO modified BF
Table 5.4: Relative amount of C1s components (%) for BF, NaOH modified BF and NaOH/GO modified BF

LIST OF FIGURES

Figure 1.1: Overview of the project discussed on Chapter 3
Figure 1.2: Simple scheme for the classification of composite materials [17]9
Figure 1.3: Stress—position profiles when fiber length (a) is equal to the critical length, (b) is greater than the critical length, and (c) is less than the critical length [17]
Figure 1.4: Molecular chain structure of cellulose [23]
Figure 1.5: MFA definition in the microstructure of plant cell wall together with cell wall sub-layers [7]
Figure 1.6: Number of publications related with nanocellulose [34]
Figure 1.7: Diglycidyl ether of bisphenol A (DGEBA) [41]
Figure 1.8: Structure of mPDA [43].
Figure 1.9: Three major reactions occurring in epoxy/amine systems [44]
Figure 1.10: FIB-SEM micrographs of CF from lower to higher magnification
Figure 1.11: Chemical structure of polypropylene [63]
Figure 1.12: Tacticity of polypropylene [63]
Figure 1.13: Schematic diagram of the chiral vector and the chiral angle [69]
Figure 1.14: Schematic illustrations of the structures of (A) armchair, (B) zigzag, and (C) chiral SWNTs [70]
Figure 2.1: Solvent exchange process using a rotary evaporator
Figure 2.2: Schematic illustration of the sizing process: a) 20s dipping of the 12k filament tow and b) 33 min immersion of metal frame with individual CFs
Figure 2.3: Schematic of preparation of the SFFT coupon
Figure 2.4: Schematic of preparation of the SFFT coupon
Figure 2.5: FTIR spectra for CNC, APTES-CNC (dried at RT for 24h) and APTES-CNC (dried at RT for 24h and at 120 °C for 2h)
Figure 2.6: XPS survey of (a) CNC and (b) APTES-CNC 50.

Figure 2.7: Deconvolution of C1s peak for (a) CNC and (b) APTES-CNC
Figure 2.8: FIB-SEM micrographs of a) unsized CF and b) epoxy-only sized CF
Figure 2.9: FIB-SEM micrographs for the 12k tow sizing technique of a) 0.6 wt% APTES-CNC sized CF, b) 1.0 wt% APTES-CNC sized CF and c) 2.0 wt% APTES-CNC sized CF
Figure 2.10: FIB-SEM micrographs for the individual sizing technique of a) 0.6 wt% APTES-CNC sized CF, b) 1.0 wt% APTES-CNC sized CF and c) 2.0 wt% APTES-CNC sized CF 56
Figure 2.11: IFSS for the a) 12k tow sized CFs and b) individually sized CFs
Figure 2.12: Transmitted light optical micrographs of the birefringence pattern at 20x and 50x for a) unsized CF, b) epoxy-only sized CF and 12k tow sized CF at c) 0.6 wt% APTES-CNC, d) 1.0 wt% APTES-CNC and e) 2.0 wt% APTES-CNC.
Figure 3.1: Schematic illustration of materials, processing and characterization
Figure 3.2: Schematic illustration of SEM analysis
Figure 3.3: Tensile stress at maximum load of a) LGF/Cellulose A, b) (SGF/Mica)/Cellulose B, c) Talc/Cellulose B and d) SGF/Cellulose B composites along with neat PP77
Figure 3.4: Young's modulus of a) LGF/Cellulose A, b) (SGF/Mica)/Cellulose B, c) Talc/Cellulose B and d) SGF/Cellulose B composites along with neat PP
Figure 3.5: Tensile strain at maximum load of a) LGF/Cellulose A, b) (SGF/Mica)/Cellulose B, c) Talc/Cellulose B and d) SGF/Cellulose B composites along with neat PP
Figure 3.6: Stress at 5% strain of a) LGF/Cellulose A, b) (SGF/Mica)/Cellulose B, c) Talc/Cellulose B and d) SGF/Cellulose B composites along with neat PP. *Specimens broke before 5% strain; maximum stress value used
Figure 3.7: Flexural modulus of a) LGF/Cellulose A, b) (SGF/Mica)/Cellulose B, c) Talc/Cellulose B and d) SGF/Cellulose B composites along with neat PP
Figure 3.8: Impact strength of a) LGF/Cellulose A, b) (SGF/Mica)/Cellulose B, c) Talc/Cellulose B and d) SGF/Cellulose B composites along with neat PP
Figure 3.9: SEM micrographs of a) Neat PP X, b) LGF/Cellulose A (30/0), c) LGF/Cellulose A (15/15) and d) LGF/Cellulose A (0/30)
Figure 3.10: SEM micrographs of a) Neat PP Y, b) (SGF/Mica)/Cellulose B (30/0), c) (SGF/Mica)/Cellulose B (15/15) and d) (SGF/Mica)/Cellulose B (0/30)
Figure 3.11: SEM micrographs of a) Neat PP Y, b) Talc/Cellulose B (30/0), c) Talc/Cellulose B (15/15) and d) Talc/Cellulose B (0/30)

Figure 3.12: SEM micrographs of a) Neat PP Z, b) SGF/Cellulose B (30/0), c) SGF/Cellulose B (15/15) and d) SGF/Cellulose B (0/30)	
Figure 3.13: SEM micrographs of a) 30wt. % Cellulose A and b) 30wt. % Cellulose B	88
Figure 3.14: Temperature at the maximum rate of decomposition determined from DTG curves for a) LGF/Cellulose A, b) (SGF/Mica)/Cellulose B, c) Talc/Cellulose B and d) SGF/Cellulose composites along with neat PP.	e B
Figure 3.15: Temperature at 1% weight loss from TGA curves for a) LGF/Cellulose A, b) (SGF/Mica)/Cellulose B, c) Talc/Cellulose B and d) SGF/Cellulose B composites along with neat PP.	90
Figure 3.16: Temperature at 10% weight loss from TGA curves for a) LGF/Cellulose A, b) (SGF/Mica)/Cellulose B, c) Talc/Cellulose B and d) SGF/Cellulose B composites along with neat PP.	91
Figure 3.17: Residual weight percent at 587 °C from TGA curves for a) LGF/Cellulose A, b) (SGF/Mica)/Cellulose B, c) Talc/Cellulose B and d) SGF/Cellulose B composites along with neat PP.	92
Figure 3.18: Crystallization and melting temperatures for a) LGF/Cellulose A, b) (SGF/Mica)/Cellulose B, c) Talc/Cellulose B and d) SGF/Cellulose B composites	93
Figure 4.1: Sensor structure and test set up.	104
Figure 4.2: SEM micrographs of CNT coated a) PI, b) glass and c) cellulose paper substrate at higher (top) and lower (bottom) magnification.	
Figure 4.3: Height (top) and amplitude (bottom) profile of CNT coated a) PI, b) glass and c) cellulose paper substrate by AFM on a 5 µm x 5 µm area	107
Figure 4.4: Height (top) and amplitude (bottom) profile of CNT coated a) PI, b) glass and c) cellulose paper substrate by AFM on a 1 μ m x 1 μ m area.	108
Figure 4.5: Response of sensors under UV illumination.	109
Figure 4.6: Resistance change of sensors under UV On/Off cycling	110
Figure 4.7: Response under UV illumination as a function of CNT weight percent on PI substrate.	112
Figure 4.8: Resistance change as a function of power density under On/Off cycle for PI substra	
Figure 4.9: Mechanical bending test with varying radius of curvature	l 14
Figure 4.10: Bending cycle test at a curvature radius of 10 mm (conditioning step)	115

Figure 4.11: UV response of the conditioned a) PI and b) cellulose paper sensors under flat and 10 mm bending state
Figure 4.12: a) Design of electrodes and b) printing on PI substrate for c) potential application on sunglasses and wristband
Figure 4.13: Resistance change of UV sensor on wristband under sunlight
Figure 5.1: SEM of polished surface of cross section of bamboo fiber bundle embedded in epoxy
Figure 5.2: (a) Young's modulus, (b) tensile strength and (c) IFSS of untreated, GO-treated, and Graphene flake-coated jute fibers [6].
Figure 5.3: Processing of BF reinforced epoxy composite
Figure 5.4: SEM images of the surface of (a) BFs, (b) NaOH modified BFs and (c) NaOH/GO modified BFs, top is lower magnification (377X) and bottom is higher magnification (9000X).
Figure 5.5: XPS survey of (a) BF, (b) NaOH modified BF and (c) NaOH/GO modified BF 135
Figure 5.6: Deconvolution of C1s peak for (a) BF, (b) NaOH modified BF and (c) NaOH/GO modified BF
Figure 5.7: (a) Flexural modulus, (b) flexural strength and (c) flexural strain along the fiber longitudinal direction for neat epoxy and epoxy composites reinforced at 22 v%, 40 v% and 50 v% BF.
Figure 5.8: (a) Flexural modulus, (b) flexural strength and (c) flexural strain along the fiber longitudinal direction for epoxy composites reinforced at 40 v% BF, 40 v% NaOH modified BF and 40 v% NaOH/GO modified BF
Figure 5.9: Flexural fracture surface for epoxy composites reinforced at (a) 40 v% BF, (b) 40 v% NaOH modified BF and (c) 40 v% NaOH/GO modified BF, top is lower magnification (177X) and bottom is higher magnification (2500X).
Figure 5.10: Flexural fracture surface for epoxy composites reinforced at 40 v% BF 145
Figure 5.11: Flexural fracture surface for epoxy composites reinforced at 40 v% NaOH modified BF
Figure 5.12: Flexural fracture surface for epoxy composites reinforced at 40 v% NaOH/GO modified BF
Figure 5.13: Short beam strength for epoxy composites reinforced at 40 v% BF, 40 v% NaOH modified BF and 40 v% NaOH/GO modified BF

CHAPTER 1: INTRODUCTION AND LITERATURE REVIEW

1.1 Introduction

For decades synthetic fibers, such as petroleum-based fibers have been the subject of much research, development and application. Although synthetic fibers, like carbon fiber and glass fiber, can produce composites with excellent mechanical properties, they consume high energy during production, they are abrasive to the processing machinery and they contribute to a large amount of carbon dioxide (CO₂) emission during production [1]. In addition, petroleum-based fibers are made from materials that will become heavily depleted over time and are non-biodegradable. Composite materials made from these synthetic fibers are also difficult to recycle since the separation of the constituents at end of life is not easy, which can result in disposal in landfills or by incineration [2]. In this context, there is a growing urgency to develop biomaterials, such as with plant-based fibers, as a means to decrease the environmental threat and dependence on fossil fuel.

Natural fibers are obtained from plants, animals or minerals [3] and have been used in various applications such as building materials, insulation boards, animal feed, cosmetics, medicine and fine chemicals [4]. The natural fibers discussed on this dissertation are plant-based, consisting mainly of cellulose, hemicellulose and lignin with lesser amounts of other components [5], and will be termed in this study as cellulose fibers. There is a variety of plant-based natural fibers of which bamboo, jute, sisal, hemp, cotton, palm, flax and ramie have found practical uses. CO₂ neutrality after burning, abundant availability, sustainable nature and non-abrasiveness to the processing equipment [6] are some of the cellulose fibers promising benefits that make them attractive for a broad range of applications.

Plant-based fibers are attracting considerable attention as reinforcements for polymer composites owing to their low cost, low density and high mechanical properties [7]. Their low density at about 1.15-1.50 g/cm³ versus 2.5 g/cm³ for glass fiber [8] is attractive for automotive, aerospace and sports applications. Reducing a vehicle's weight by 10 % can improve the fuel economy by 3 to 7 % [9] and contribute to attaining the CAFE standards. Therefore, the usage of plant-based fibers in the automotive industry is a central strategy for meeting light-weighting and fuel economy standards. The idea of using bio-based materials in vehicle parts was first introduced by Ford Motor Company in early 1930s [10] and nowadays natural fibers are being considered as replacements for synthetic fibers in different components, such as door and instrument panels, armrests, headrests and seat shells [4]. They also potentially could exhibit advantages in terms of cost. Natural fiber reinforced composites are viable replacements for glass reinforced composites in automotive applications since their use reduces the use of expensive glass fibers (\$0.50/kg versus \$3.25/kg) [8] and they have attractive properties such as better impact resistance that is essential for vehicles [11].

1.2 Motivation

Cellulose fibers are increasingly and successfully being used in a large range of applications. The global natural fiber composite market reached \$2.1 billion in 2010 [7] and many natural fiber composite products have been developed. However, despite their advantages and usage in load-bearing components, the industrial uptake of natural fiber reinforced polymers in high-level structural applications has been limited [12]. Efforts need to be taken to promote their usage as the primary structural components of structures such as in aerospace and maritime applications [13]. According to Shah [12], over 95% of natural fiber composites in Europe are applied in vehicles as non-structural components. One reason is the higher mechanical properties

of synthetic fibers compared to natural fibers, as shown on Table 1.1, which makes the synthetic fibers preferable in some applications.

Table 1.1: Comparison between plant and synthetic fibers [12].

Properties	Plant fiber	Glass fiber	Carbon fiber
Tensile stiffness (GPa)	Moderate (~30 – 80)	Moderate (70 – 85)	High (150 – 500)
Tensile strength (GPa)	Low (~0.4 – 1.5)	Moderate (2.0 – 3.7)	High (1.3 – 6.3)

Considering the potential and beneficial properties of cellulose, more research needs to be directed in this path, so the real potential of natural fibers can be exploited. This study shows that cellulose fibers can effectively reinforce polymer composites as a potential ecofriendly alternative to synthetic fiber reinforced composites and be used in combination with synthetic fibers. This work investigates ways how cellulose fibers can be used with or instead of synthetic fibers in polymer composites. In this sense we investigate cellulose fiber at its macro and nano scale and how they can reinforce different polymer matrices such as thermosetting (epoxy) and thermoplastic (polypropylene). The contribution of this project is to investigate cellulose fiber usage with different materials targeting different applications, as detailed in the sections below.

1.3 Significant research proposal

The research proposals hereafter presented is as follows:

1.3.1 Chapter 2: Carbon Fiber/Epoxy Matrix Composite Interphases Modified with Cellulose Nanocrystals

A composite is a combination of two or more components to produce a new material with improved properties in comparison to its constituents. It is usually formed by a fiber that is responsible for the reinforcement properties and a matrix that protects and holds the fiber. Carbon fiber reinforced polymer (CFRP) composites have gained attention because of their high strength-to-weight ratio. However, one drawback of CFRP, specifically epoxy-based CFRP, is its brittle fracture mechanism. Brittle fracture is not only dependent on the mechanical properties of the fiber and matrix, but also dependent on the effectiveness of the interfacial adhesion between the components [14]. Therefore, a well-designed interphase is required to achieve improvements in the mechanical properties of the composites.

In this work, a process to modify the composite interphase by coating carbon fiber (CF) with functionalized cellulose nanocrystals (CNCs) as a nano-reinforcement to improve the adhesion between the CF and an epoxy matrix was investigated. CNCs were surface treated with 3-aminopropyl triethoxysilane (APTES) and then incorporated in a sizing applied to the fiber. The project goal was to investigate how CNCs could be used to simultaneously strengthen and toughen composite materials. CNCs have attracted considerable attention due to their high mechanical properties, high specific surface area, and the well-known advantages of cellulose fibers: low density, availability, and sustainable nature. An optimum CNC concentration in the sizing was

identified, single fiber adhesion tests to determine the interfacial shear strength (IFSS) were conducted, and appropriate characterization and analyses were completed.

The results demonstrate that sizing CFs with APTES-CNCs is an effective method to increase the interfacial properties in CF reinforced epoxy composites, and the technique can potentially be implemented for interfacial optimization in petroleum-based as well as bio-based natural fiber composites.

1.3.2 Chapter 3: Hybrid Cellulose-Inorganic Reinforcement Polypropylene Composites: Lightweight Materials for Automotive Applications

Cellulose fibers are attracting considerable attention within the transportation industry to reinforce polymer composites. This research is focused on the development of hybrid composites combining cellulose fibers with glass fibers (long and short) or talc in a polypropylene (PP) matrix, and on evaluating the mechanical and thermal properties of the resulting composites for automotive 'under-the-hood' and body interior applications. The fibers were combined with PP in the form of master-batch pellets and Figure 1.1 illustrates the research rationale and advantages.

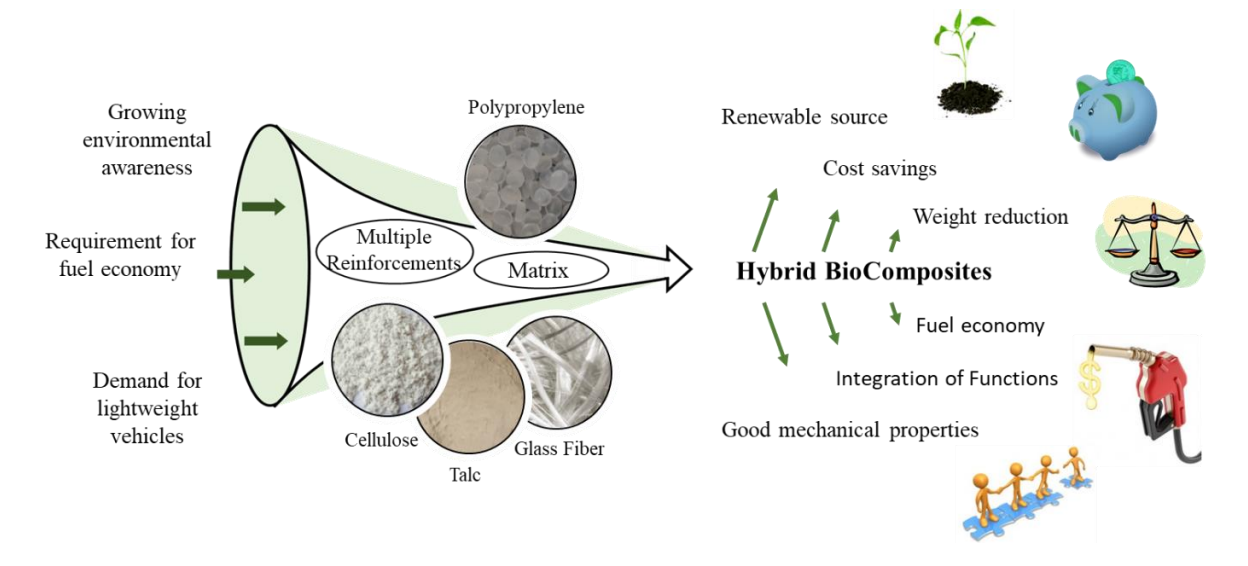


Figure 1.1: Overview of the project discussed on Chapter 3.

The common belief is that natural fibers are limited to processing with low melting temperature thermoplastics, however Ozen *et al.* [15] succeed in melt blending natural fiber blends with nylon 6. The composites with a high content of natural fiber blend displayed enhanced tensile and flexural properties in comparison with neat polymer, which verified that the processing conditions did not affect the final properties. In the present work cellulose fiber were processed with PP at a maximum temperature of 193°C (380 F) without noticeable degradation.

The effects of combining cellulose and glass fibers or talc is investigated, looking for the ideal concentration of each constituent, and also qualifying the fiber-matrix interphase. Results show that in general the mechanical properties (tensile, flexural and impact strength of notched Izod specimens) decreased with increasing cellulose content. However, hybrid composites with an optimum concentration of cellulose fiber is a viable approach leading to weight and cost savings and can reduce or replace the use of inorganic fibers in many automotive applications.

1.3.3 Chapter 4: Flexible Ultraviolet Sensor based on Carbon Nanotubes

Flexible substrates and cellulose paper electronics are attracting considerable attention since they offer new capabilities for devices that are not possible with the conventional rigid substrates. Electronics made of cellulose paper are being investigated as low-cost and disposable alternatives in applications such as sensors and supercapacitors.

In this work, a sensor to detect Ultraviolet (UV) radiation was developed in which cellulose fibers in the form of a paper was investigated as a sensor substrate. Two flexible substrates (Cellulose paper and Polyimide film (PI)) and one rigid substrate (Glass) were chosen. Cellulose paper was chosen since it is a low cost, lightweight, ecofriendly and disposable material.

UV sensors can help in the detection of UV radiation and prevention of health problems related to the intense exposure to this radiation, especially cancer. UV sensors are also widely used in many applications, including space communication and climate change. Carbon Nanotubes (CNTs) as the sensing material and at different concentrations of CNT solution were drop-cast onto the active region between the electrodes of the sensor on each substrate. Multiple tests were conducted including the response of the sensors under UV On/Off illumination cycles and mechanical bending test at varying radius of curvature.

All the sensors respond immediately to UV On/Off cycles with a change in resistance due to the ability of the CNTs to adsorb and desorb oxygen on their surface. Although the PI substrate yields the sensor with the highest response, the results demonstrated that the cellulose paper has the potential to be utilized in this electronics application.

1.3.4 Chapter 5: Surface Modification of Bamboo in Epoxy Composites

Bamboo has fast growing up to 21 cm per day and abundant availability, which makes their fibers attractive compared to other natural fibers [16]. With Young's modulus varying from 19 to 43 GPa and strength varying from 341 to 860 MPa [16], bamboo fibers (BFs) are excellent material to reinforce polymer composites. However, the intrinsic hydrophilicity of BFs can weak the bonding into the matrix and lower the composite mechanical properties. To achieve improved performance, many fiber surface treatments have been done to achieve good fiber-matrix interaction in BF reinforced epoxy composites.

In this work, BFs were surface treated with a solution of NaOH and then coated with Graphene Oxide (GO). Epoxy composites reinforced at a fiber volume content of 40% were processed to assess the impacts on flexural properties and short beam shear strength (SBSS). 40v%

NaOH/GO modified BF composites show a considerable increase of 43% and 29% for flexural modulus and flexural strength, respectively, compared to 40v% untreated BF composites. A slightly increase of 6% was observed for the SBSS.

This investigation shows that the modification of the BF-epoxy matrix interphase with NaOH/GO has the potential to reduce utilization of synthetic fibers in composites and contribute to the global sustainable development.

1.4 Literature review

The following sections review the chemistry, properties and characteristics of the materials used and the state of art of natural fiber surface treatments, mechanism of epoxy curing and recent advances for engineering the composite interphase for improving the adhesion between CF and an epoxy matrix.

1.4.1 Composite materials

Composite is a combination of two or more components to produce a new material with improved properties in comparison to its constituents. One component is the matrix, which is continuous and surrounds the dispersed phase [17]. In general, composites are classified in particle-reinforced, fiber-reinforced, and structural composites [17] as shown on Figure 1.2.

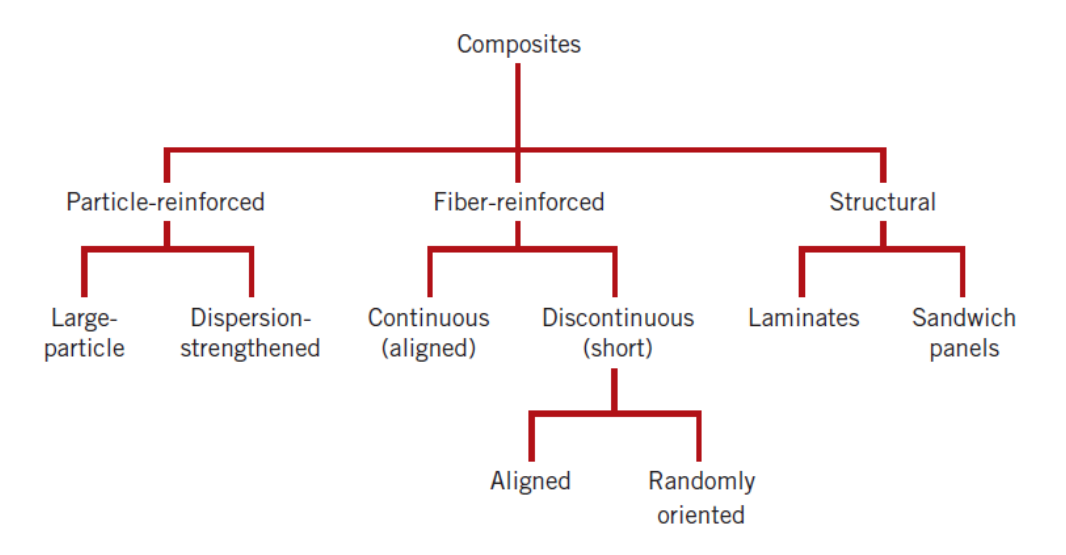


Figure 1.2: Simple scheme for the classification of composite materials [17].

Fiber reinforced polymer composites are formed by a fiber that is responsible for the reinforcement properties and a polymer matrix that protects and holds the fibers. They are ideal for aerospace and automotive industry applications that require lightweight materials with good mechanical properties. Many polymer composites also offer the advantage of being molded in complex shapes.

One important parameter in fiber reinforced polymer composites is the fiber critical aspect ratio ($l_{c/d}$). Fiber critical length (l_c) is the segment capable of maintaining its integrity at an applied strain [18] and Figure 1.3 shows the stress–position profile for a composite subjected to a tensile stress equal to the fiber tensile strength σ_f^* . If the fiber equals or exceeds the required $l_{c/d}$ the maximum fiber load is achieved, and if the fiber is shorter than the $l_{c/d}$ it will not achieve the maximum load [17]. An effective reinforcement is achieved when the fiber aspect ratio is greater than the critical aspect ratio.

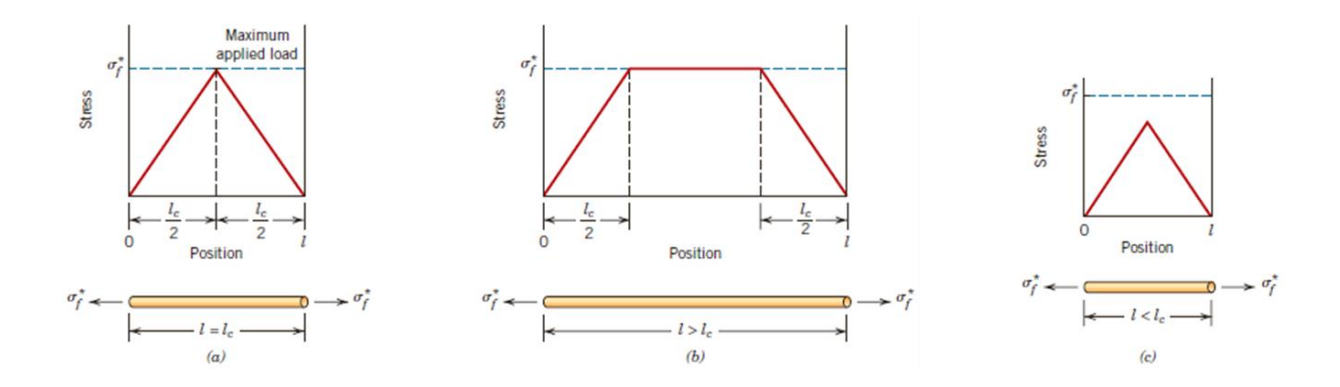


Figure 1.3: Stress–position profiles when fiber length (a) is equal to the critical length, (b) is greater than the critical length, and (c) is less than the critical length [17].

1.4.2 Cellulose fiber

Cellulose is the main load bearing component of plant cell walls and [19] is a stable polymer formed by repeating units of D-anhydroglucose ($C_6H_{11}O_5$) linked by β -1,4- glucosidic bond at C_1 and C_4 position [20] as shown on Figure 1.4. The degree of polymerization (DP) of cellulose ($C_6H_{10}O_5$)_n is defined by the number of n repeating units, and varies depending on the cellulose source. In native cellulose n is up to 10,000 and since the length of the anhydroglucose unit is 0.515 nm, the total length of a native cellulose molecule is about 5μ m [21]. The hydroxyl groups (OH) of the glucose unit can interact through hydrogen bonds with its own chains to create fibrils or with adjacent chains to create microfibrils [22]. The diameter of the elementary fibril is approximately 2 to 4 nm, and when arranged in parallel they form the microfiber with diameter about 10 to 25 nm [23]. Microfibrils entwine into a network to form a fibril with diameter reported at about 500 nm [23]. Within the microfibrils, cellulose possess crystalline regions where the molecules are bonded by strong hydrogen bonds and arranged in an orderly manner [21,23]. The non-crystalline regions are less ordered and amorphous.

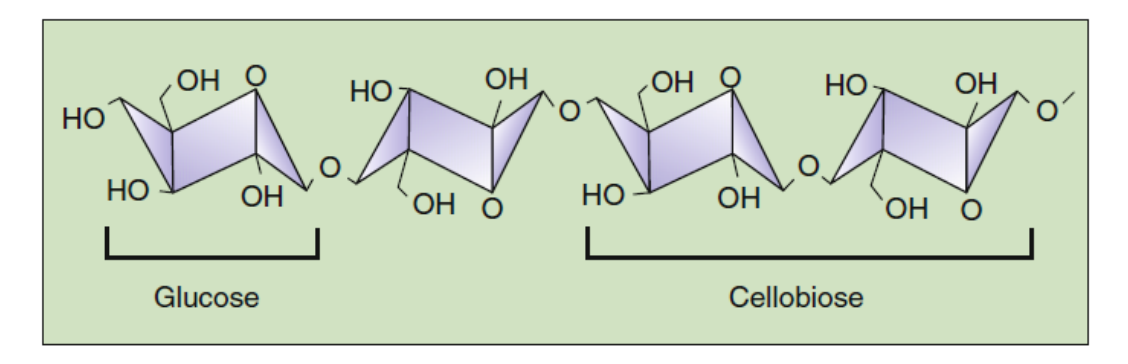


Figure 1.4: Molecular chain structure of cellulose [23]

A single fiber of a plant-based natural fiber consists of several cells, which are formed out of cellulose microfibrils along with lignin and hemicellulose [3]. The ratio between cellulose and lignin/hemicellulose varies among natural fibers, and cotton fiber has the highest cellulose content of 95 - 97 % and 70 % of crystallinity [23]. Figure 1.5 shows that the plant cell wall consists of a primary cell wall (P) and three layers of secondary walls (S₁, S₂ and S₃) where the microfibrils are oriented at distinct angles to the axis of the fiber, along with a cell cavity in the center called lumen [3,24]. The mechanical properties of a natural fiber are generally correlated to its cellulose content and the microfibrillar angle (MFA) of the fibrils [3]. Since the S₂ is the thickest layer, its MFA angle will dictate the elastic properties of the fiber and in general, the lower the spiral angle, the higher the Young's modulus. Ramie fiber has a spiral angle of 7.5° [3] that is among the lowest for natural fibers.

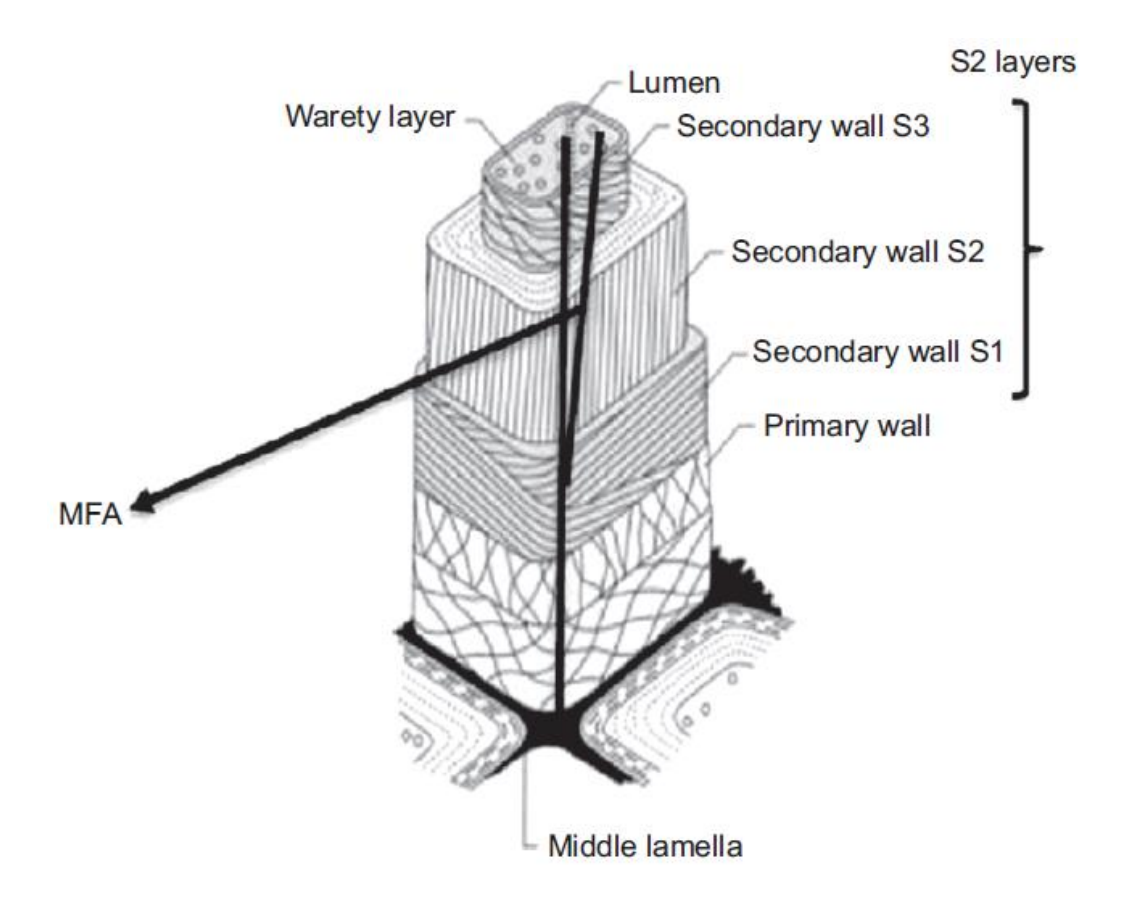


Figure 1.5: MFA definition in the microstructure of plant cell wall together with cell wall sub-layers [7].

Cellulose is the most abundant renewable resource [23] and cellulose fibers have been widely investigated due to the increasing environmental awareness and the reduction of nonrenewable resources [6]. A variety of natural fibers are available, and their properties are listed on Table 1.2.

Table 1.2: Density and properties of some plant based fibers [7].

Fiber	Density	Tensile strength	Elongation at	Young's
	(Kg/m^3)	(MPa)	break	modulus
			(%)	(GPa)
Flax	1380	343 – 1035	1.2 – 3	27.6
Ramie	1440	400 – 938	2 – 4	61.4 – 128
Sisal	1200	507 – 885	1.9 – 3	9.4 – 22
Banana	1350	529 – 914	3 – 10	8 – 32
Bamboo	800 – 1400	391 – 1000	2	11 – 30

1.4.2.1 Natural fiber treatments

One of the greatest challenges of working with natural fiber reinforced polymer composites is related to the interfacial adhesion since natural fibers are polar and hydrophilic and most of polymers are hydrophobic. The hydroxyl groups on the fiber surface or in the non-crystalline regions may attract and react with water molecules by hydrogen bonding [24]. This reduces the interfacial interaction with the matrix and may lead to composites with low mechanical properties [25]. Improvements on the interfacial shear strength and adhesion can be performed through chemical and physical treatments of either the fiber or the matrix.

Alkali treatment is the most common chemical treatment of natural fibers where sodium hydroxide (NaOH) removes a certain amount of lignin and wax in the cell wall of the fiber, which increases the number of reaction sites by exposing the crystallites [26]. The treatment can also break hydrogen bonds, which can increase the fiber surface roughness and promote better mechanical interlocking [26]. However, there is an optimum concentration of NaOH, since the

excess causes excessive delignification and damage to the fiber. Lu *et al.* [27] used this technique to treat hemp fiber. They extruded untreated and treated hemp with recycled high-density polyethylene (rHDPE) and the scanning electron microscope (SEM) shows that the fracture surface of the untreated fiber composite exhibits fiber pullout due to the poor interfacial adhesion. On other hand, the treated hemp composite shows fiber breakage without pullout that confirms the improvement on the interfacial bonding. An increase in the mechanical properties of the composite was also observed due to the alkali treatment.

Coupling agents are effective in enhancing the interfacial compatibility between natural fibers and the polymer matrix, and silane is widely used [28]. Silane has a generic chemical formula of X_3Si -R with bifunctional groups that react with the fiber by one side and the polymer by the other side, establishing a bridge between them [29]. In the presence of water, the alkoxy group of silane (X) will originate silanol that reacts with the OH groups of the fiber, establishing strong covalent bonds.

However, careful attention should be taken with chemical treatments to avoid fiber degradation during the process and/or the decrease of other properties. An alternative to treat the fibers are by physical treatments that modify the surface and structural characteristics of the fibers [30] and improve the mechanical bonding of the fiber into the matrix [31]. A common physical treatment is the cold plasma done through an electrical discharge on the fiber surface that improves the bonding characteristics by changing the surface energy slightly [32].

Valášek *et al.* [33] used oxygen plasma to treat coconut coir, banana and sisal fibers at a discharge power of 350 W for 30 s to evaluate the influence of the treatment on the interfacial interaction of the fibers with epoxy resin. The treatment increased the number of new oxygen

functional groups on the surface of the fibers, which optimized the interfacial interaction with the epoxy resin as observed by SEM micrographs.

After adequate chemical or physical treatment cellulose fiber can yield composites with even better mechanical properties. Overall, natural fiber reinforced composites are emerging as potential substitutes to metal and ceramic based materials in applications such as automotive, aerospace and electronics industries [4]. Many efforts have been done to overcome their weakness and new achievements are promising.

1.4.3 Cellulose nanocrystals (CNCs)

Recently, researchers have used nano-scale cellulose fibers to take advantage of their high specific surface area and aspect ratio. CNCs are extracted from cellulose fibers usually by an acid hydrolysis process that degrades the amorphous regions of the fiber releasing the crystalline nanoparticles [34]. They are rod-like nanocrystals, with average width generally in the order of a few nanometers [34] and with length generally between 100 and 1000 nm [35], depending on their origin and production conditions. Their modulus and strength were estimated around 130 GPa and 7 GPa, respectively [36]. Around 25 years ago, CNC was investigated as a reinforcement for polymers by Favier *et al.* [37] and since then, the publications on nanocellulose has grown considerably, as shown in Figure 1.6. This increasing tendency shows the high interest in this area, and explains the huge number of manufacturing facilities that are being built, which will increase production to upwards of multiple tons per day [34].

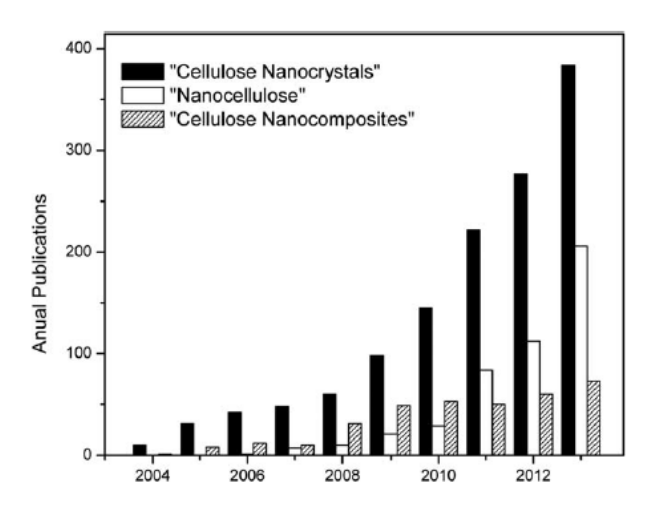


Figure 1.6: Number of publications related with nanocellulose [34].

The main challenge of CNCs in nanocomposite applications are associated with their high hydrophilicity. Many researchers have modified the cellulose surface by non-covalent modification, or by covalent modification such as esterification, polymer grafting and silylation [19].

Surfactants are a simple and fast way for modifying the CNC surface [19], while coupling agents are an effective way for promoting a covalent bond between the CNC and matrix. Silanes are the most effective and widely used coupling agent and Kargarzadeh *et al.*[38] proved that CNCs surface treated with silane could be successfully well dispersed in unsaturated polyester resin (UPR) composites toughened with liquid natural rubber, which contributed to good impact resistance of the composites. Sheltami *et al.*[39] also observed that the adhesion between CNC in a poly(vinyl chloride) (PVC) matrix also improved upon surface modification of the nanocrystals with silane.

1.4.4 **Epoxy**

Epoxy is a commonly used thermosetting that exhibits good mechanical, adhesive and electrical insulating properties, as well as high chemical and corrosion resistance [40]. The diglycidyl ether of bisphenol A (DGEBA), which is the intermediate for epoxy resins, is synthesized from the bisphenol A and epichlohydrin [41] as shown in Figure 1.7.

Figure 1.7: Diglycidyl ether of bisphenol A (DGEBA) [41].

The number-average degree of polymerization (n) depends on the stoichiometry of the reactants and typical values for DGEBA are in the range of 0.03 - 10 [42]. For n values close to zero the monomers are crystalline solids, for n values up to 0.5 the monomers are liquids, and for greater values of n the monomers are amorphous solids [42].

The epoxy grade used in this research was EPONTM resin 828 that is a liquid epoxy resin and its properties are shown on Table 1.3. Its molecular weight (MW) is approximately 380 g/mol and it is suitable for many fabrication techniques, such as pultrusion, filament winding, casting, molding and vacuum bag laminates [40]. A low MW resin was selected since it has a low viscosity, does not require the addition of a solvent and serves as a suitable model for other thermoset systems

from a processing viewpoint. The present resin is bifunctional since its molecule contains two epoxide groups (C_2H_3O) and the weight per epoxide (EEW) shown on Table 1.3 is the ratio of the molecular weight of the epoxy resin to the number of epoxy groups.

Table 1.3: EPON 828 properties [40].

Properties	
Weight per Epoxide (EEW)	185 – 192 g/eq
Viscosity at 25 °C	110 – 150 P
Density	1.16 g/cm ³
Melting point	40 – 44 °C

1.4.5 m-Phenylenediamine (mPDA)

The amine-based curing agent selected to cure the epoxy is mPDA from ACROS Organics, which is an aromatic diamine. Its chemical structure and properties are shown in Figure 1.8 and Table 1.4, respectively.

Figure 1.8: Structure of mPDA [43].

Table 1.4: mPDA properties [43].

Properties	
Physical state	Solid
Molecular Weight	108.14 g/mol
Melting point	63 – 65 °C
Boiling point	282 – 284 °C
Molecular formula	C ₆ H ₈ N ₂

1.4.5.1 Epoxy/amine curing

Figure 1.9 shows the basic steps of the reaction between epoxy resins and diamines. It starts by epoxide ring opening mechanism where the oxygen from the epoxide ring will react with the hydrogen from the primary amine causing the formation of a hydroxyl group and reducing the primary amine into a secondary amine (Figure 1.9 (1)) [44]. The secondary amine can further react with an epoxide group to form a tertiary amine (Figure 1.9 (2)) [44]. Another possible reaction is an ether linkage where the epoxide group reacts with the hydroxyl group (Figure 1.9 (3)), in the presence of a catalyst or at high temperature [45].

Figure 1.9: Three major reactions occurring in epoxy/amine systems [44].

For the present diamine, since the number of active hydrogen per molecule is four, the equivalent weight of amine is calculated by Equation 1 [46]:

Equivalent weight of amine =
$$\frac{\text{MW of amine}}{\text{Number of active hydrogen atoms of amine}}$$
 (1)

where the MW of mPDA is 108.14 g/mol, resulting in 27.04 g/eq that represents the grams of hardener containing one equivalent of N-H group. The present epoxy contains two epoxide groups, and the phr that corresponds to the weight amount of hardener needed per 100 g of epoxy, is calculated by Equation 2 [46]:

Stoichiometric quantity of amine = Equivalent weight of amine *
$$\frac{100}{EEW}$$
 (2)

where the approximate EEW of epoxy is 185 g/eq, leading to approximately 14.5 phr. In this study, EPON Resin 828 cured with 14.5 phr mPDA exhibited tensile strength at break of 89.6 \pm 4.7 MPa, tensile modulus of 3.6 \pm 0.4 GPa and tensile elongation at break of 5.0 \pm 1.0 %.

1.4.6 Carbon fibers (CFs)

CF contains at least 92 wt % carbon and they have high tensile properties, low density and high thermal and chemical stabilities in the absence of oxidizing agents [47]. CFs are not totally crystalline, but are composed of both graphitic (stable form of crystalline carbon at ambient conditions) and noncrystalline regions [17].

Different organic precursor materials are used for producing CFs including rayon, polyacrylonitrile (PAN) and pitch, which will yield fibers with different properties. In general, the first step of production is the stabilization where the precursor fibers experience an oxidization process at about 200 – 400 °C [47]. Then the carbonization in an inert atmosphere at high temperature (around 1,000 °C) will drive off non-carbon elements of the stabilized fibers. Further heat treatment of the carbonized fibers at 3,000 °C yields fibers with higher carbon content and higher Young's modulus [47]. After carbonization, surface treatment of the CFs is performed to improve their adhesion into the polymer matrix.

The properties of the resultant CF depends on the crystallinity, crystalline distribution, molecular orientation, carbon content, defects and other parameters [47]. Figure 1.10 shows the continuous CF used in this project (PAN-based CF supplied by Hexcel Co.) and its properties is shown on Table 1.5.

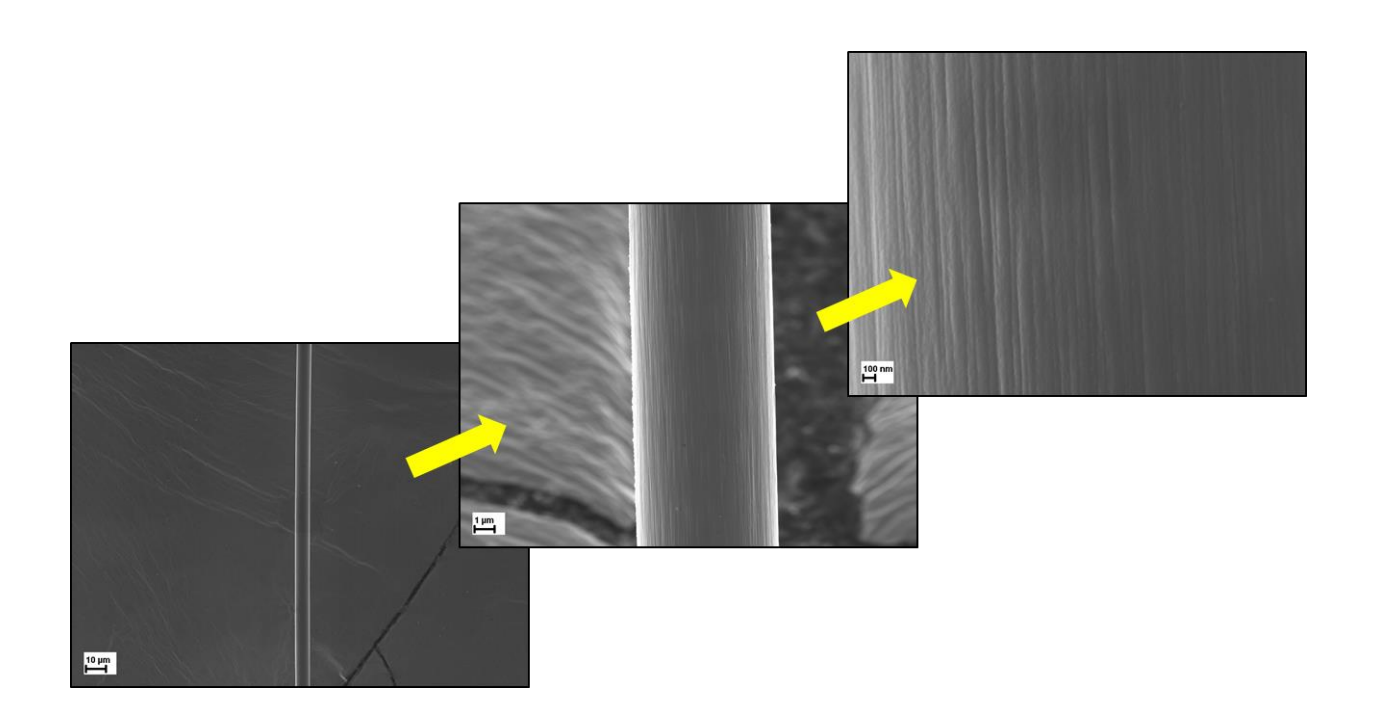


Figure 1.10: FIB-SEM micrographs of CF from lower to higher magnification.

Table 1.5: Typical CF properties [48].

Properties	
Tensile Strength	4,413 MPa
Tensile Modulus (Chord 6000-1000)	231 GPa
Ultimate Elongation at Failure	1.7%
Density	1.79 g/cm ³
Fiber Diameter	7.1 μm

1.4.6.1 Carbon fiber reinforced epoxy composites

Many strategies have been used to increase the interfacial bonding between CFs and epoxy matrix, including fiber surface treatments, sizing or coating, and addition of nanoparticles at the

interphase. This section provides a background about interphase mechanisms and a literature review about recent development on engineering the composite interphase.

1.4.6.2 Fiber surface treatments

Surface treatment processes are frequently applied to CFs to remove the weak outer layer and add functional chemical groups in the surface to improve the wettability to the matrix [49]. Some techniques such as dry and wet oxidation steps and electro-discharge have been studied [50]. The Composite Materials and Structures Center (CMSC) at MSU has developed a process where CFs are surface treated with high intensity ultraviolet light in the presence of ozone (UVO treatment) to increase the surface oxygen concentration. This is beneficial to the fiber wetting by the matrix and details are provided elsewhere [51,52].

Another effective method to enhance fiber—matrix adhesion is through plasma treatment process that generates free radicals that contact the solid surface causing surface cleaning, etching, crosslinking and activation [50]. This method only affects few superficial layers and does not change the fiber bulk properties.

1.4.6.3 Interphase tailoring via sizing or coating

Fiber sizing consists of coating the fiber surface with a thin coating containing polymeric components [53]. The sizing improves wettability and can create an interphase in the composite by dissolution or inter-diffusion [54], which improves the stress transfer and mechanical properties such as a stiffness of the interphase modulus that can lead to an improvement of the IFSS.

Many efforts have been done to predict the IFSS in terms of the fiber, matrix and interphase properties. One of the first approaches was developed by Cox [55,56], who considered an elastic

fiber embedded in an elastic matrix with a perfect bonding. The model led to Equation 3 that assumes no loequated transfer through the ends of the fiber [57]:

$$\tau = E_f \varepsilon_m \left(\frac{G_m}{2E_f \ln(\frac{R}{r})} \right)^{0.5} \frac{\sinh \beta (0.5L - x)}{\cosh \beta \frac{L}{2}} \tag{3}$$

where E_f is the fiber tensile modulus, ε_m is the strain in the matrix, G_m is the matrix shear modulus, R is the interfiber spacing, R is the radius of the fiber, R is a scaling factor, R is the length of the fiber fragment, R is the radial distance outward and R is the interfacial shear stress at a fixed point. If the specimen geometry is fixed and same fiber with fixed properties is used, the IFSS will have a direct dependence on the product of the matrix strain to failure and the square root of the matrix shear modulus [57,58].

Drzal and Madhukar [59] investigated the differences on CFs surface treated with an electrochemical oxidation step only (fibers are called AS4), and CFs coated with a 100-200 nm layer of epoxy applied on the AS4 fibers (fibers are called AS4C). The IFSS of AS4 was 68.3 MPa, which increased to 81.4 MPa for AS4C because of the interaction of the coating layer with the bulk matrix, which caused a local change in properties in the fiber-matrix interphase. The properties of this layer were imparted to the interphase and controlled adhesion, proving the effectiveness of the sizing.

Recently, Liu *et al*. [60] used a thermoplastic polymer solution to size CF reinforced epoxy, which has led to an increase of 15.5% for the IFSS compared to the baseline CF/epoxy composite. It was a result of the increased surface energy at the interphase, which means that the fiber surface contains more polar groups that can establish strong interactions with the resin. The sizing has also

led to 56.1% improvement in interfacial fracture toughness, which shows that the sizing not only improved the IFSS, but also preserved and increased the fracture toughness.

1.4.6.4 Functional interphase: effects of adding nanoparticles in the sizing

One novel approach for engineering the composite interphase is the incorporation of nanoparticles into the fiber surface. One advantage of adding nanoparticles in the sizing is not only improving the fiber-matrix adhesion but also increasing the toughness of the composite by presenting resistance to crack propagation [61]. The presence of nanoparticles in the sizing can also locally increase the shear modulus in the interphase, which can further generate an improvement in the IFSS as shown in Cox's equation.

Qin et. al [54] investigated the quality of CF-epoxy interface by adding functionalized silicon dioxide (SiO₂) nanoparticles. The CFs were immersed in a suspension of SiO₂ nanoparticles functionalized with APTES. The composites exhibited 44% improvement on the IFSS for CFs sized with 1.3 wt% relative concentration of SiO₂, compared to non-coated CFs. This improvement was the result of an increase of the shear modulus of the matrix in the interphase region caused by the presence of the nanoparticles.

As shown in the literature review, CNCs have attracted considerable attention due to their low density, low cost, sustainable nature and high mechanical properties. With all these advantages, CNCs are potential candidate to be added as part of a sizing to modify the CF-epoxy interphase as will be shown on Chapter 2.

1.4.7 Polypropylene (PP)

PP $((C_3H_6)_n)$ is a semi-crystalline polymer [62] obtained from the polymerization of the monomer propylene $(CH_2=CHCH_3)$ [63]. The chemical structure of PP is shown on Figure 1.11.

$$CH_3$$

 CH_2 CH_2

Figure 1.11: Chemical structure of polypropylene [63].

When polymerized, the methyl groups can be oriented in different spatial arrangements in relation to the carbon backbone, leading to isotactic PP (methyl groups are oriented on one side of the carbon backbone, with high degree of crystallinity), syndiotactic PP (methyl groups are on alternate sides of the chain, with less crystalline) and atactic PP (random arrangement of the methyl groups along the carbon backbone, leading to an amorphous polymer) [63,64].

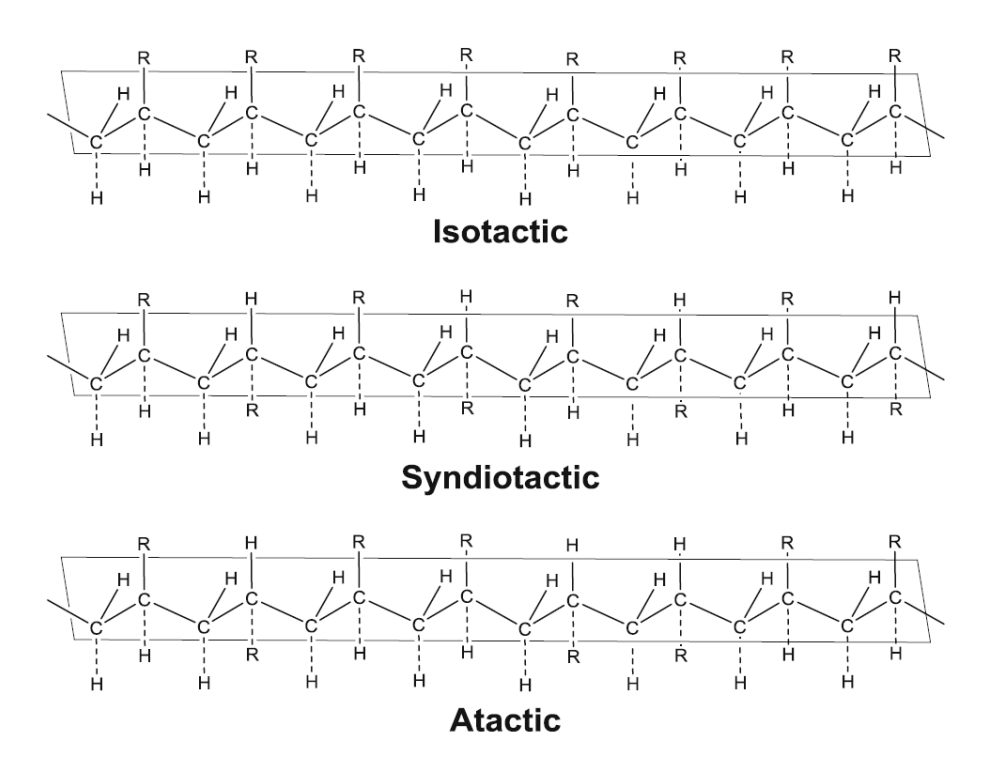


Figure 1.12: Tacticity of polypropylene [63].

The majority of PP is produced as a homopolymer and its melting temperature is at about 160 °C [64]. PP can also be polymerized with ethylene to produce a PP copolymer. Regarding the processing technique this thermoplastic can be molded or extruded and the most common shaping technique is injection molding. Mechanical properties of neat PP and reinforced PP will vary depending on the structure and morphology of the PP, filler and reinforcement, processing and testing conditions [65].

1.4.8 Carbon Nanotubes (CNTs)

CNTs consist of one or several graphene planes rolled in a cylindrical shape with diameters of 1 to several dozens of nanometers and lengths of up to several microns [66]. They can be single-walled carbon nanotubes (SWCNTs) with a diameter of 1 to 2 nm consisting of a single graphite

sheet rolled into a cylindrical tube, they can be double-walled carbon nanotubes (DWCNTs) made of two concentric nanotubes or they can be multiwalled carbon nanotubes (MWCNTs) made by multiple concentric nanotubes with diameters ranging from 2 to 50 nm depending on the number of tubes [67].

They have high aspect ratio, high electrical conductivity and good thermal and mechanical properties [68]. Young's modulus in the range of 270 to 950 GPa and tensile strength between 11 to 63 GPa were reported [67].

In this study SWCNTs were used and they can be classified in terms of chiral vector (\vec{C}_h) and chiral angle (θ) as shown on Figure 1.13 [69]. The chiral vector that indicates the rolling up direction of CNT can be expressed in terms of base vectors (\vec{a}_1) and (\vec{a}_2) and a pair of integer (n, m) according to Equation 4 [69]. The n and m are the chiral indices [68], and depending on their values CNT can be classified as zigzag, armchair and chiral as shown on Figure 1.14.

$$\vec{C}_h = m\vec{a}_1 + n\vec{a}_2 \tag{4}$$

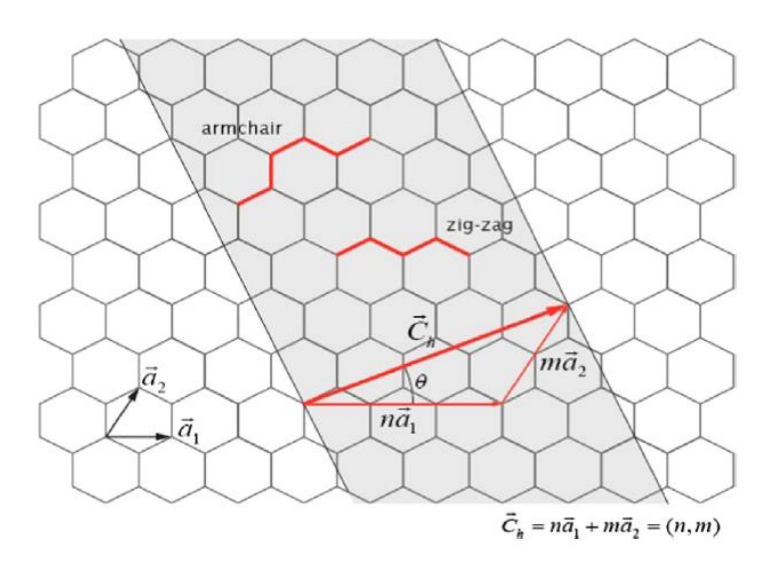


Figure 1.13: Schematic diagram of the chiral vector and the chiral angle [69].

If n and m are equal the CNT is armchair (two edges of each hexagon are perpendicular to the cylinder axis (Figure 1.14(A)), if n or m is equal to 0 the CNT is zigzag (two edges of each hexagon are parallel to the cylinder axis (Figure 1.14(B)) and for other values of indices, CNTs are chiral (Figure 1.14(C)) [66,68,70]. Armchair CNTs exhibit metallic conductivity type, whereas zigzag CNTs are either metallic or semiconducting [68].

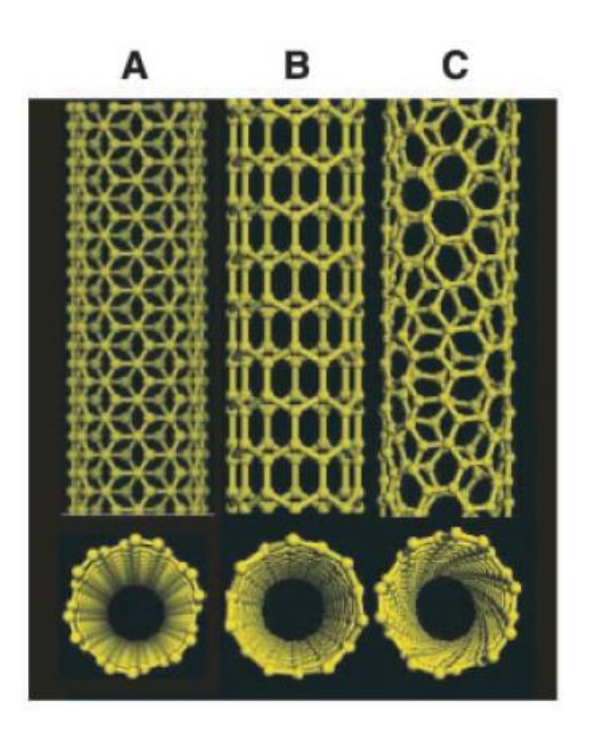


Figure 1.14: Schematic illustrations of the structures of (A) armchair, (B) zigzag, and (C) chiral SWNTs [70].

REFERENCES

REFERENCES

- [1] M.A.S. Spinacé, K.K.G. Fermoseli, M.-A. De Paoli, Recycled polypropylene reinforced with curaua fibers by extrusion, J. Appl. Polym. Sci. 112 (2009) 3686–3694. doi:10.1002/app.29683.
- [2] M. Ramesh, Hemp, jute, banana, kenaf, ramie, sisal fibers, in: Handb. Prop. Text. Tech. Fibres, Elsevier, 2018: pp. 301–325. doi:10.1016/B978-0-08-101272-7.00009-2.
- [3] A.K. Bledzki, J. Gassan, Composites reinforced with cellulose based fibres, Prog. Polym. Sci. (1999). doi:10.1016/S0079-6700(98)00018-5.
- [4] M.R. Sanjay, G.R. Arpitha, L.L. Naik, K. Gopalakrishna, B. Yogesha, Applications of Natural Fibers and Its Composites: An Overview, Nat. Resour. 07 (2016) 108–114. doi:10.4236/nr.2016.73011.
- [5] J.S. Han, J.S. Rowell, Chemical Composition of Fibers, in: R.M. Rowell, R.A. Young, J.K. Rowell (Eds.), Pap. Compos. from Agro-Based Resour., CRC/Lewis Publishers, Boca Raton, 1997: pp. 83–134.
- [6] G. Francucci, E. Rodriguez, Processing of plant fiber composites by liquid molding techniques: An overview, Polym. Compos. 37 (2016) 718–733. doi:10.1002/pc.23229.
- [7] S.R. Djafari Petroudy, Physical and mechanical properties of natural fibers, in: Adv. High Strength Nat. Fibre Compos. Constr., Elsevier, 2017: pp. 59–83. doi:10.1016/B978-0-08-100411-1.00003-0.
- [8] T. Westman, MP; Fifield, LS; Simmons, KL; Laddha, SG; Kafentzis, Natural Fiber Composites: A Review, Washington, 2010. https://www.pnnl.gov/main/publications/external/technical_reports/PNNL-19220.pdf.
- [9] A. Langhorst, A. Kiziltas, D. Mielewski, E. Lee, Selective dispersion and compatibilizing effect of cellulose filler in recycled PA6/PP blends, in: 15th Annu. Soc. Plast. Eng. Automot. Compos. Conf. Exhib., Troy (Detroit), 2015.
- [10] O. Akampumuza, P.M. Wambua, A. Ahmed, W. Li, X.-H. Qin, Review of the applications of biocomposites in the automotive industry, Polym. Compos. 38 (2017) 2553–2569. doi:10.1002/pc.23847.
- [11] M. Fogorasi, I. Barbu, The potential of natural fibres for automotive sector review, IOP Conf. Ser. Mater. Sci. Eng. 252 (2017) 012044. doi:10.1088/1757-899X/252/1/012044.
- [12] D.U. Shah, Developing plant fibre composites for structural applications by optimising composite parameters: a critical review, J. Mater. Sci. 48 (2013) 6083–6107. doi:10.1007/s10853-013-7458-7.

- [13] K. Lau, P. Hung, M.-H. Zhu, D. Hui, Properties of natural fibre composites for structural engineering applications, Compos. Part B Eng. 136 (2018) 222–233. doi:10.1016/j.compositesb.2017.10.038.
- [14] J. Yang, J. Xiao, J. Zeng, L. Bian, C. Peng, F. Yang, Matrix modification with silane coupling agent for carbon fiber reinforced epoxy composites, Fibers Polym. 14 (2013) 759–766. doi:10.1007/s12221-013-0759-2.
- [15] E. Ozen, A. Kiziltas, E.E. Kiziltas, D.J. Gardner, Natural fiber blends-filled engineering thermoplastic composites for the automobile industry, in: 12th Annu. Automot. Compos. Conf. Exhib. 2012 (ACCE 2012) Unleashing Power Des., Troy (Detroit), 2012.
- [16] D.E. Depuydt, N. Sweygers, L. Appels, J. Ivens, A.W. van Vuure, Bamboo fibres sourced from three global locations: A microstructural, mechanical and chemical composition study, J. Reinf. Plast. Compos. (2019) 1–16. doi:10.1177/0731684419828532.
- [17] W.D. Callister, D.G. Rethwisch, Materials science and engineering: An introduction (eight edition), 2009. doi:10.1016/0261-3069(91)90101-9.
- [18] T. Lacroix, B. Tilmans, R. Keunings, M. Desaeger, I. Verpoest, Modelling of critical fibre length and interfacial debonding in the fragmentation testing of polymer composites, Compos. Sci. Technol. 43 (1992) 379–387. doi:10.1016/0266-3538(92)90061-7.
- [19] F. Ansari, M. Salajková, Q. Zhou, L.A. Berglund, Strong Surface Treatment Effects on Reinforcement Efficiency in Biocomposites Based on Cellulose Nanocrystals in Poly(vinyl acetate) Matrix, Biomacromolecules. 16 (2015) 3916–3924. doi:10.1021/acs.biomac.5b01245.
- [20] R. Kumar, S. Obrai, A. Sharma, Chemical modifications of natural fiber for composite material, Pelagia Res. Libr. (2011).
- [21] L. Fan, M.M. Gharpuray, Y.-H. Lee, Cellulose Hydrolysis, Springer Berlin Heidelberg, Berlin, Heidelberg, 1987. doi:10.1007/978-3-642-72575-3.
- [22] A. Thygesen, Properties of hemp fibre polymer composites-An optimisation of fibre properties using novel defibration methods and fibre characterisation, R. Agric. Vet. Univ. (2006). doi:(Risø-PhD; No. 11(EN)).
- [23] H. Chen, Chemical Composition and Structure of Natural Lignocellulose, in: Biotechnol. Lignocellul., Springer Netherlands, Dordrecht, 2014: pp. 25–71. doi:10.1007/978-94-007-6898-7_2.
- [24] L. Hua, P. Zadorecki, P. Flodin, Cellulose fiber-polyester composites with reduced water sensitivity (1)—chemical treatment and mechanical properties, Polym. Compos. 8 (1987) 199–202. doi:10.1002/pc.750080308.
- [25] M.M. Kabir, H. Wang, T. Aravinthan, F. Cardona, K.-T. Lau, Effects of natural fibre surface on composite properties: a review, in: 1st Int. Postgrad. Conf. Eng. Des. Dev.

- Built Environ. Sustain. Wellbeing, Brisbane, 2011: pp. 94–99.
- [26] C. Mohan D., M. B., Characterization of Kenaf fibre reinforced composites, J. Chem. Pharm. Res. 6 (2014) 626–628.
- [27] N. Lu, R.H. Swan, I. Ferguson, Composition, structure, and mechanical properties of hemp fiber reinforced composite with recycled high-density polyethylene matrix, J. Compos. Mater. 46 (2012) 1915–1924. doi:10.1177/0021998311427778.
- [28] S. Kalia, A. Dufresne, B.M. Cherian, B.S. Kaith, L. Avérous, J. Njuguna, E. Nassiopoulos, Cellulose-Based Bio- and Nanocomposites: A Review, Int. J. Polym. Sci. 2011 (2011) 1–35. doi:10.1155/2011/837875.
- [29] Y. Xie, C.A.S. Hill, Z. Xiao, H. Militz, C. Mai, Silane coupling agents used for natural fiber/polymer composites: A review, Compos. Part A Appl. Sci. Manuf. 41 (2010) 806–819. doi:10.1016/j.compositesa.2010.03.005.
- [30] L.A. Pothan, A.S. Luyt, S. Thomas, Polyolefin/Natural Fiber Composites, in: Polyolefin Compos., John Wiley & Sons, Inc., Hoboken, NJ, USA, n.d.: pp. 44–86. doi:10.1002/9780470199039.ch3.
- [31] A.K. Bledzk, V.E. Sperber, O. Faruk, Natural and Wood Fibre Reinforcement in Polymers, 2002.
- [32] O. Faruk, A.K. Bledzki, H.-P. Fink, M. Sain, Biocomposites reinforced with natural fibers: 2000–2010, Prog. Polym. Sci. 37 (2012) 1552–1596. doi:10.1016/j.progpolymsci.2012.04.003.
- [33] P. Valášek, M. Müller, V. Šleger, Influence of Plasma Treatment on Mechanical Properties of Cellulose-based Fibres and Their Interfacial Interaction in Composite Systems, BioResources. 12 (2017) 5449–5461. doi:10.15376/biores.12.3.5449-5461.
- [34] M. Mariano, N. El Kissi, A. Dufresne, Cellulose nanocrystals and related nanocomposites: Review of some properties and challenges, J. Polym. Sci. Part B Polym. Phys. 52 (2014) 791–806. doi:10.1002/polb.23490.
- [35] H. Kargarzadeh, R.M. Sheltami, I. Ahmad, I. Abdullah, A. Dufresne, Cellulose nanocrystal: A promising toughening agent for unsaturated polyester nanocomposite, Polym. (United Kingdom). 56 (2015) 346–357. doi:10.1016/j.polymer.2014.11.054.
- [36] J. Lu, P. Askeland, L.T. Drzal, Surface modification of microfibrillated cellulose for epoxy composite applications, Polymer (Guildf). 49 (2008) 1285–1296. doi:10.1016/j.polymer.2008.01.028.
- [37] V. Favier, H. Chanzy, J.Y. Cavaille, Polymer Nanocomposites Reinforced by Cellulose Whiskers, Macromolecules. 28 (1995) 6365–6367. doi:10.1021/ma00122a053.
- [38] H. Kargarzadeh, R.M. Sheltami, I. Ahmad, I. Abdullah, A. Dufresne, Cellulose

- nanocrystal reinforced liquid natural rubber toughened unsaturated polyester: Effects of filler content and surface treatment on its morphological, thermal, mechanical, and viscoelastic properties, Polym. (United Kingdom). 71 (2015) 51–59. doi:10.1016/j.polymer.2015.06.045.
- [39] R.M. Sheltami, H. Kargarzadeh, I. Abdullah, Effects of silane surface treatment of cellulose nanocrystals on the tensile properties of cellulose-polyvinyl chloride nanocomposite, Sains Malaysiana. 44 (2015) 801–810.
- [40] Hexion, EPONTM Resin 828 Technical Data Sheet, (2005). https://www.hexion.com/CustomServices/PDFDownloader.aspx?type=tds&pid=1fb05b42 -5814-6fe3-ae8a-ff0300fcd525 (accessed February 10, 2019).
- [41] J.I. Yang, Part I: Synthesis of Aromatic Polyketones Via Soluble Precursors Derived from Bis(A-Aminintrile)S; Part Ii: Modifications of Epoxy Resins with Functional Hyperbranched Poly(Arylene Ester)s, Virginia Polytechnic Institute and State University, 1998.
- [42] J.-P. Pascault, R.J.J. Williams, General Concepts about Epoxy Polymers, in: Epoxy Polym., Wiley-VCH Verlag GmbH & Co. KGaA, Weinheim, Germany, 2010: pp. 1–12. doi:10.1002/9783527628704.ch1.
- [43] ThermoFisher Scientific, m-Phenylenediamine Safety Data Sheet, (2018). https://www.acros.com/DesktopModules/Acros_Search_Results/Acros_Search_Results.as px?search_type=CatalogSearch&SearchString=130560010 (accessed February 10, 2019).
- [44] H. Liu, A. Uhlherr, R.J. Varley, M.K. Bannister, Influence of substituents on the kinetics of epoxy/aromatic diamine resin systems, J. Polym. Sci. Part A Polym. Chem. 42 (2004) 3143–3156. doi:10.1002/pola.20169.
- [45] Y. Zhang, S. Vyazovkin, Effect of Substituents in Aromatic Amines on the Activation Energy of Epoxy–Amine Reaction, J. Phys. Chem. B. 111 (2007) 7098–7104. doi:10.1021/jp071001h.
- [46] L.M. Meng, Y.C. Yuan, M.Z. Rong, M.Q. Zhang, A dual mechanism single-component self-healing strategy for polymers, J. Mater. Chem. 20 (2010) 6030. doi:10.1039/c0jm00268b.
- [47] X. Huang, Fabrication and Properties of Carbon Fibers, Materials (Basel). 2 (2009) 2369–2403. doi:10.3390/ma2042369.
- [48] Hexcel Corporation, HexTow® AS4 Carbon Fiber Datasheet, (2018). https://www.hexcel.com/user_area/content_media/raw/AS4_HexTow_DataSheet.pdf (accessed February 10, 2019).
- [49] L.T. Drzal, M.J. Rich, P.F. Lloyd, Adhesion of Graphite Fibers to Epoxy Matrices: I. The Role of Fiber Surface Treatment, J. Adhes. 16 (1983) 1–30. doi:10.1080/00218468308074901.

- [50] L. Tang, J.L. Kardos, A review of methods for improving the interfacial adhesion between carbon fiber and polymer matrix, Polym. Compos. 18 (1997) 100–113. doi:10.1002/pc.10265.
- [51] M.J. Rich, L.T. Drzal, B.P. Rook, P. Askeland, E.K. Drown, Novel carbon fiber surface treatment with ultravilet light in ozone to promote composite mechanical properties, ICCM Int. Conf. Compos. Mater. (2009).
- [52] M.J. Rich, E.K. Drown, P. Askeland, L.T. Drzal, Surface Treatment of Carbon Fibers By Ultraviolet Light + Ozone: Its Effect on Fiber Surface Area and Topography, in: 19TH Int. Conf. Compos. Mater., 2013.
- [53] Z. Dai, F. Shi, B. Zhang, M. Li, Z. Zhang, Effect of sizing on carbon fiber surface properties and fibers/epoxy interfacial adhesion, Appl. Surf. Sci. 257 (2011) 6980–6985. doi:10.1016/j.apsusc.2011.03.047.
- [54] W. Qin, F. Vautard, P. Askeland, J. Yu, L. Drzal, Modifying the carbon fiber–epoxy matrix interphase with silicon dioxide nanoparticles, RSC Adv. 5 (2015) 2457–2465. doi:10.1002/pc.23325.
- [55] H.L. Cox, The elasticity and strength of paper and other fibrous materials, Br. J. Appl. Phys. 3 (1952) 72–79. doi:10.1088/0508-3443/3/302.
- [56] T.F. Cooke, High Performance Fiber Composites with Special Emphasis on the Interface: A Review of the Literature, J. Polym. Eng. 7 (1987).
- [57] V. Rao, L.T. Drzal, The dependence of interfacial shear strength on matrix and interphase properties, Polym. Compos. 12 (1991) 48–56. doi:10.1002/pc.750120108.
- [58] W. Qin, F. Vautard, L.T. Drzal, J. Yu, Mechanical and electrical properties of carbon fiber composites with incorporation of graphene nanoplatelets at the fiber-matrix interphase, Compos. Part B Eng. 69 (2015) 335–341. doi:10.1016/j.compositesb.2014.10.014.
- [59] L.T. Drzal, M. Madhukar, Fibre-matrix adhesion and its relationship to composite mechanical properties, J. Mater. Sci. 28 (1993) 569–610. doi:10.1007/BF01151234.
- [60] R. Liu, WenBo; Zhang, Shu; Li, Bichen; Yang, Fan; Jiao, WeiCheng; Hao, LiFeng; Wang, Improvement in Interfacial Shear Strength and Fracture Toughness for Carbon Fiber Reinforced Epoxy Composite by Fiber Sizing, Polym. Compos. 35 (2013) 482–488.
- [61] J. Karger-Kocsis, H. Mahmood, A. Pegoretti, Recent advances in fiber/matrix interphase engineering for polymer composites, Prog. Mater. Sci. 73 (2015) 1–43. doi:10.1016/j.pmatsci.2015.02.003.
- [62] B. Pukánszky, Particulate filled polypropylene: structure and properties, in: Polypropyl. Struct. Blends Compos., Springer Netherlands, Dordrecht, 1995: pp. 1–70. doi:10.1007/978-94-011-0523-1_1.

- [63] Y. Takashima, Polypropylene, Encycl. Polym. Nanomater. (2014) 1–6. doi:10.1007/978-3-642-36199-9_254-1.
- [64] H. Karian, Handbook of Polypropylene and Polypropylene Composites, Revised and Expanded, CRC Press, 2003. doi:10.1201/9780203911808.
- [65] J. Karger-Kocsis, Microstructural aspects of fracture in polypropylene and in its filled, chopped fiber and fiber mat reinforced composites, in: Polypropyl. Struct. Blends Compos., Springer Netherlands, Dordrecht, 1995: pp. 142–201. doi:10.1007/978-94-011-0523-1_4.
- [66] I. V. Zaporotskova, N.P. Boroznina, Y.N. Parkhomenko, L. V. Kozhitov, Carbon nanotubes: Sensor properties. A review, Mod. Electron. Mater. (2016). doi:10.1016/j.moem.2017.02.002.
- [67] K.S. Ibrahim, Carbon nanotubes-properties and applications: a review, Carbon Lett. 14 (2013) 131–144. doi:10.5714/CL.2013.14.3.131.
- [68] B.K. Kaushik, M.K. Majumder, Carbon Nanotube: Properties and Applications, in: Carbon Nanotub. Based VLSI Interconnects, 2015: pp. 17–37. doi:10.1007/978-81-322-2047-3_2.
- [69] L. Boumia, M. Zidour, A. Benzair, A. Tounsi, A Timoshenko beam model for vibration analysis of chiral single-walled carbon nanotubes, Phys. E Low-Dimensional Syst. Nanostructures. 59 (2014) 186–191. doi:10.1016/j.physe.2014.01.020.
- [70] R.H. Baughman, Carbon Nanotubes--the Route Toward Applications, Science (80-.). 297 (2002) 787–792. doi:10.1126/science.1060928.

CHAPTER 2: CARBON FIBER/EPOXY MATRIX COMPOSITE INTERPHASES MODIFIED WITH CELLULOSE NANOCRYSTALS

Portions of this chapter were published in the Composites Science and Technology Journal with citation "M.D. Reale Batista, L.T. Drzal, Carbon fiber/epoxy matrix composite interphases modified with cellulose nanocrystals, Compos. Sci. Technol. 164 (2018) 274–281. doi:10.1016/j.compscitech.2018.05.010."

2.1 Abstract

The incorporation of nanoparticles at the composite interphase has attracted considerable attention due to their contribution to the functional and mechanical properties of the composite. Cellulose nanocrystals (CNCs) were used to modify the interphase between carbon fiber (CF) and an epoxy matrix to simultaneously strengthen and toughen the CF composite. CNCs were functionalized with 3-aminopropyltriethoxysilane (APTES) and surface modification was confirmed by Fourier transform infrared (FTIR) spectroscopy and X-ray photoelectron spectroscopy (XPS), which revealed the presence of the new chemical species. Functionalized CNCs (APTES-CNCs) were applied as part of a sizing to coat CFs and an optimum concentration was identified. The APTES-CNCs dispersion on the surface of CFs was characterized by scanning electron microscopy (SEM) and the interfacial adhesion was assessed by measuring the interfacial shear strength (IFSS) through the single fiber fragmentation test (SFFT). IFSS indicated stronger adhesion between the CFs and the epoxy matrix for the fibers sized with APTES-CNCs, compared to unsized CFs and epoxy-only sized CFs. CFs sized with APTES-CNCs at a concentration of 1.0 wt% resulted in an 81% increase in IFSS compared to unsized CFs, and the birefringent stress pattern seen during the SFFT supports the assumption that adding APTES-CNCs at the composite interphase promotes an improvement in the failure mode. These results demonstrate that sizing CFs with APTES-CNCs is an effective method to increase the interfacial properties in CF reinforced epoxy composites, and a potential approach for the development of ecofriendly and lightweight composite materials for aerospace and automotive applications.

Keywords: Interphase; Fiber/matrix bond; Polymer-matrix composites; Carbon fibers; Cellulose nanocrystal;

2.2 Introduction

Lightweight, high-strength and high-stiffness are often identified as desirable properties for parts used in aerospace and automotive fields. The U.S. Environmental Protection Agency (EPA)'s standards will require a target of 54.5 miles per gallon to be met by model year 2025 [1]. To achieve these engineering needs and meet the growing requirement for fuel economy, carbon fiber reinforced polymer (CFRP) composites have gained attention because of their high strength-to-weight ratio. However, one drawback of CFRP, specifically epoxy-based CFRP, is its brittle fracture mechanism. Brittle fracture is not only dependent on the mechanical properties of the fiber and matrix, but also dependent on the effectiveness of the interfacial adhesion between the components [2]. Therefore, a well-designed interphase is required to achieve improvements in the mechanical properties of the composites.

According to Karger-Kocsis et al. [3] the term interphase has been defined as a finite interlayer with distinct physico-chemical properties between the fiber and matrix. The interphase comprises a three dimensional region where the local properties vary from the properties of the bulk matrix and bulk fiber [4]. The interfacial adhesion between the fiber and matrix and the effectiveness of the stress transfer at the interphase are essential elements for composite

performance. An interphase engineered to increase stress transfer from the matrix to the reinforcing fiber will result in a composite with greater strength and structural integrity [5]. Many strategies have been used to increase the interfacial bonding between the fiber and matrix, including fiber surface treatments, sizing or coating, and the addition of nanoparticles in the interphase.

Surface treatment processes such as dry and wet oxidation steps, plasma treatment, electrodischarge [6] and ultraviolet light with ozone (UVO treatment) [7] are frequently applied to CFs to remove the weak outer layer and add functional chemical groups in the surface to improve the wettability to the matrix [4] and to chemically react with the polymer matrix.

In addition to surface treatments, the application of a fiber sizing, which consists of a thin coating on the fiber surface containing polymeric components [8] is commonly used. The sizing improves wettability, provides fiber protection during handling and weaving and can create an interphase in the composite by dissolution or inter-diffusion [5] into the polymer matrix, which improves the stress transfer and mechanical properties such as stiffness of the interphase modulus that can lead to an improvement of the IFSS. Cox's shear-lag model [9,10] shows that the IFSS will have a direct dependence on the product of the matrix strain to failure and the square root of the matrix shear modulus [11,12]. Much work [13,14] has been done on sizing CFs to improve the interfacial adhesion and mechanical properties of the composites.

A recent development has been the incorporation of nanoparticles into the fiber–matrix interphase through the sizing. The addition of nanoparticles has the potential for not only improving the fiber-matrix adhesion but also for increasing the toughness of the composite by providing resistance to crack propagation [3]. The presence of nanoparticles in the sizing can also

locally increase the shear modulus in the interphase, which can further generate an improvement in the IFSS.

An additional benefit to adding nanoparticles in the interphase is imparting other properties beyond mechanical to produce a multifunctional material. Qin et al. [12] showed that incorporating graphene nanoplatelets (GnP) in the CF/epoxy interphase not only improved the flexural and interlaminar shear strength, but also created a conductive path between the fibers that improved electrical conductivity.

Several methods have been proposed to incorporate nanoparticles on the fiber surface: electrophoretic deposition (EPD), chemical vapor deposition (CVD), spray coating [3] and dipping [15,16]. It has been reported that the addition of graphite nanoplatelets [17], GnP [12] and functionalized silicon dioxide nanoparticles [5,18] to the sizing increases the adhesion at the composite interphase by mechanical interlocking, establishment of covalent bonding as well as stiffening of the interphase modulus.

CNCs, extracted from cellulose fibers [19] have attracted considerable attention due to their high mechanical properties, high specific surface area, low cost, low density, availability, and sustainable nature. CNCs are rod-like cellulose nanocrystals, with average width generally in the order of a few nanometers [19] and with length generally between 100 and 1000 nm [20]. Their modulus and strength are estimated around 130 GPa and 7 GPa, respectively [21], making them an attractive nanoparticle to be added to an engineered sizing to modify the CF-epoxy interphase.

The main challenge in utilizing CNCs in composite applications is their high hydrophilicity, which makes them incompatible with hydrophobic polymers. To overcome this drawback, researchers have modified the cellulose surface by non-covalent modification, or by

covalent modification such as esterification, polymer grafting and silylation [22]. Silane coupling agents are widely used to surface treat CNCs [23].

In this work, a process to modify the composite interphase by coating a CF with functionalized CNCs as a nano-reinforcement to improve the adhesion between the CF and an epoxy matrix was investigated. CNCs were surface treated with 3-aminopropyl triethoxysilane (APTES) and then incorporated in a sizing applied to the fiber. The project goal was to investigate how CNCs could be used to simultaneously strengthen and toughen composite materials. This work utilizes the dipping sizing technique for coating single fibers and multiple fiber tows. An optimum CNC concentration in the sizing was identified, single fiber adhesion tests were conducted, and appropriate characterization and analyses were completed.

2.3 Experimental

2.3.1 Materials

A CNC slurry was purchased from University of Maine (Process Development Center) with 12.2 wt% CNC in water. APTES was chosen to functionalize the surface of CNCs and was obtained from Aldrich (99%). Polyacrylonitrile (PAN)-based CFs AS4 (12k filament count tow) were supplied by Hexcel Co. with an average diameter of 7.1μm. The CFs were surface treated by the UVO treatment developed in our laboratories [7]. The epoxy used was EPONTM resin 828 (viscosity of 110 – 150 P at 25°C) supplied by Hexion Inc. and the curing agent was m-Phenylenediamine (mPDA) supplied by ACROS Organics. Acetone and ethanol were chosen as solvents for the solvent exchange process of the CNC slurry.

2.3.2 Methods

2.3.2.1 Surface treatment of CNCs

A solvent exchange process was utilized to disperse CNCs in an adequate solvent for further chemical modification of their surface. The CNC slurry was diluted with water and solvent exchanged with ethanol and acetone and then surface treated with APTES based on a method applied to micro fibrillated cellulose (MFC) as described elsewhere [21]. First, the CNC slurry was diluted with water to obtain CNCs at 0.5 wt%. Then it was sonicated for 6 min (10s On / 5s Off) using a Cole-Parmer 750-Watt Ultrasonic processor, and stirred for 72 h. This aqueous suspension was solvent exchanged with ethanol three times and then with acetone three times using a rotary evaporator (BUCHI R-114) as shown on Figure 2.1. After each successive mixing with the solvent, 5 min sonication (10s On / 5s Off) was applied to ensure good dispersion of the nanoparticles. The content of CNCs in acetone was adjusted to be 0.6 wt%. After the solvent exchange process, APTES was added into the CNCs acetone suspension to yield a 0.3 wt% final concentration and the suspension was stirred for 40 h. This APTES-CNC acetone suspension was used as the baseline for the sizing preparation described in Section 2.3.2.2.



Figure 2.1: Solvent exchange process using a rotary evaporator.

To confirm effectiveness of the CNC surface treatment, an APTES-CNC acetone suspension was filtered and the sediments were dried at room temperature (RT) for 24 h for further analysis. Some specimens received additional treatment at 120 °C for 2 h for comparison [21]. CNCs that were treated with APTES are abbreviated as APTES-CNCs.

2.3.2.2 Sizing of CFs with APTES-CNC

Figure 2.2 represents the process used for sizing CFs with APTES-CNCs. The epoxy was dispersed in the APTES-CNC acetone suspension by sonication for 10 min (10s On / 5s Off) and the sizing was continuously stirred for 5 h. Then the curing agent mPDA was added and the sizing was stirred for 1-2 h. Evaporation of acetone occurred simultaneously during these 6-7 h of stirring to adjust the sizing concentration as required. Final sizing stoichiometry was kept constant at 1.4

wt% of (epoxy resin + 9 phr mPDA) in acetone and the CNC concentrations were set at 0.6 wt%, 1.0 wt% and 2.0 wt% to the total sizing solution. These CNC concentrations were calculated based on the CNC weight only.

CFs were sized by two different techniques for comparison purposes. The first technique (Figure 2.2(a)) consists of dipping the 12k filament tow into the sizing solution for 20 seconds and slowly pulling the tow out. The second technique (Figure 2.2(b)) consists of aligning and mounting individual CFs onto a square-shaped metal frame and immersing them into the sizing solution for approximately 32 min (sequence of 5 min without stir / 3 min with stir) and in the last minute slowly pulling the metal frame out. For both techniques, the final step is drying the sized CFs in an oven at 60°C for 3 h. CFs without sizing and CFs sized with epoxy-only were prepared as control samples. For CFs sized with epoxy-only, 1.4 wt% of (epoxy resin + 9 phr mPDA) was dissolved in acetone and then CFs were sized accordingly.

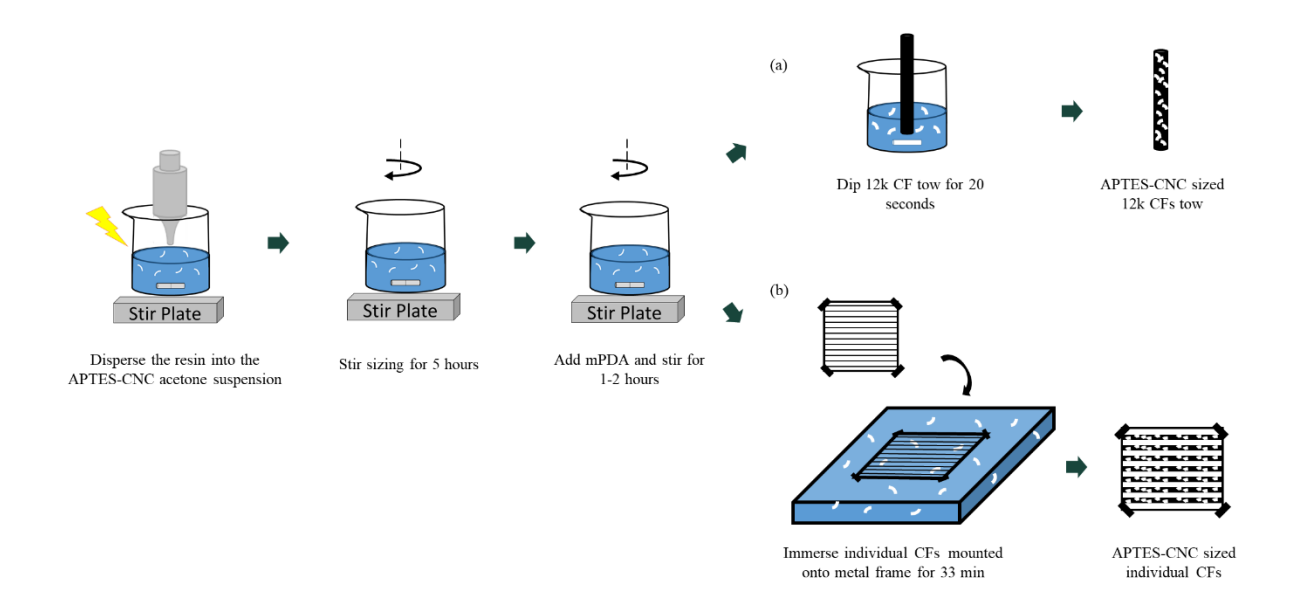


Figure 2.2: Schematic illustration of the sizing process: a) 20s dipping of the 12k filament tow and b) 33 min immersion of metal frame with individual CFs.

2.3.2.3 Preparation of SFFT coupon

A single CF was aligned axially in the cavity of a dogbone coupon in a silicone mold and kept taut with rubber cement in the end sprues as shown in Figure 2.3. The epoxy and curing agent were heated at 75°C, then mixed at a concentration of 14.5 phr mPDA and degassed in a vacuum oven. The silicone mold containing the single CFs was also degassed to remove trapped air in the mold and yield void-free samples. Then the resin system was carefully added into the silicone mold covering the CFs and coupons were cured at 75°C for 2 h and postcured at 125°C for 2 h. Cured coupons were polished to obtain high fidelity specimens to conduct the fragmentation test.

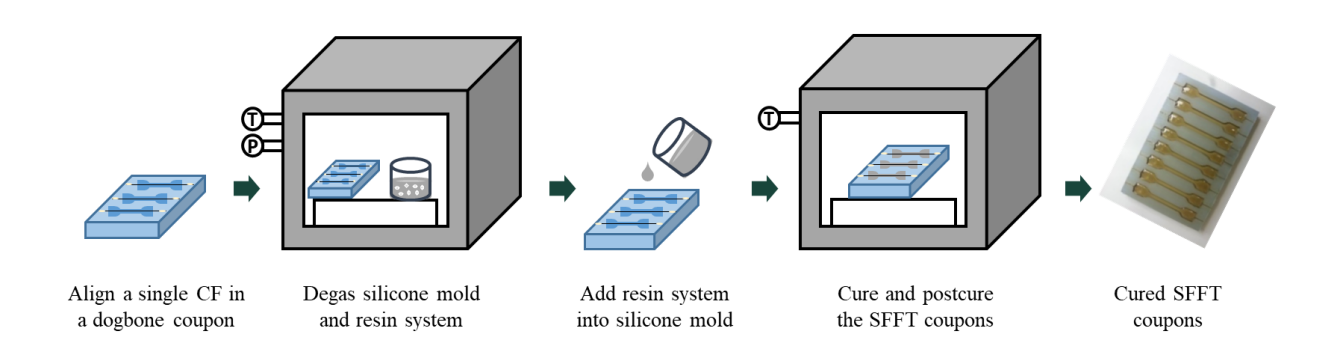


Figure 2.3: Schematic of preparation of the SFFT coupon.

2.3.3 Characterization methods

2.3.3.1 Fourier transform infrared (FTIR) spectroscopy

FTIR spectroscopy with a diamond attenuated total reflectance (ATR) window was used to investigate the changes in the functional groups as a result of the surface treatment of CNCs. Both untreated CNCs and APTES-CNCs were characterized with a PerkinElmer Spectrum One system at a resolution of 4 cm⁻¹, 16 scans, from 4000-650 cm⁻¹.

2.3.3.2 X-ray photoelectron spectroscopy (XPS)

Both untreated CNCs and APTES-CNCs were characterized by XPS using a Physical Electronics 5400 ESCA. Prior to XPS analysis, a Soxhlet extraction process with acetone was given to the APTES-CNCs to remove any physically bonded silane [21]. Survey spectra were collected at 187.85 eV pass energy and higher resolution spectra were collected with 29.35 eV pass energy.

2.3.3.3 Scanning Electron Microscopy (SEM)

A Carl Zeiss Auriga FIB scanning electron microscope with accelerating voltage of 5 keV was used to observe the homogeneity of the APTES-CNC distribution on the surface of CFs. Unsized and sized CFs were mounted on the SEM sample holder on top of carbon tape and sputter-coated with tungsten to prevent surface charging.

2.3.3.4 Single Fiber Fragmentation Test (SFFT)

The SFFT [13,24] was used to determine the level of adhesion between the CFs and the epoxy system. Figure 2.4 shows a coupon containing a single CF mounted in a tensile jig fitted onto a transmitted light optical microscope (Olympus BH-2).

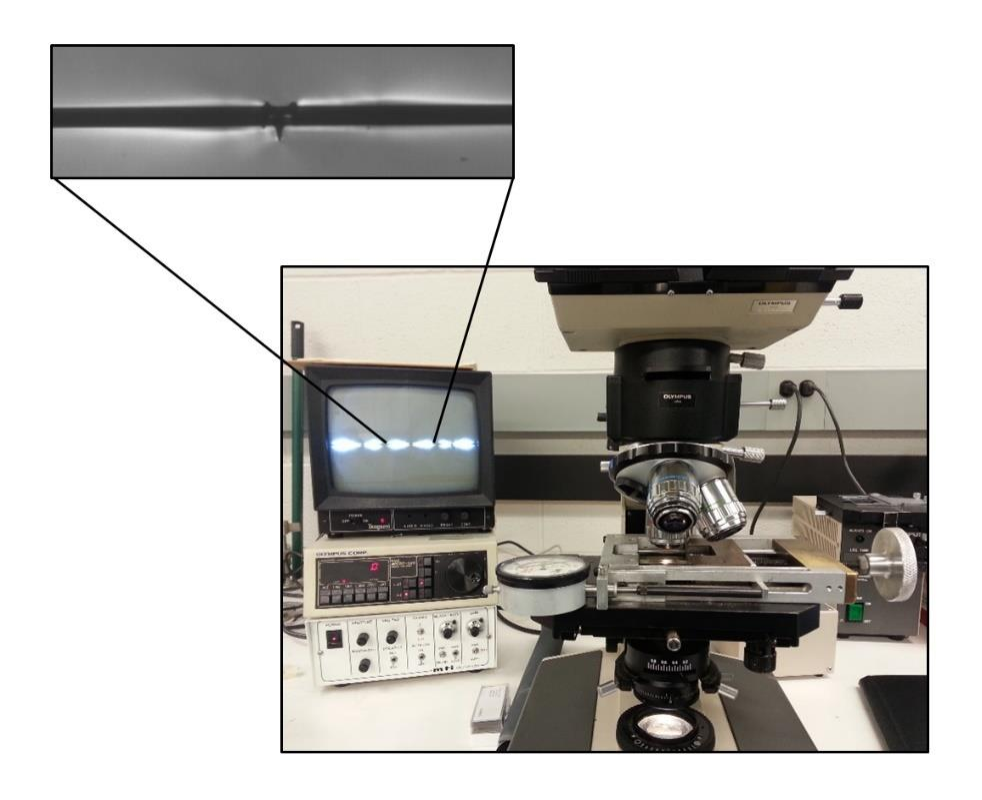


Figure 2.4: Schematic of preparation of the SFFT coupon.

The applied tensile stress (σ) on the specimen is transferred to the fiber through an interfacial shear stress mechanism [24]. When the fiber tensile strength is reached, the encapsulated fiber fractures inside the matrix. With increasing loading, the fiber will repeatedly break until the fragment length is too short to allow sufficient stress transfer to exceed the fiber breaking strength [13]. When this saturation point was reached, the number of fractures within a fixed length was determined with the optical micrometer system. A shear-lag analysis was conducted to calculate IFSS, according to Equation 1 [13,24]:

$$\tau = \left(\frac{\sigma_f}{2}\right) \left(\frac{d}{l_c}\right) \tag{1}$$

where τ is the IFSS, l_c is the fiber critical length, d is the fiber diameter and σ_f is the fiber tensile strength at the critical length. The fiber critical length is necessary to maintain the integrity of the composite material and is calculated using Equation 2 [24]:

$$l_c = \left(\frac{4}{3}\right) * \bar{l} \tag{2}$$

where \bar{l} is the average fiber fragmentation length once saturation is reached. At least 5 coupons were tested. As shown in the upper portion of Figure 2.4 using polarized light a birefringent stress pattern can be observed at the fiber-matrix interphase around the fiber breaks, which is a qualitative indicator of the level of adhesion.

2.4 Results and discussion

2.4.1 CNC surface modification with APTES

Figure 2.5 displays the FTIR spectra for the CNC and APTES-CNC. The CNC spectrum shows bands that are consistent with the spectrum of cellulose: the peaks around 3700-3000 cm⁻¹ correspond to the hydrogen-bonded OH stretching and the peak around 2900 cm⁻¹ is attributed to the CH stretching. The OH bending of adsorbed water is observed around 1640 cm⁻¹, the bending of CH₂ is displayed at 1426 cm⁻¹, and the C–O stretching around 1052 and 1030 cm⁻¹ [20,25]. The surface modification of cellulose fibers by APTES initiates when the triethoxysilane is hydrolyzed yielding ≡Si–OH–bearing oligomers [26]. These silanol groups interact by strong hydrogen bonds with the hydroxyl groups –OH of the cellulose and are converted into covalent ≡Si–O–C≡ bonds by a condensation reaction when heated above 100°C [26]. In this study, the hydrolysis of triethoxysilane was possible due to the presence of the residual water from the solvent exchange process, as observed by Lu *et al.* [21], and the FTIR spectra for APTES-CNCs show bands that

confirm the effectiveness of the surface treatment. The spectrum for APTES-CNC dried at RT for 24h is displayed in Figure 2.5 and shows peaks characteristics of amine groups at 1565 and 1482 cm⁻¹, indicating that there is hydrogen bonding between the amine groups and the hydroxyl groups of both silanol and cellulose [25]. Un-reacted silanol groups can be noticed in a weak band at 999 cm⁻¹. It is difficult to identify the Si–O–Si band since it overlaps with the C–O of cellulose at 1030cm⁻¹. Other authors report an increase of this peak after silane treatment indicating an evidence of silane adsorption [20,25].

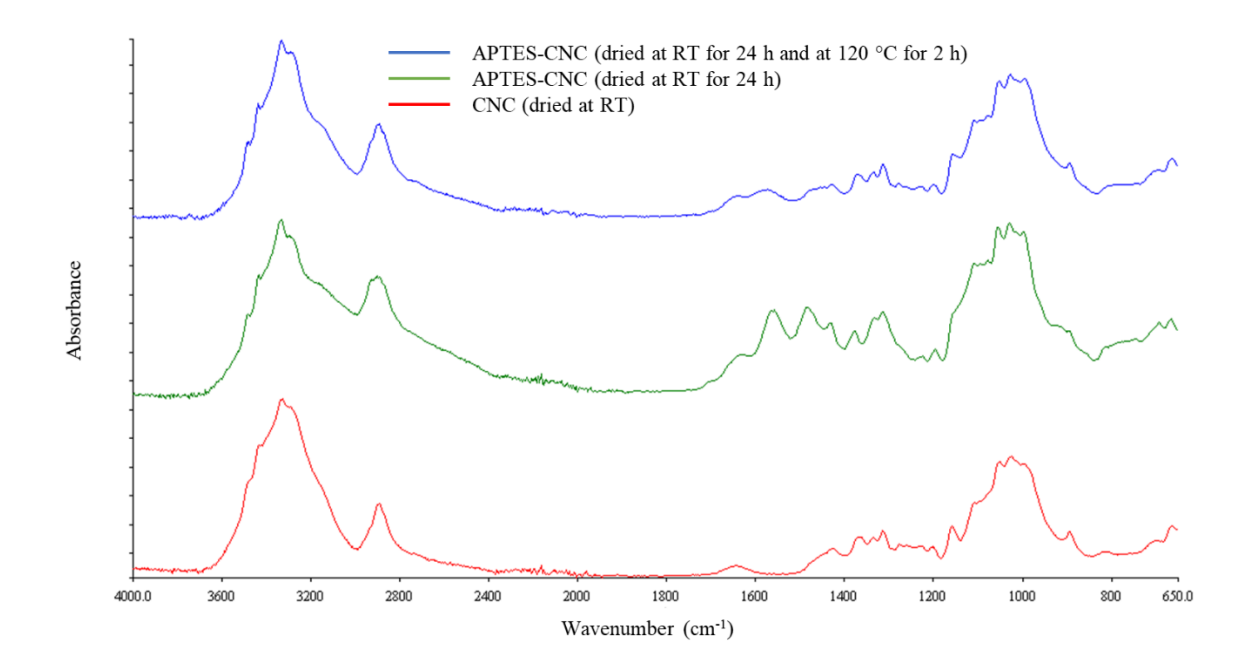
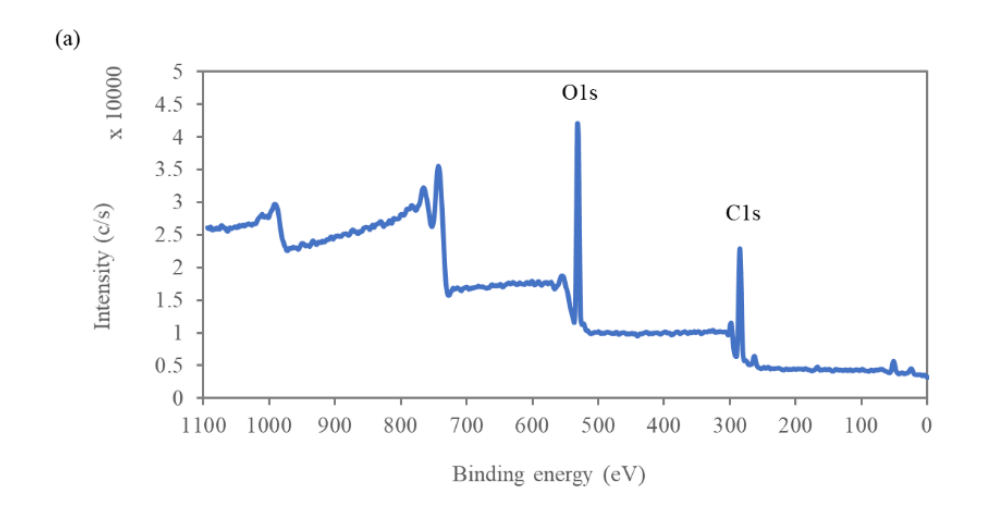


Figure 2.5: FTIR spectra for CNC, APTES-CNC (dried at RT for 24h) and APTES-CNC (dried at RT for 24h and at 120 °C for 2h).

The APTES-CNC that received additional heat treatment at 120 °C for 2 h exhibited some differences in the spectrum, as shown in Figure 2.5. The band at 1565 cm⁻¹ was shifted to a higher frequency at around 1580 cm⁻¹. This result agrees with other authors that observed that the amino groups could react with the carbonyl groups on cellulose (existing and produced during the heat

treatment) to form imines [25,27]. The differences observed on APTES-CNC spectra compared to CNC spectrum confirm that the silane treatment successfully introduced functional groups onto the CNC surface.

XPS analysis was conducted to obtain quantitative and chemical information on the surface composition of the CNC and APTES-CNC. Figure 2.6 presents for both samples the wide-scan survey spectra with elemental assignments. The spectrum for treated CNC detected peaks assigned to silicon (Si2p, Si2s) and nitrogen (N1s) elements, which are characteristic of APTES.



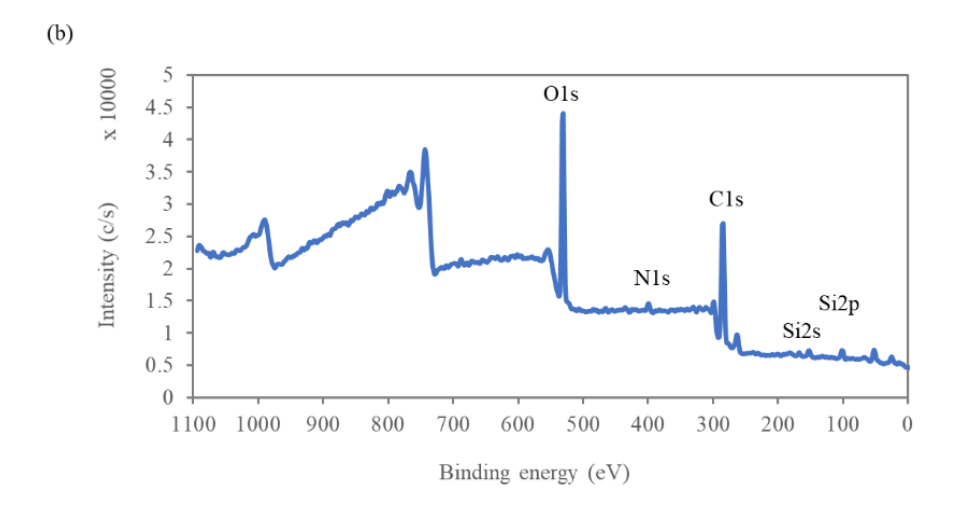


Figure 2.6: XPS survey of (a) CNC and (b) APTES-CNC.

Table 2.1 provides the elemental atomic composition and the oxygen to carbon ratio (O/C) of CNC and APTES treated sample. After treatment, silicon content increased from 0 to 3.3% and nitrogen content increased from 0 to 3.1%. Even after the Soxhlet extraction process, there are still significant amounts of silicon and nitrogen present on the cellulose surface, which indicates that APTES reacted chemically with the CNCs. As a result of the silane treatment, the O/C ratio decreased from 0.78 for CNC to 0.65 for APTES-CNC due the bonding of APTES on the surface of the CNCs.

Table 2.1: O/C ratio and element composition in percent for CNC and APTES-CNC.

Sample	O/C	C1s	N1s	O1s	Si2p
CNC	0.78	55.5	0	43.2	0
APTES-CNC	0.65	56.9	3.1	36.7	3.3

The deconvolution of C1s peak for CNC and APTES-CNC are given in Figure 2.7. Table 2.2 summarizes the relative amount of C1s components, which includes C1: C-C, C2: C-O and C3: O-C-O. Surface modification changed the relative amount of C1s components. The C1 relative amount increased from 11.9% for CNC up to 32.0% for the APTES-CNC. The increase in C1 can be assigned to the propyl groups on APTES that was attached to CNC during the treatment [21,25]. The intensity of C2 peak decreased and C3 slightly increased. These changes on the relative amount of C1s components clearly show that chemical bonds between APTES and CNCs were created. The XPS results confirm chemical functionalization of the CNC by the APTES treatment.

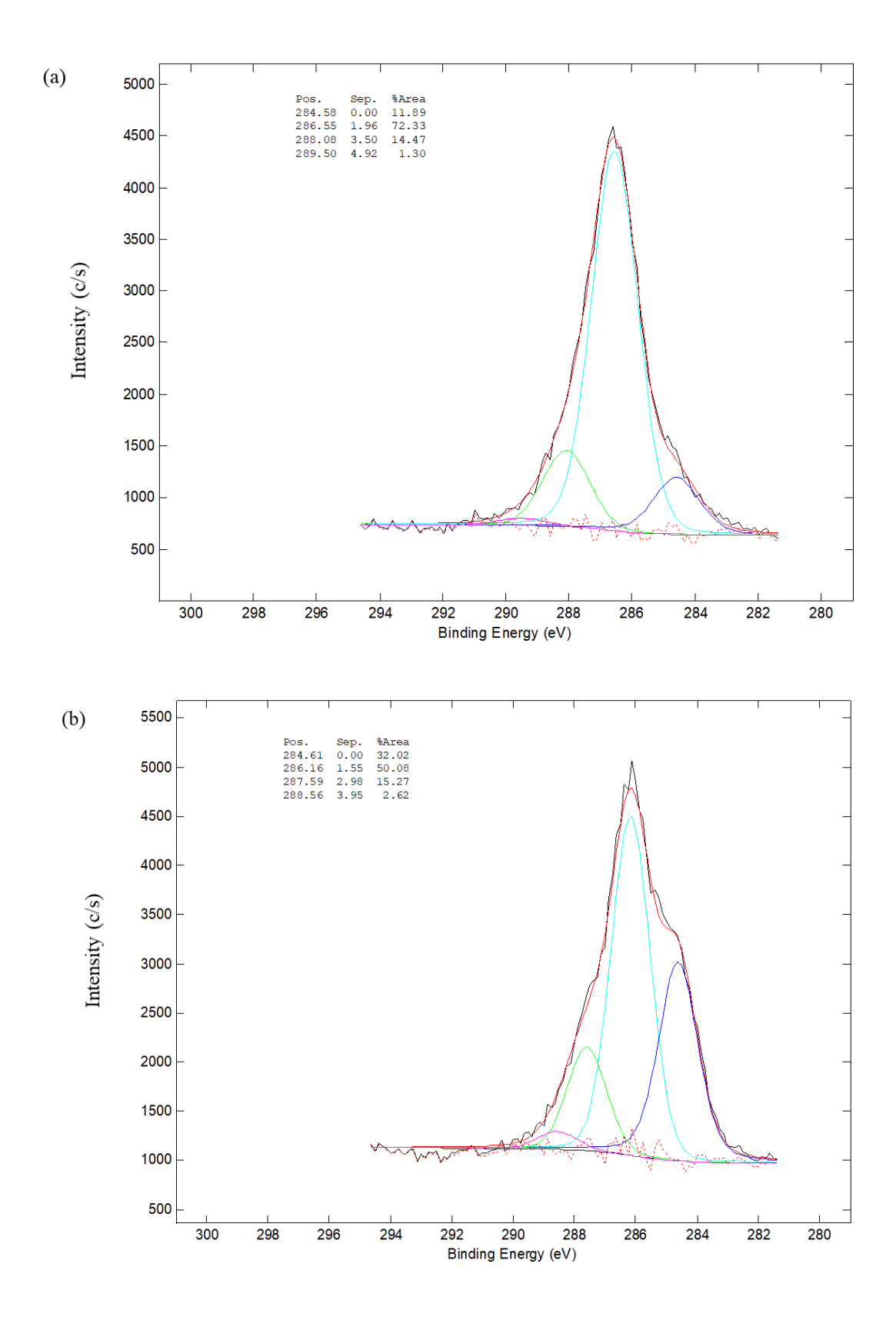


Figure 2.7: Deconvolution of C1s peak for (a) CNC and (b) APTES-CNC.

Table 2.2: Relative amount of C1s components (%) for CNC and APTES-CNC.

Sample	C1	C2	C3
CNC	11.9	72.3	14.5
APTES-CNC	32.0	50.1	15.3

2.4.2 Characterization of APTES-CNC sized CFs

Figure 2.8 shows SEM images of unsized CF and epoxy-only sized CF, and both exhibit similar surfaces with grooves and ridges that are common on CFs produced by spinning of the PAN precursor. When APTES-CNCs were added into the sizing, the micrographs (Figure 2.9 and Figure 2.10) show that the nanoparticles covered the CFs surface and exhibited a specific topography that resembles a web-like structure. Figure 2.9 shows the surface of the 12k tow sized CFs at different APTES-CNC concentrations and at different magnifications. In a typical hand dipping sizing process, the outside of the tow exhibited higher coverage while fibers on the interior of the tow exhibited lower coverage. This may be a result of the 12k carbon fibers being close together in the tow where the sizing was not able to completely diffuse into the tow interior. This could be addressed by using a continuous fiber sizing tower system that constantly spreads the tow of CFs as much as possible using rollers while being sized [12]. The micrographs were taken from fibers harvested from intermediate regions of the tow and CFs with CNC-free portions still could be observed.

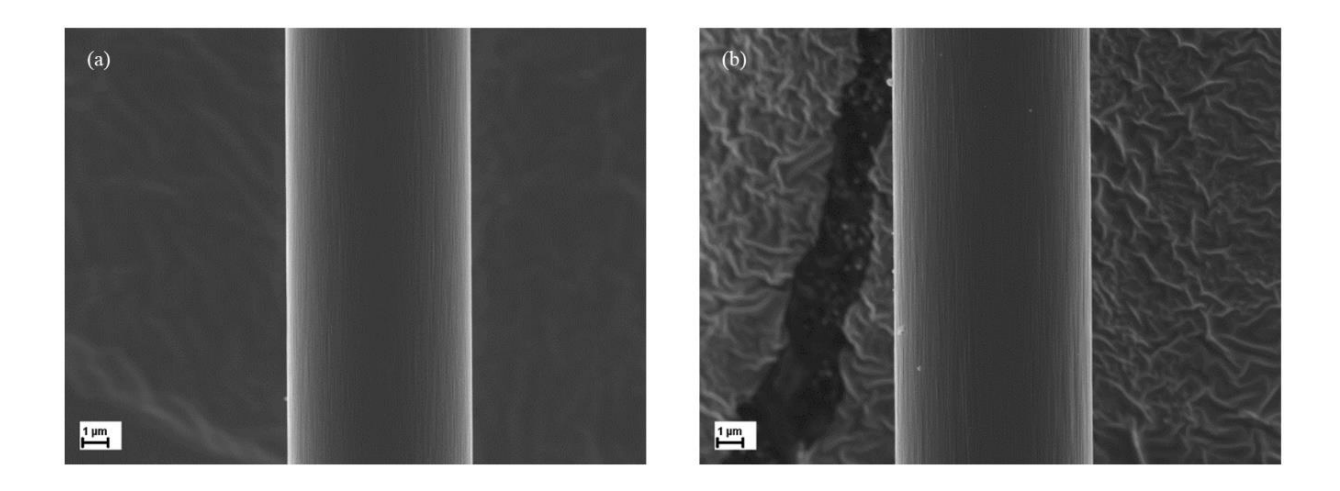


Figure 2.8: FIB-SEM micrographs of a) unsized CF and b) epoxy-only sized CF.

Figure 2.9(a) shows that a sizing was formed on the surface of the CFs sized at 0.6 wt% APTES-CNC and Figure 2.9(b) shows that the 1.0 wt% APTES-CNC sizing exhibited some regions where a considerable epoxy coating, which also contains APTES-CNCs, could be observed (identified by white arrow). It can be clearly noted that the epoxy resin permeates the CNCs, suggesting strong interaction between the resin and the functionalized nanoparticles. This configuration is correlated with a large improvement in the IFSS as will be discussed later in Section 2.4.3. At 2.0 wt% APTES-CNC (Figure 2.9(c)), there is an excess of nanoparticles in some regions and more bridging between the single fibers (red arrow). Excess coverage when using high concentrations of nanoparticles were reported in other work [17].

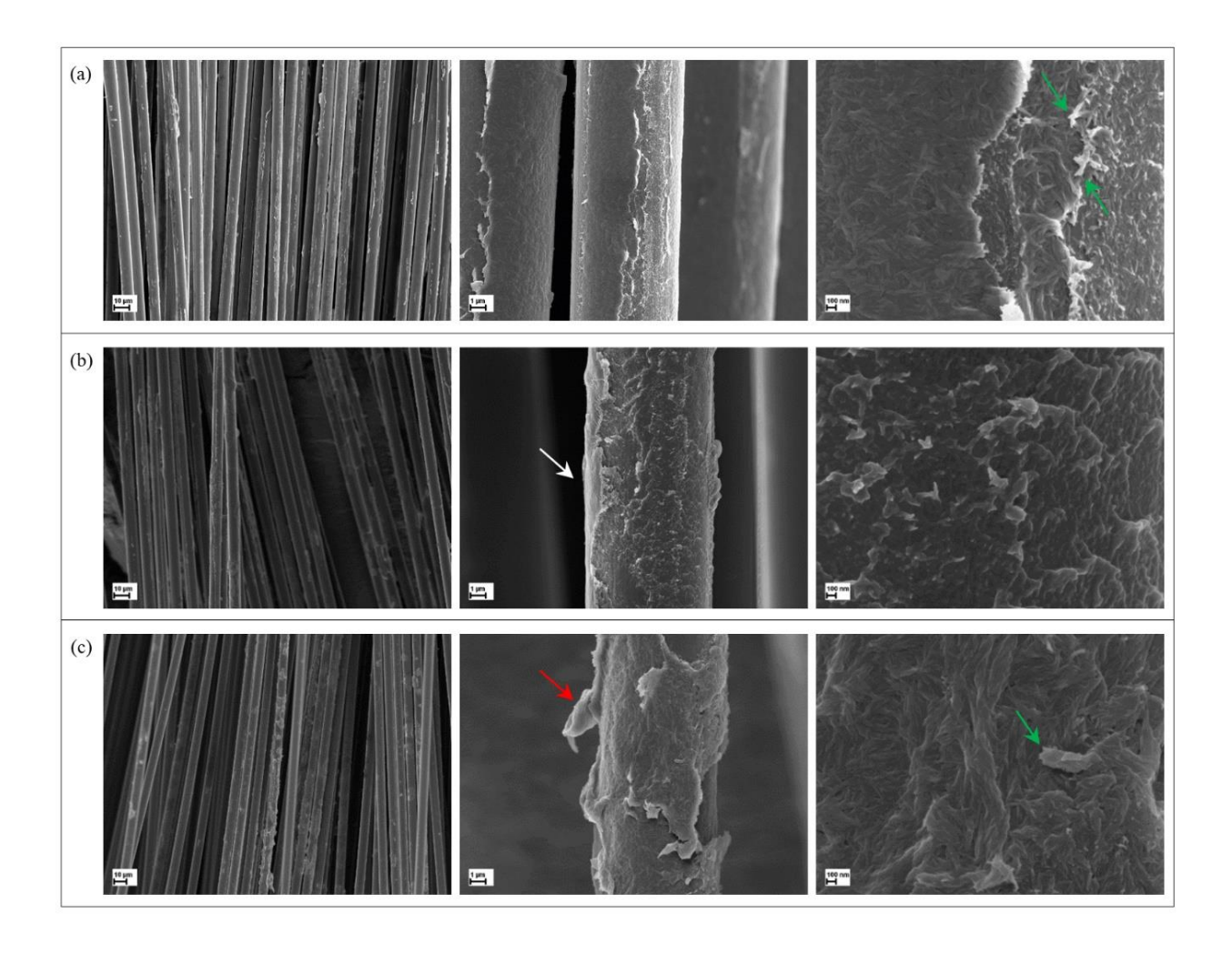


Figure 2.9: FIB-SEM micrographs for the 12k tow sizing technique of a) 0.6 wt% APTES-CNC sized CF, b) 1.0 wt% APTES-CNC sized CF and c) 2.0 wt% APTES-CNC sized CF.

At higher magnification in Figure 2.9 (green arrow), it is possible to identify CNC free ends that are derived from the network substructure, and as reported by others using MFC [28], these free ends offer physical anchoring sites for the epoxy while also providing broad area for chemical interactions. Overall, the surface of the APTES-CNC sized CFs exhibited a specific topography, with more roughness compared to the unsized CF and epoxy-only sized CF.

In the individual sizing technique, the individual CF surface was immersed in the sizing solution for a longer time. Figure 2.10 shows the individual CFs sized at 0.6 wt%, 1.0 wt% and

2.0 wt% APTES-CNC. It can be noted that this technique avoids bridging between the CFs and also avoids deforming the sizing when the 12k CF tow is opened for analysis, as was observed in the previous technique. A concentration of 0.6 wt% APTES-CNC was able to form a sizing on the surface of CFs as can be noted in Figure 2.10(a). For 1.0 wt% APTES-CNC (Figure 2.10(b)) it is possible to observe a considerable epoxy coating, which also contains APTES-CNCs. For 2.0 wt% APTES-CNC (Figure 2.10(c)), there is a dense coverage, as a result of the higher concentration, lengthy immersion and exposure of the CF surface into the sizing. This dense coating can impact the mechanical properties, as will be discussed in Section 3.3. Overall, both sizing techniques are effective and simple methods for sizing CF.

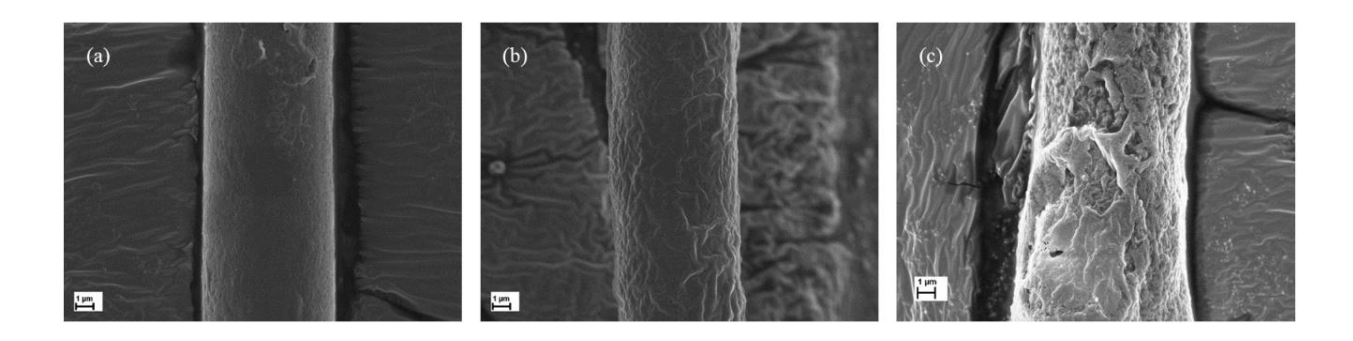
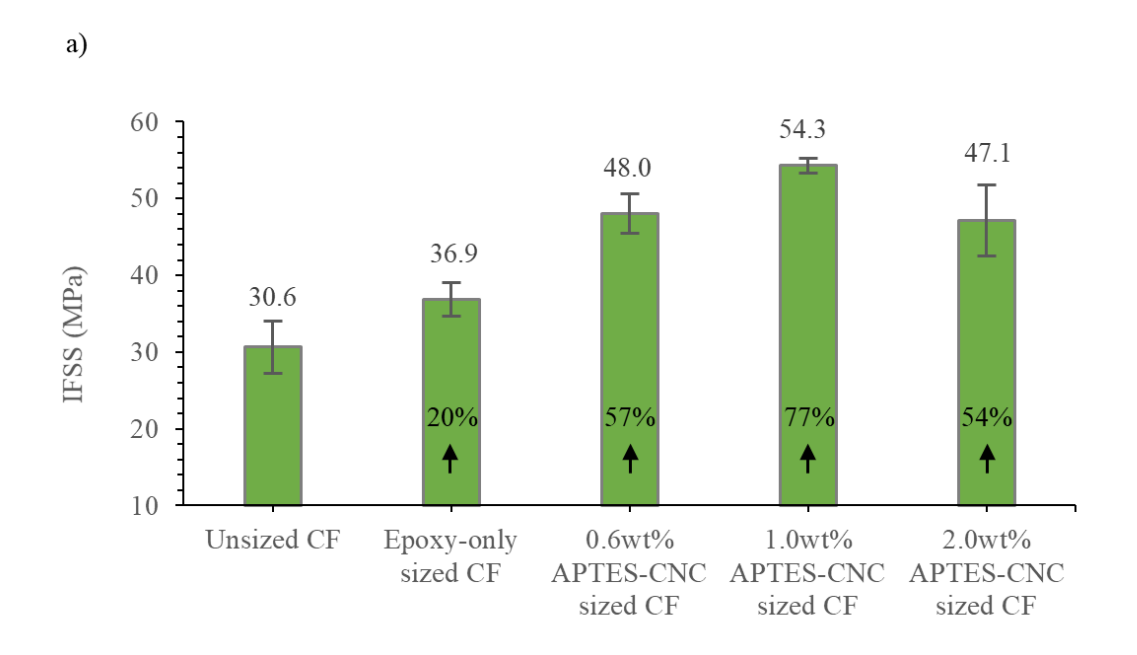


Figure 2.10: FIB-SEM micrographs for the individual sizing technique of a) 0.6 wt% APTES-CNC sized CF, b) 1.0 wt% APTES-CNC sized CF and c) 2.0 wt% APTES-CNC sized CF.

2.4.3 Evaluation of the IFSS by adding APTES-CNCs at the composite interphase

Figure 2.11 presents the IFSS calculated according to Equation 1 and Equation 2 for the 12k tow sized CFs and individually sized CFs. The percent increase of the IFSS was calculated using the unsized CFs as reference. For both techniques, the epoxy-only sized CFs exhibited higher IFSS compared to unsized CFs. This is the result of the epoxy coating having a lower concentration

of curing agent than the bulk matrix, which diffuses to the fiber surface from the bulk and forms an interphase with a concentration gradient [5]. It generates a gradual change in the properties and a stiffer interphase for improved shear transfer onto the fiber surface.



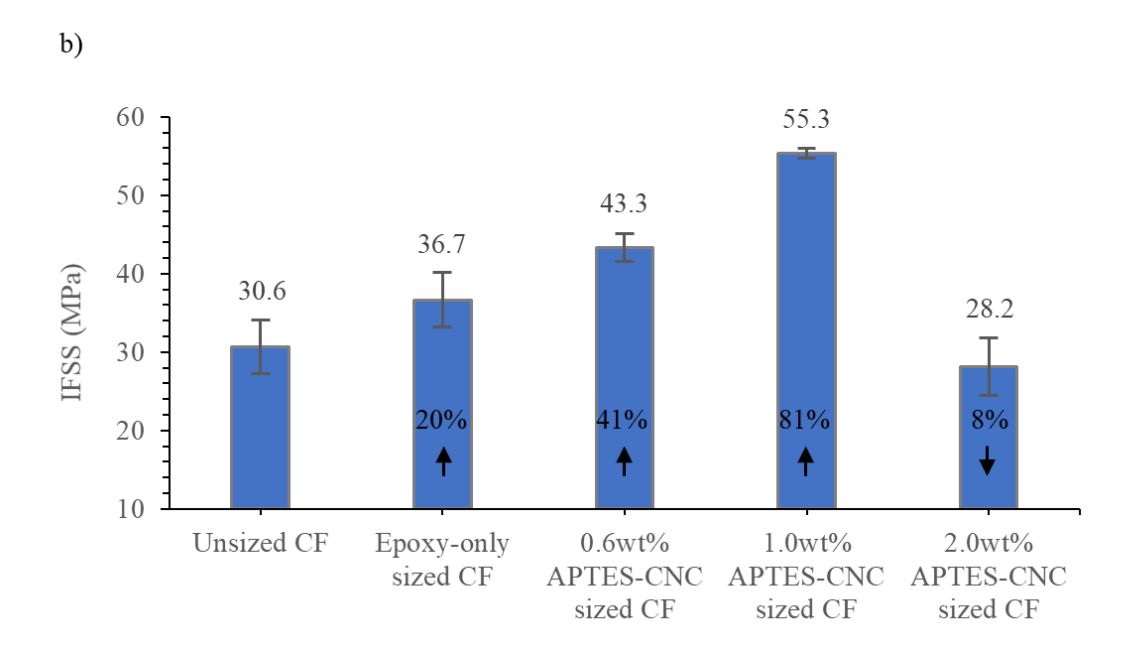


Figure 2.11: IFSS for the a) 12k tow sized CFs and b) individually sized CFs.

The incorporation of APTES-CNCs at the interphase has promoted an increase of the IFSS, which indicates the high efficacy of the nanoparticles in promoting good stress transfer from the matrix to the fiber. The effect of adding only 0.6 wt% APTES-CNC showed a considerable increase on the IFSS of 57% and 41% for the 12k tow sized CF and individually sized CF, respectively. The optimum improvement was obtained at a concentration of 1.0 wt% APTES-CNC that greatly increased the IFSS in 77% and 81% for the 12k tow sized CF and individually sized CF, respectively. APTES acted as a coupling agent by improving the interactions with the epoxide groups of the matrix and increasing the fiber-matrix adhesion at the interphase. The presence of the nanoparticles at the interphase locally increased the shear modulus of the matrix, and it can increase the IFSS since it has a direct dependence on the product of the matrix strain to failure and the square root of the matrix shear modulus.

The CFs sized at 2.0 wt% APTES-CNC exhibited an increase of 54% for the 12k tow sized CF and a reduction of 8% for the individually sized CF. As shown in Figure 2.10(c), the excessive sizing pick up generates multilayers of CNCs that can cause slippage of the nanoparticles with respect to each other and decrease the efficiency of stress transfer at the interphase [29].

Table 2.3 and Table 2.4 summarize the fiber fragment aspect ratio and IFSS for the 12k tow sized CFs and individually sized CFs, respectively. They show that the lowest fiber fragment aspect ratio and hence highest IFSS was achieved for CFs sized at 1.0 wt% APTES-CNC. Only 2.0 wt% APTES-CNC individually sized CFs exhibited aspect ratio higher than the unsized CFs.

Table 2.3: Fiber fragment aspect ratio (l_c/d) and IFSS for 12k tow sized CFs.

Campla	Fiber fragment	IFSS (MPa)	IFSS relative
Sample	aspect ratio	II 33 (WIF a)	increase (%)
Unsized CF	72.9 ± 8.3	30.6 ± 3.4	-
Epoxy-only sized CF	60.1 ± 3.6	36.9 ± 2.1	20
0.6 wt% APTES-CNC sized CF	46.1 ± 2.5	48.0 ± 2.6	57
1.0 wt% APTES-CNC sized CF	40.6 ± 0.7	54.3 ± 0.9	77
2.0 wt% APTES-CNC sized CF	47.2 ± 4.4	47.1 ± 4.6	54

Table 2.4: Fiber fragment aspect ratio (l_c/d) and IFSS for individually sized CFs.

Campla	Fiber fragment	IECC (MD _o)	IFSS relative
Sample	aspect ratio	IFSS (MPa)	increase (%)
Unsized CF	72.9 ± 8.3	30.6 ± 3.4	-
Epoxy-only sized CF	60.7 ± 5.9	36.7 ± 3.5	20
0.6 wt% APTES-CNC sized CF	51.0 ± 2.1	43.3 ± 1.7	41
1.0 wt% APTES-CNC sized CF	39.9 ± 0.4	55.3 ± 0.6	81
2.0 wt% APTES-CNC sized CF	79.4 ± 9.6	28.2 ± 3.7	-8

Overall, CNC surface modification with silane and the addition of functionalized nanoparticles at the interphase proved to be an effective method to enhance the interfacial adhesion of composites. The increase in adhesion could be attributed to the increase in the interphase

modulus resulting from the incorporation of CNCs in the epoxy-CF interphase combined with strong chemical bonding generated by the APTES at the interphase.

2.4.4 Interfacial failure mode analysis

Figure 2.12 shows representative micrographs of the birefringent stress patterns at saturation in the SFFT for the 12k tow sized CFs at different magnification. Figure 2.12(a) shows that the fracture of unsized CFs occurred mostly by frictional de-bonding. It is characteristic of weak interfaces, and results in low IFSS, as described in Section 3.3. The epoxy sizing has changed the birefringence pattern, as evidenced by the shorter fragment length along the CF and a crack propagation into the matrix perpendicular to the fiber (Figure 2.12(b)). For the APTES-CNC sized CFs there was no obvious de-bonding (Figure 2.12(c-e). Instead, the birefringence patterns for CFs sized with nanoparticles was characteristic of very strong adhesion and a well bonded interphase, evidenced by the extensive crack propagation into the matrix, that correlates to the highest level of adhesion at the interphase. This birefringence pattern supports the findings of the highest levels of IFSS being associated with APTES-CNC sized CFs, as presented in Figure 2.11 (a).

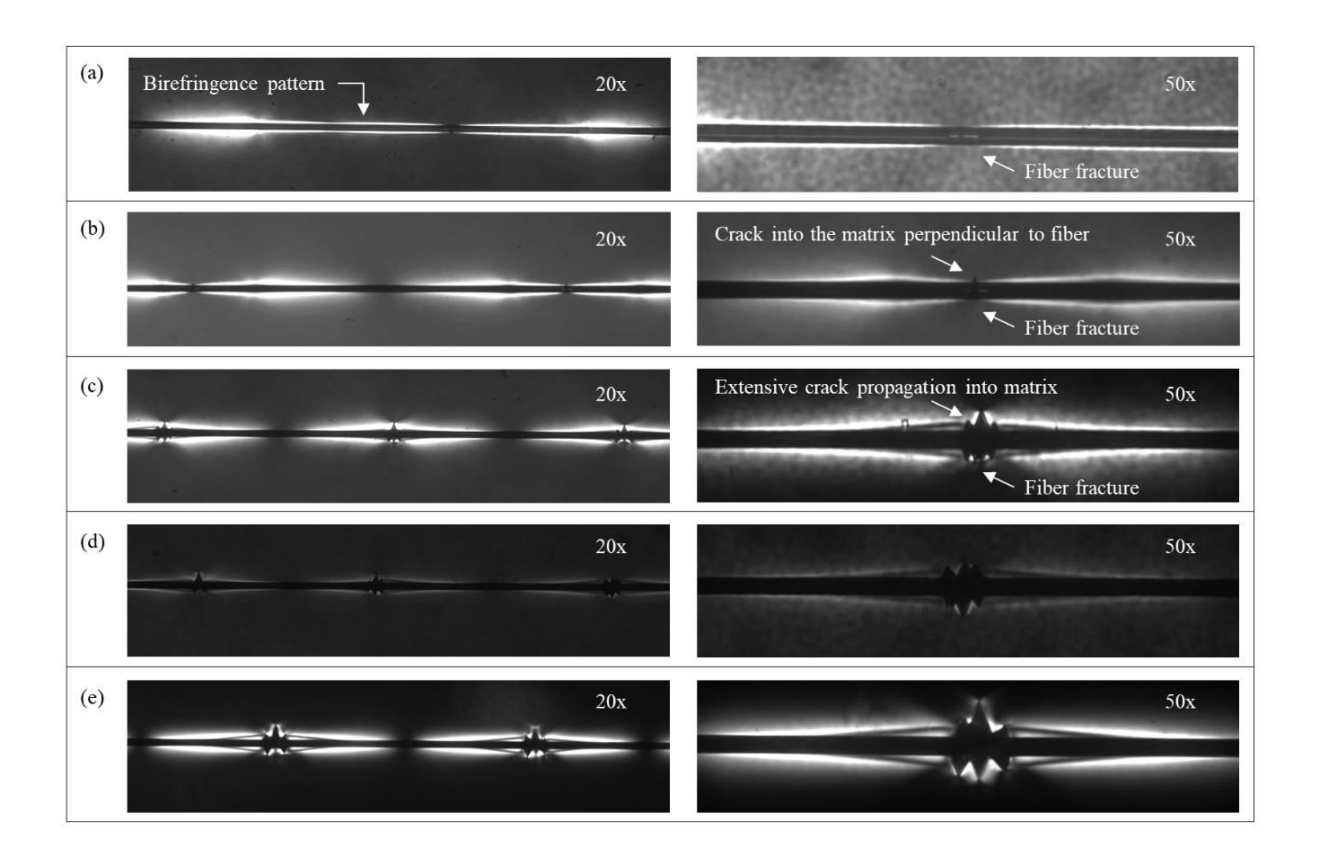


Figure 2.12: Transmitted light optical micrographs of the birefringence pattern at 20x and 50x for a) unsized CF, b) epoxy-only sized CF and 12k tow sized CF at c) 0.6 wt% APTES-CNC, d) 1.0 wt% APTES-CNC and e) 2.0 wt% APTES-CNC.

2.5 Conclusions

This work has shown that the incorporation of CNCs at a CF-epoxy interphase can increase matrix-fiber adhesion. CNCs were successfully functionalized with APTES and the presence of APTES-CNC at the interphase greatly enhanced the stress transfer from the matrix to the fiber. The increase in the IFSS was achieved by the establishment of covalent bonding and by the increase of the modulus at the composite interphase. An optimal sizing concentration for CFs sized with 1.0 wt% APTES-CNCs in the sizing resulted in an IFSS increase of 77% and 81% for the 12k

tow sized CF and individually sized CF, respectively, as well as an improvement of the failure mode.

In summary, beneficial effects of adding APTES-CNCs as a sizing for CF-epoxy matrix composites were shown. The process developed in this work has been shown to be a simple and effective method to size CFs and improve their adhesion in polymer composites. This technique can potentially be implemented for interfacial optimization in petroleum based as well as bio-based natural fiber composites.

REFERENCES

REFERENCES

- [1] EPA and NHTSA Set Standards to Reduce Greenhouse Gases and Improve Fuel Economy for Model Years 2017-2025 Cars and Light Trucks, 2012. https://nepis.epa.gov/Exe/tiff2png.cgi/P100EZ7C.PNG?-r+75+-g+7+D%3A%5CZYFILES%5CINDEX DATA%5C11THRU15%5CTIFF%5C00000346%5CP100EZ7C.TIF.
- [2] J. Yang, J. Xiao, J. Zeng, L. Bian, C. Peng, F. Yang, Matrix modification with silane coupling agent for carbon fiber reinforced epoxy composites, Fibers Polym. 14 (2013) 759–766. doi:10.1007/s12221-013-0759-2.
- [3] J. Karger-Kocsis, H. Mahmood, A. Pegoretti, Recent advances in fiber/matrix interphase engineering for polymer composites, Prog. Mater. Sci. 73 (2015) 1–43. doi:10.1016/j.pmatsci.2015.02.003.
- [4] L.T. Drzal, R.M. J., P.F. Lloyd, Adhesion of Graphite Flbres to Epoxy Matrices: I. The Role of Fibre Surface Treatment, J. Adhes. 16 (1982) 1–30. doi:10.1080/00218468308074901.
- [5] W. Qin, F. Vautard, P. Askeland, J. Yu, L. Drzal, Modifying the carbon fiber–epoxy matrix interphase with silicon dioxide nanoparticles, RSC Adv. 5 (2015) 2457–2465. doi:10.1002/pc.23325.
- [6] L. Tang, J.L. Kardos, A review of methods for improving the interfacial adhesion between carbon fiber and polymer matrix, Polym. Compos. 18 (1997) 100–113. doi:10.1002/pc.10265.
- [7] M.J. Rich, E.K. Drown, P. Askeland, L.T. Drzal, Surface Treatment of Carbon Fibers By Ultraviolet Light + Ozone: Its Effect on Fiber Surface Area and Topography, in: 19TH Int. Conf. Compos. Mater., 2013.
- [8] Z. Dai, F. Shi, B. Zhang, M. Li, Z. Zhang, Effect of sizing on carbon fiber surface properties and fibers/epoxy interfacial adhesion, Appl. Surf. Sci. 257 (2011) 6980–6985. doi:10.1016/j.apsusc.2011.03.047.
- [9] H.L. Cox, The elasticity and strength of paper and other fibrous materials, Br. J. Appl. Phys. 3 (1952) 72–79. doi:10.1088/0508-3443/3/302.
- [10] T.F. Cooke, High Performance Fiber Composites with Special Emphasis on the Interface: A Review of the Literature, J. Polym. Eng. 7 (1987).
- [11] V. Rao, L.T. Drzal, The dependence of interfacial shear strength on matrix and interphase properties, Polym. Compos. 12 (1991) 48–56. doi:10.1002/pc.750120108.
- [12] W. Qin, F. Vautard, L.T. Drzal, J. Yu, Mechanical and electrical properties of carbon fiber

- composites with incorporation of graphene nanoplatelets at the fiber-matrix interphase, Compos. Part B Eng. 69 (2015) 335–341. doi:10.1016/j.compositesb.2014.10.014.
- [13] L.T. Drzal, M. Madhukar, Fibre-matrix adhesion and its relationship to composite mechanical properties, J. Mater. Sci. 28 (1993) 569–610. doi:10.1007/BF01151234.
- [14] R. Liu, WenBo; Zhang, Shu; Li, Bichen; Yang, Fan; Jiao, WeiCheng; Hao, LiFeng; Wang, Improvement in Interfacial Shear Strength and Fracture Toughness for Carbon Fiber Reinforced Epoxy Composite by Fiber Sizing, Polym. Compos. 35 (2013) 482–488.
- [15] K.Y. Lee, P. Bharadia, J.J. Blaker, A. Bismarck, Short sisal fibre reinforced bacterial cellulose polylactide nanocomposites using hairy sisal fibres as reinforcement, Compos. Part A Appl. Sci. Manuf. 43 (2012) 2065–2074. doi:10.1016/j.compositesa.2012.06.013.
- [16] B.E.B. Uribe, A.J.F. Carvalho, J.R. Tarpani, Low-cost, environmentally friendly route to produce glass fiber-reinforced polymer composites with microfibrillated cellulose interphase, J. Appl. Polym. Sci. 133 (2016). doi:10.1002/app.44183.
- [17] W. Qin, F. Vautard, L.T. Drzal, J. Yu, Modifying the carbon fiber-epoxy matrix interphase with graphite nanoplatelets, Polym. Compos. 37 (2016) 1549–1556. doi:10.1002/pc.23325.
- [18] W. Qin, F. Vautard, P. Askeland, J. Yu, L.T. Drzal, Incorporation of silicon dioxide nanoparticles at the carbon fiber-epoxy matrix interphase and its effect on composite mechanical properties, Polym. Compos. (2015). doi:10.1002/pc.23715.
- [19] M. Mariano, N. El Kissi, A. Dufresne, Cellulose nanocrystals and related nanocomposites: Review of some properties and challenges, J. Polym. Sci. Part B Polym. Phys. 52 (2014) 791–806. doi:10.1002/polb.23490.
- [20] H. Kargarzadeh, R.M. Sheltami, I. Ahmad, I. Abdullah, A. Dufresne, Cellulose nanocrystal: A promising toughening agent for unsaturated polyester nanocomposite, Polym. (United Kingdom). 56 (2015) 346–357. doi:10.1016/j.polymer.2014.11.054.
- [21] J. Lu, P. Askeland, L.T. Drzal, Surface modification of microfibrillated cellulose for epoxy composite applications, Polymer (Guildf). 49 (2008) 1285–1296. doi:10.1016/j.polymer.2008.01.028.
- [22] F. Ansari, M. Salajková, Q. Zhou, L.A. Berglund, Strong Surface Treatment Effects on Reinforcement Efficiency in Biocomposites Based on Cellulose Nanocrystals in Poly(vinyl acetate) Matrix, Biomacromolecules. 16 (2015) 3916–3924. doi:10.1021/acs.biomac.5b01245.
- [23] R.M. Sheltami, H. Kargarzadeh, I. Abdullah, Effects of silane surface treatment of cellulose nanocrystals on the tensile properties of cellulose-polyvinyl chloride nanocomposite, Sains Malaysiana. 44 (2015) 801–810.
- [24] D. Tripathi, F.R. Jones, Review Single fibre fragmentation test for assessing adhesion in

- fibre reinforced composites, J. Mater. Sci. 33 (1998) 1–16. doi:10.1023/A:1004351606897.
- [25] J. Lu, L.T. Drzal, Microfibrillated cellulose/cellulose acetate composites: Effect of surface treatment, J. Polym. Sci. Part B Polym. Phys. 48 (2010) 153–161. doi:10.1002/polb.21875.
- [26] A. Gandini, M.N. Belgacem, Modified cellulose fibers as reinforcing fillers for macromolecular matrices, in: Macromol. Symp., 2005: pp. 257–270. doi:10.1002/masy.200550326.
- [27] M.U. de la Orden, M.C. Matías, C.G. Sánchez, J.M. Urreaga, Ultraviolet Spectroscopic Study of the Cellulose Functionalization with Silanes, Spectrosc. Lett. 32 (1999) 993–1003. doi:10.1080/00387019909350044.
- [28] B.E.B. Uribe, E.M.S. Chiromito, A.J.F. Carvalho, J.R. Tarpani, Low-cost, environmentally friendly route for producing CFRP laminates with microfibrillated cellulose interphase, Express Polym. Lett. 11 (2017) 47–59. doi:10.3144/expresspolymlett.2017.6.
- [29] A. Asadi, M. Miller, R.J. Moon, K. Kalaitzidou, Improving the interfacial and mechanical properties of short glass fiber/epoxy composites by coating the glass fibers with cellulose nanocrystals, Express Polym. Lett. 10 (2016) 587–597. doi:10.3144/expresspolymlett.2016.54.

CHAPTER 3: HYBRID CELLULOSE-INORGANIC REINFORCEMENT POLYPROPYLENE COMPOSITES: LIGHTWEIGHT MATERIALS FOR AUTOMOTIVE APPLICATIONS

Portions of this chapter were published as a journal paper in Polymer Composites Journal. The link and citation for the paper is "Reale Batista MD, Drzal LT, Kiziltas A, Mielewski D. Hybrid cellulose-inorganic reinforcement polypropylene composites: Lightweight materials for automotive applications. Polymer Composites. 2019; 1–16. https://doi.org/10.1002/pc.25439".

3.1 Abstract

Cellulose fibers are attracting considerable attention within the transportation industry as a class of reinforcing agents for polymer composites owing to their low cost, low density, high mechanical properties, and considerable environmental benefits. The objective of this study was to develop hybrid composites combining cellulose fiber with long glass fiber, short glass fiber or talc in a polypropylene (PP) matrix to optimize the overall composite properties. Tensile, flexural and notched Izod impact tests revealed that in general the mechanical properties decreased with increasing cellulose content, however, adding an optimum concentration of the cellulose fiber is a promising alternative to reduce or replace the utilization of inorganic fibers. For applications in automotive 'under-the-hood' and body interior components, the hybrid cellulose-inorganic reinforcement composite approach not only leads to superior weight and cost savings, but also environment benefits over the inorganic reinforced composites.

3.2 Introduction

The growing environmental awareness and the demand for the utilization of renewable sources to develop sustainable and recycled materials have promoted the incorporation of cellulose fibers as reinforcement for polymer composites [1]. Cellulosic fiber reinforced polymer composites have been used for many applications such as automotive components, aerospace parts, sporting goods and in the construction industry [2]. The interest in using this material is due to its sustainable nature, low cost, acceptable mechanical properties, elimination of abrasive damage to processing equipment, abundant availability and reduced health concerns [3–7].

Cellulose fiber has a lower density compared to glass fibers and talc fillers, approximately 1.5 g/cm³ versus 2.5 and 2.8 g/cm³, respectively. Therefore, its usage in the automotive industry is a central strategy for meeting light weighting and fuel economy standards. Reducing a vehicle's weight by 10 % can improve the fuel economy by 3 to 7 % [8] and contribute to attaining the CAFE standards. Despite the attractiveness of natural fiber reinforced polymer composites, they exhibit lower modulus and strength as well as inferior moisture resistance compared to synthetic fiber reinforced composites, such as glass fiber reinforced polymer composites [9].

Hybridization of cellulose fiber with inorganic fibers is one possibility to improve the mechanical properties of the composites. The advantage of combining two or more fiber types in a single matrix is that the unique properties of one type of fiber could complement what is lacking in the other [10,11]. Hybridization is also a means to combine different fiber properties to develop a multifunctional composite. In this sense, hybrid composites made with cellulose fibers possess advantages in weight reduction, sustainability and higher mechanical properties.

The objective of this study was the development of hybrid composites, investigating the effects of combining cellulose fiber with long glass fiber (LGF), short glass fiber (SGF) or talc in a polypropylene (PP) matrix. The focus was on increasing the biobased content by reducing the amount of inorganic reinforcement. The mechanical, thermal and morphological properties of the resulting composites were evaluated in terms of feasibility for automotive applications to decrease the environmental impact while maintaining the product safety, durability, and quality.

3.3 Experimental

3.3.1 Materials

PP homopolymer pellets were supplied from three commercial sources (Company X, Company Y and Company Z) listed in Table 3.1. Cellulose was obtained from a commercial source combined with PP in the form of pellets and they are named as Cellulose A and Cellulose B. They are from the same commercial source with the same composition, only with different dispersion techniques. The inorganic reinforcements were supplied in the form of master-batch pellets and their 'as received' composition can be observed in Table 3.1.

Table 3.1: As received pellets compositions.

Composition	Comments
Homopolymer PP pellets	Kindly obtained from local sources:
	Neat PP X from Company X (4.0 g/10 min, ASTM D1238)
	Neat PP Y from Company Y (37 g/10min, ISO 1133)
	Neat PP Z from Company Z (17 g/10min, ISO 1133)
30 wt. % Cellulose filled PP	Kindly provided by local source:
pellets	Cellulose A and Cellulose B. Cellulose pellets have
	hexagonal shape, a thickness of 0.1 to 1.5 mm and a length
	of 4.5 to 6.5 mm
30 wt. % LGF filled PP pellets	Used in instrumental panel substrates
40 wt. % (SGF / Mica) filled PP	Supplied by Company Y:
pellets	Melt flow: 10 g/10min (ISO 1133) / Density: 1.23 g/cm ³
	Used in console substrate
42.5 wt. % Talc filled PP pellets	Supplied by Company Y with a minimum of 25% post-
	consumer recycled content. Used in head lamp housing
33 wt. % SGF filled PP pellets	Supplied by Company Z:
	Melt flow: 4.0 g/10 min (ISO 1133)
	Used in console substrate

3.3.2 **Processing**

The composites were prepared in Ford's lab by injection molding (Boy Machines Model 80M) with the same processing conditions and the total fiber mass content was fixed at 30 wt. %, with the cellulose concentration varying gradually from 0 wt. % up to 30 wt. %. Table 3.2 summarizes the composite compositions and sample identification codes, for each constituent source. To achieve the desired inorganic reinforcement/cellulose concentration, the as received master-batch pellets from Table 3.1 were mixed and diluted with neat PP as needed.

Table 3.2: Sample identification codes and composite composition for each constituent source.

LGF / Cellulose hybrid composites				
Sample code	LGF (wt. %)	Cellulose A (wt. %)	PP from Company X	
			(wt. %)	
Neat PP X	0	0	100	
LGF/Cellulose A (30/0)	30	0	70	
LGF/Cellulose A (20/10)	20	10	70	
LGF/Cellulose A (15/15)	15	15	70	
LGF/Cellulose A (10/20)	10	20	70	
LGF/Cellulose A (0/30)	0	30	70	

(SGF / Mica) / Cellulose hybrid composites

Sample code	(SGF/Mica)	Cellulose B (wt. %)	PP from Company Y
	(wt. %)		(wt. %)
Neat PP Y	0	0	100
(SGF/Mica)/Cellulose B (30/0)	30	0	70
(SGF/Mica)/Cellulose B (20/10)	20	10	70
(SGF/Mica)/Cellulose B (15/15)	15	15	70
(SGF/Mica)/Cellulose B (10/20)	10	20	70
(SGF/Mica)/Cellulose B (0/30)	0	30	70

Talc / Cellulose hybrid composites

Sample code	Talc (wt. %)	Cellulose B (wt. %)	PP from Company Y
			(wt. %)
Neat PP Y	0	0	100
Talc/Cellulose B (30/0)	30	0	70
Talc/Cellulose B (20/10)	20	10	70
Talc/Cellulose B (15/15)	15	15	70
Talc/Cellulose B (10/20)	10	20	70
Talc/Cellulose B (0/30)	0	30	70

SGF / Cellulose hybrid composites

Sample code	SGF (wt. %)	Cellulose B (wt. %)	PP from Company Z
			(wt. %)
Neat PP Z	0	0	100
SGF/Cellulose B (30/0)	30	0	70
SGF/Cellulose B (20/10)	20	10	70
SGF/Cellulose B (15/15)	15	15	70
SGF/Cellulose B (10/20)	10	20	70
SGF/Cellulose B (0/30)	0	30	70

Prior to injection molding, the pellets were dried at 60° C overnight to reduce moisture content. Then they were mixed and fed into the hopper on the injection molding machine as shown on Figure 3.1. An extrusion process was not used in this research. Therefore, it is worth mentioning that this is an efficient one-step injection process that can speed up part production. To avoid cellulose degradation the maximum injection temperature was limited to 193° C (380 F). Composites were molded into ASTM test specimens and conditioned in a room at $23 \pm 2^{\circ}$ C and $50 \pm 5\%$ relative humidity for 7 days before conducting mechanical tests.

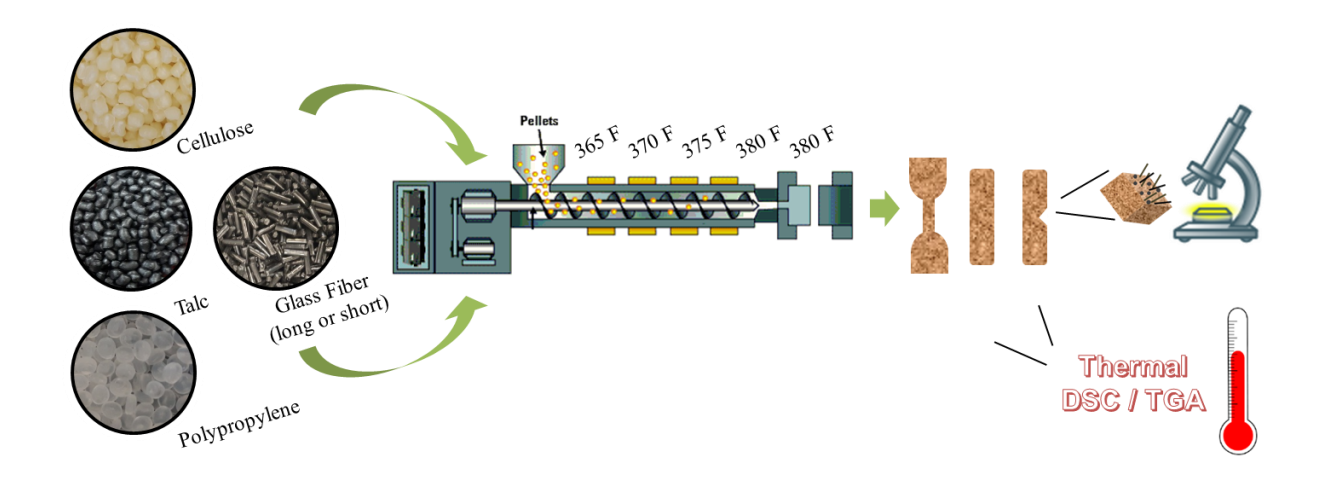


Figure 3.1: Schematic illustration of materials, processing and characterization.

3.3.3 Testing procedure and characterization

3.3.3.1 Mechanical test

Tensile and flexural tests were conducted in an Instron 3366 in compliance to ASTM D638-10 and ASTM D790-10, respectively. The tensile test used a crosshead speed of 5.0 mm/min, a 5 kN load cell and a 50 mm extensometer attached to the gauge section of the specimen

to measure the displacement. The stress at maximum load, strain at maximum load and Young's modulus were determined. At least six specimens were tested for each data set.

The flexural tests also used a 5 kN load cell, at a rate of 1.0 mm/min with a support span length of 50 mm. The stress at 5% strain and flexural modulus were determined.

The impact strength of notched Izod specimens was measured according to ASTM D256-10. Tests were conducted on a Testing Machines Inc. 43-02-03 model impact test machine with a 2 lb. pendulum, and the results are the average from ten specimens of each data set.

All the mechanical tests were run in an environmentally conditioned room at $23 \pm 2^{\circ}C$ and $50 \pm 5\%$ relative humidity.

3.3.3.2 Scanning electron microscopy (SEM)

A Carl Zeiss EVO LS 25 scanning electron microscope with accelerating voltage of 15 kV was used to observe the morphology of the impact fracture surface of the samples. The samples were sputter-coated with platinum to prevent surface charging. In the micrographs, the direction of impact is from right to left, as shown on the schematic illustration on Figure 3.2.

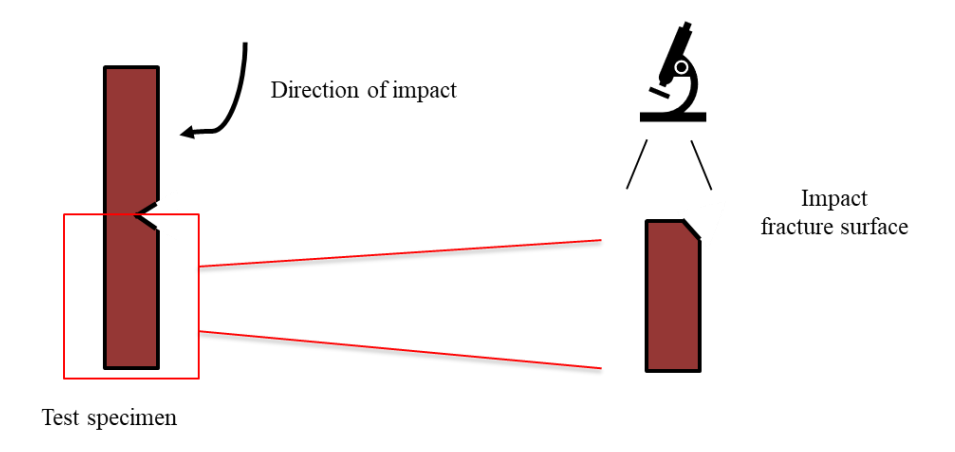


Figure 3.2: Schematic illustration of SEM analysis.

3.3.3.3 Thermal characterization

Melting and crystallization behavior of the neat polymer matrix and the composites were measured using a TA Instruments Q2000 differential scanning calorimeter. To remove the thermal history, samples were heated from room temperature to 250 °C at a rate of 20 °C/min and held isothermally at 250 °C for 5 minutes. Then, they were cooled to -50 °C at a rate of 10 °C/min and held at -50 °C for 5 minutes before reheating to 250 °C at a rate of 10 °C/min.

The melting and crystallization behavior were collected from the heat flow versus temperature curves. Melting temperature (T_m) was assigned as the peak minimum of the endothermic melt transition, and crystallization temperature (T_c) as the peak maximum of the exothermic crystallization transition. The enthalpy of melting (ΔH_m) and enthalpy of crystallization (ΔH_c) were also measured from these curves. Specimen weight was in the range of 7 to 9 mg and the results were averaged from three specimens of each sample.

The thermal stability of the neat PP and the composites was investigated by thermal gravimetric analysis (TGA) curves using a TA Instruments Q500. The thermograms were obtained under constant air flow rate of 50 mL·min⁻¹ and the samples were heated up to 600 °C at a rate of 10 °C/min. The sample weight was in the range of 8 to 10 mg. Three replicates of each sample were performed.

3.4 Results and discussion

3.4.1 Mechanical properties

3.4.1.1 Tensile properties

Figure 3.3, Figure 3.4 and Figure 3.5 show the effects of different fiber combinations on the tensile properties of the composites, along with the neat PP. Overall, the addition of inorganic fibers and cellulose led to a considerable increase in the maximum tensile stress (Figure 3.3) and Young's modulus (Figure 3.4) in comparison to the neat PP. The inorganic fibers produced the greatest improvement in these properties. An increase of 232% and 401% for tensile stress and modulus, respectively, was observed for LGF/Cellulose A (30/0) composites compared to neat PP X (Figure 3.3(a), Figure 3.4(a)). As the cellulose content was increased to replace a portion of the LGF, SGF/Mica or SGF, the tensile stress and modulus of the composites decreased. For these composites which contain glass fiber, this trend is expected due to the stronger and stiffer properties of the inorganic fiber compared to cellulose [12]. As reported in the work of Thwe and Liao [9], the tensile strength and modulus of hybrid composites of bamboo fiber and glass fiber in PP gradually increased with increasing glass fiber to bamboo fiber ratio.

It was observed that even with the incorporation of 30 wt. % cellulose, the tensile stress and modulus of the composites are still higher compared to neat PP. The addition of 30 wt. % Cellulose B promotes an increase of 18% and 129% for tensile stress and modulus, respectively, in comparison with neat PP Y (Figure 3.3(b,c), Figure 3.4(b,c)). SGF/Cellulose B (15/15) hybrid composites increased the tensile stress and modulus by 58% and 171%, respectively, in comparison with neat PP Z (Figure 3.3(d), Figure 3.4(d)) and is suitable for body interior (console

substrate, wiring harness) and under-the-hood (battery and power distribution box covers) applications.

The tensile stress at maximum load for the composites made of talc and cellulose did not follow the previous trend (Figure 3.3(c)). Talc/Cellulose B (10/20) composites exhibited an increase of 15% for the tensile stress in comparison with Talc/Cellulose B (30/0) composites, which represents an advantage of the hybrid composite over the composite reinforced with talc only.

The tensile strains at maximum load of the composites were markedly lower than neat PP (Figure 3.5) with no considerable difference in strain as a function of fiber content.

Overall, the mechanical properties in tension show that the hybridization of cellulose with inorganic reinforcements produced beneficial enhancements.

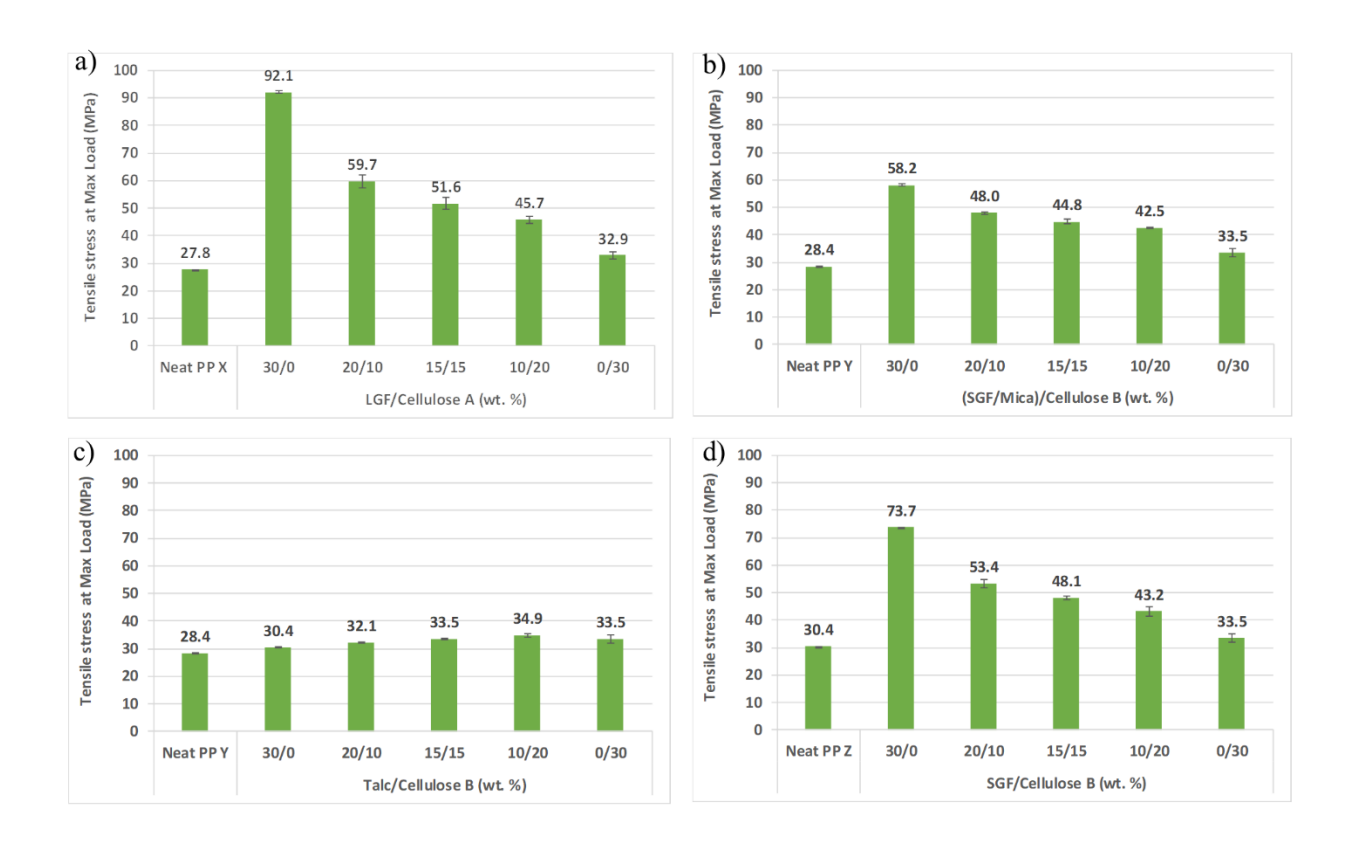


Figure 3.3: Tensile stress at maximum load of a) LGF/Cellulose A, b) (SGF/Mica)/Cellulose B, c) Talc/Cellulose B and d) SGF/Cellulose B composites along with neat PP.

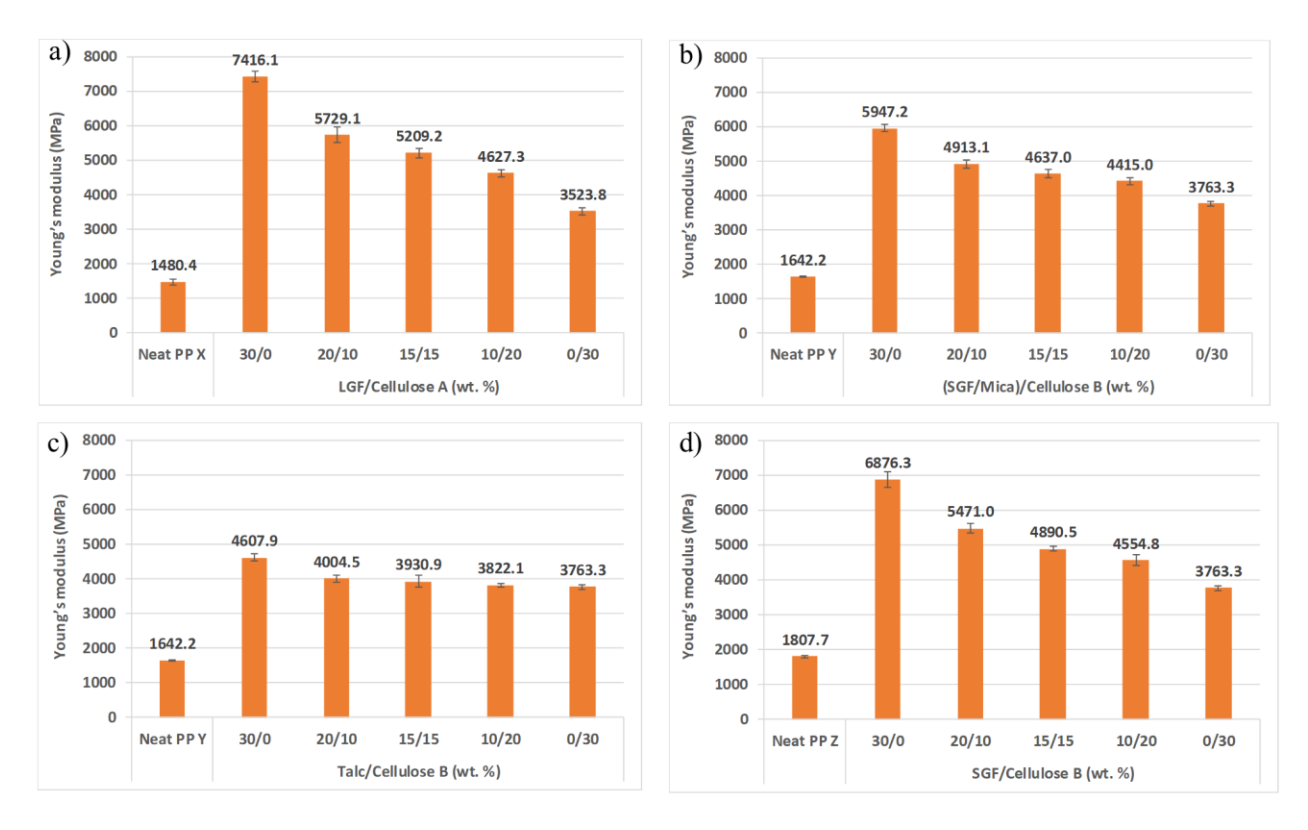


Figure 3.4: Young's modulus of a) LGF/Cellulose A, b) (SGF/Mica)/Cellulose B, c)

Talc/Cellulose B and d) SGF/Cellulose B composites along with neat PP.

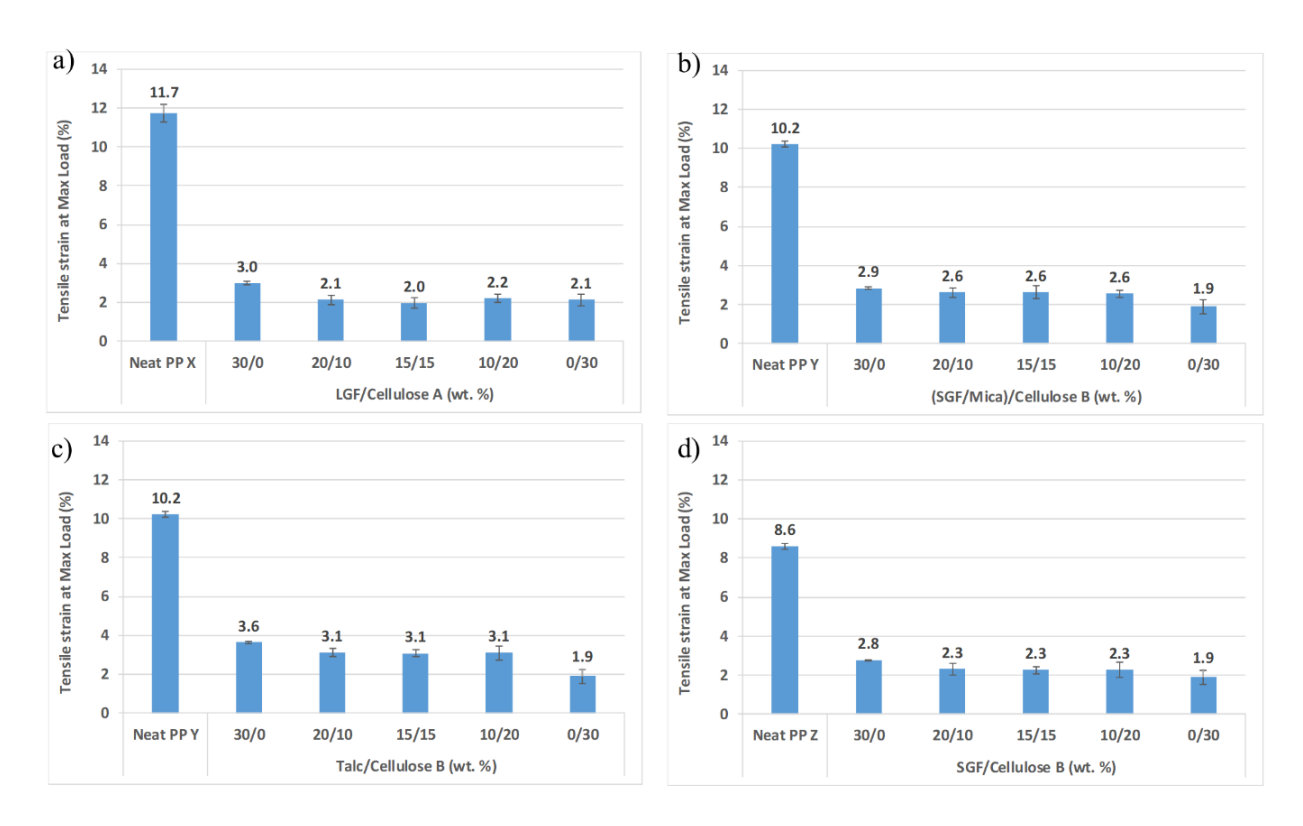


Figure 3.5: Tensile strain at maximum load of a) LGF/Cellulose A, b) (SGF/Mica)/Cellulose B, c) Talc/Cellulose B and d) SGF/Cellulose B composites along with neat PP.

3.4.1.2 Flexural properties

The Figure 3.6 and Figure 3.7 show the flexural properties of the polymer matrix and the composites. Flexural properties exhibited a similar trend as the tensile results, revealing that in general the mechanical properties decreased as the amount of cellulose increased. The stress at 5% strain achieved a 59% enhancement for LGF/Cellulose A (0/30) compared to neat PP X (Figure 3.6(a)).

The presence of cellulose increased the stress at 5% strain for Talc/Cellulose B composites (Figure 3.6(c)) with the highest strength of 56.3 MPa for Talc/Cellulose B (10/20) hybrid

composites. It represents an increase of 10% in comparison with Talc/Cellulose B (30/0) composites.

Similar to the tensile modulus results, all composites showed higher flexural modulus than neat PP (Figure 3.7).

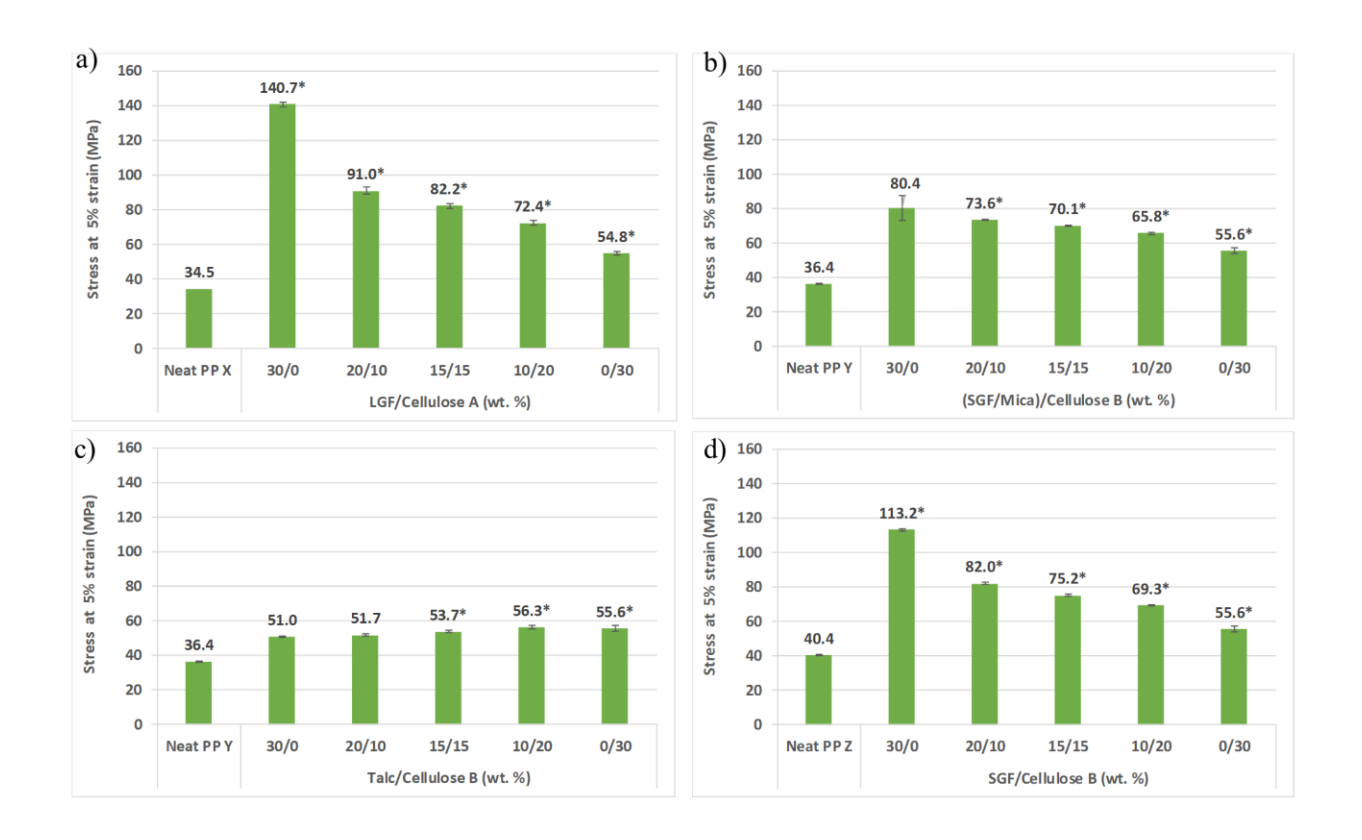


Figure 3.6: Stress at 5% strain of a) LGF/Cellulose A, b) (SGF/Mica)/Cellulose B, c) Talc/Cellulose B and d) SGF/Cellulose B composites along with neat PP. *Specimens broke before 5% strain; maximum stress value used.

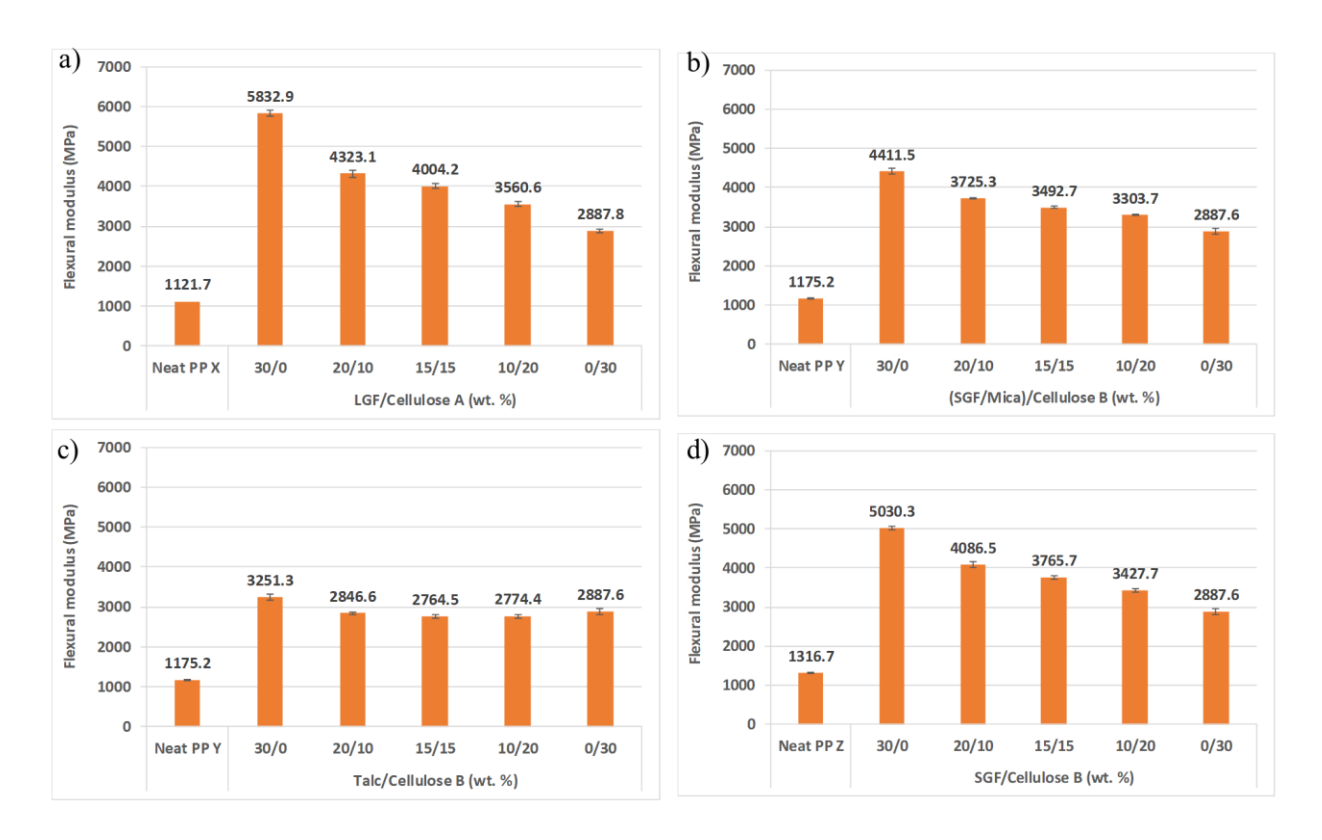


Figure 3.7: Flexural modulus of a) LGF/Cellulose A, b) (SGF/Mica)/Cellulose B, c) Talc/Cellulose B and d) SGF/Cellulose B composites along with neat PP.

3.4.1.3 Impact properties

The addition of cellulose fibers acted as stress concentrators and reduced the impact strength of the composites, as shown in Figure 3.8(a, b and d). A decrease in impact strength of PP was also observed when sisal fibers were added to PP by unnotched Izod impact test [13].

Figure 3.8(a) shows that LGF/Cellulose A (15/15) composites exhibited an impact strength 91% higher than LGF/Cellulose A (0/30). As reported by Panthapulakkal and Sain [14] for hemp/glass fiber/PP composites, the impact strength is enhanced with an increase in glass fiber content due to the improved resistance offered from the glass fibers in the composites. For the hybrid composites made of SGF/Cellulose B (Figure 3.8(d)) the impact strength is still preserved

in comparison with the neat PP Z. The SGF/Cellulose B (20/10) composites increased the impact strength by 34% and the SGF/Cellulose B (10/20) composites still exhibited 16% increase compared to neat PP Z. No change in impact strength was observed when adding cellulose to talc composites (Figure 3.8(c)).

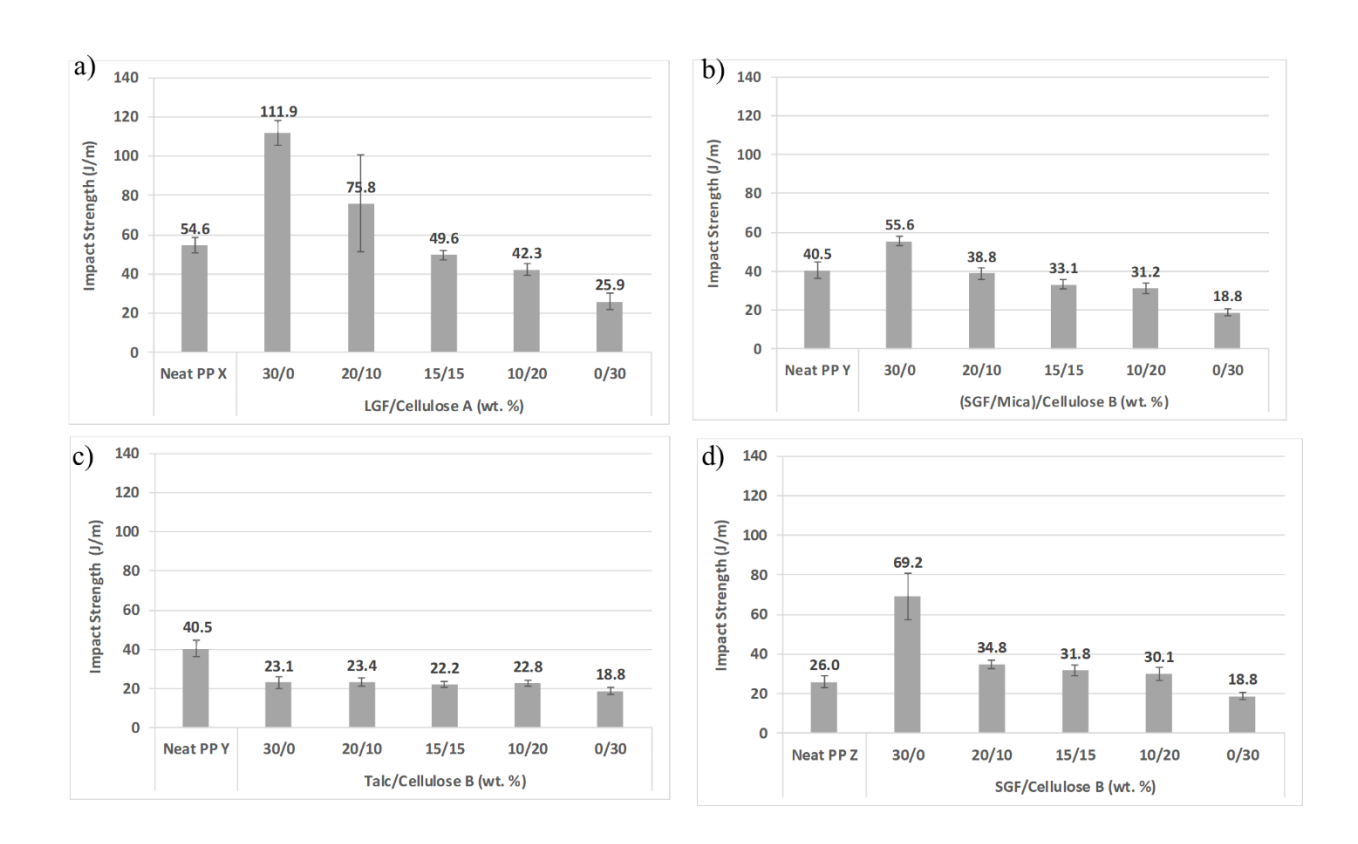


Figure 3.8: Impact strength of a) LGF/Cellulose A, b) (SGF/Mica)/Cellulose B, c) Talc/Cellulose B and d) SGF/Cellulose B composites along with neat PP.

3.4.2 Morphological properties

Figure 3.9, Figure 3.10, Figure 3.11, and Figure 3.12 show the impact fracture surface of LGF/Cellulose A, (SGF/Mica)/Cellulose B, Talc/Cellulose B and SGF/Cellulose B composites,

respectively, along with the neat PP. The samples investigated are neat PP and composites reinforced with inorganic reinforcement/cellulose at 30/0, 15/15 and 0/30 (wt.%).

It can be observed that the basic deformation mechanism of all unmodified PP is shear yielding (Figure 3.9(a), Figure 3.10(a), Figure 3.11(a), Figure 3.12(a)). There was no significant difference between the surface morphologies of the Cellulose A and Cellulose B composites (Figure 3.9(d), Figure 3.10(d), Figure 3.11(d), Figure 3.12(d). Figure 3.13 show higher magnification of the composites reinforced at 30wt. % cellulose where the width and thickness of the fiber can be observed. Since the cellulose fiber is hydrophilic, interfacial compatibility is not expected to be high. This is consistent with the micrographs of the fracture surfaces which show little evidence of interfacial interaction between the cellulose and the matrix. This incompatibility may reduce the mechanical properties and is in agreement with the reduced tensile, flexural and impact properties measured on the cellulose reinforced composites. Cellulose fiber fracture is also clear from Figure 3.9(d) and Figure 3.13.

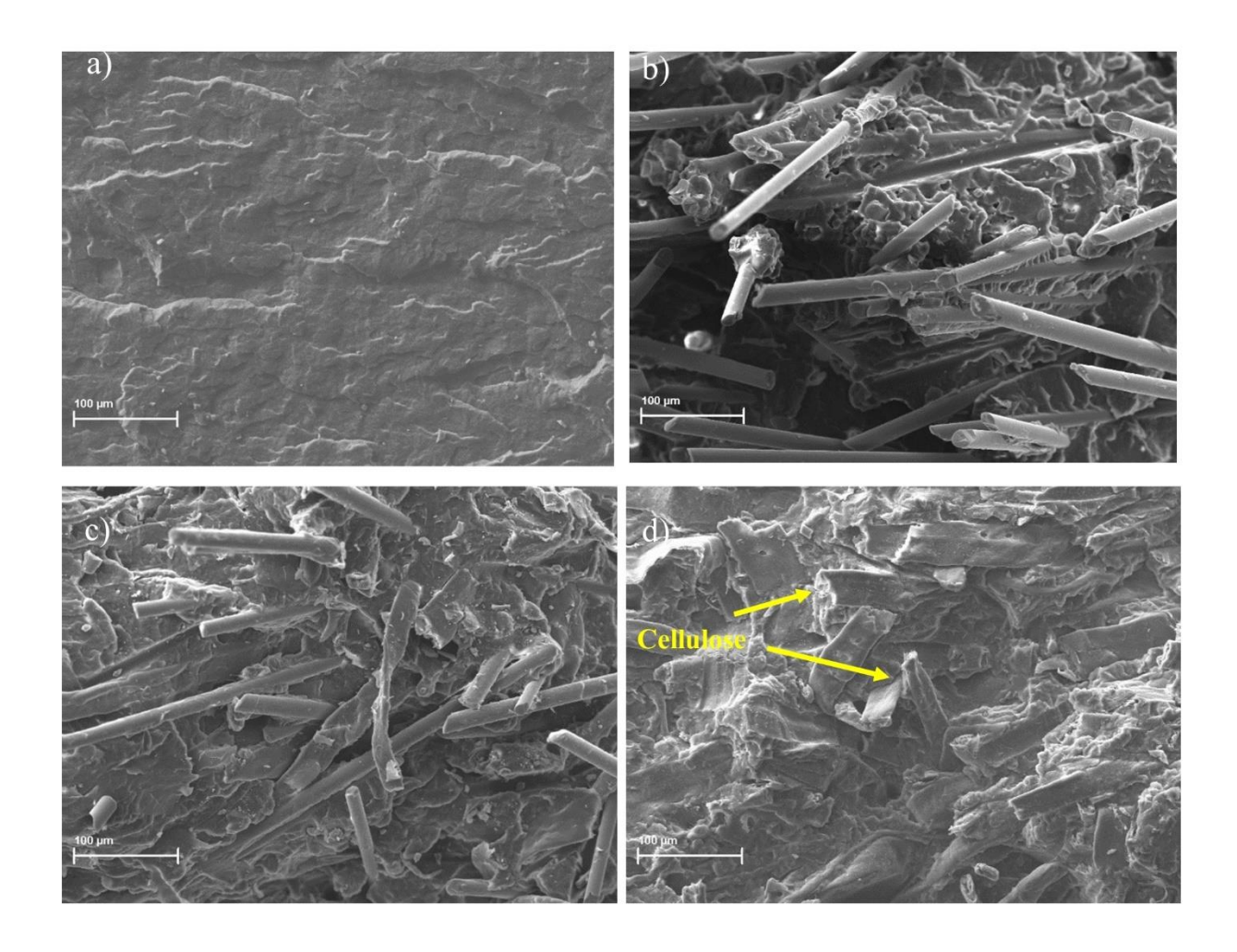


Figure 3.9: SEM micrographs of a) Neat PP X, b) LGF/Cellulose A (30/0), c) LGF/Cellulose A (15/15) and d) LGF/Cellulose A (0/30).

The micrographs of specimens reinforced with long or short glass fiber exhibited fiber pull out (Figure 3.9(b), Figure 3.10(b), Figure 3.12(b)), an indicative of poor interfacial adhesion between the glass fiber and matrix. This behavior is in agreement with results reported by Arbelaiz *et al.* [11]. The distribution of the fibers in the matrix appears to be good however.

With the incorporation of 15 wt. % cellulose (Figure 3.9(c), Figure 3.10(c), Figure 3.12(c)), holes from the pulled out glass fibers are still observed. In the SEM micrographs glass fiber can

be distinguished from cellulose by their difference in diameter. Good distribution of the hybrid fibers is observed.

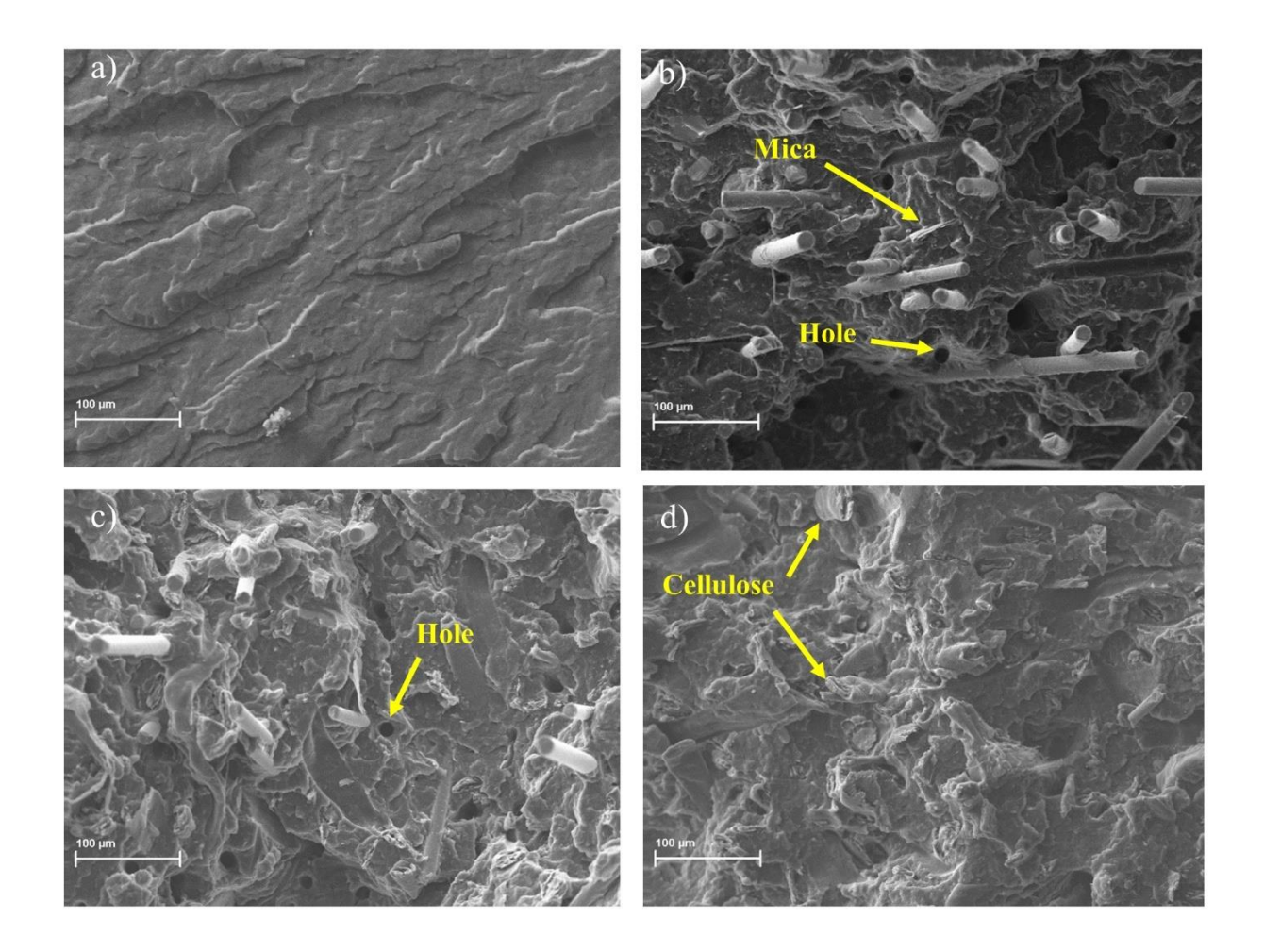


Figure 3.10: SEM micrographs of a) Neat PP Y, b) (SGF/Mica)/Cellulose B (30/0), c) (SGF/Mica)/Cellulose B (15/15) and d) (SGF/Mica)/Cellulose B (0/30).

Figure 3.10(b) identifies a mica particle and Figure 3.11(b) identifies the platelet talc filler. Micrographs show good talc distribution in the matrix with no large aggregates present.

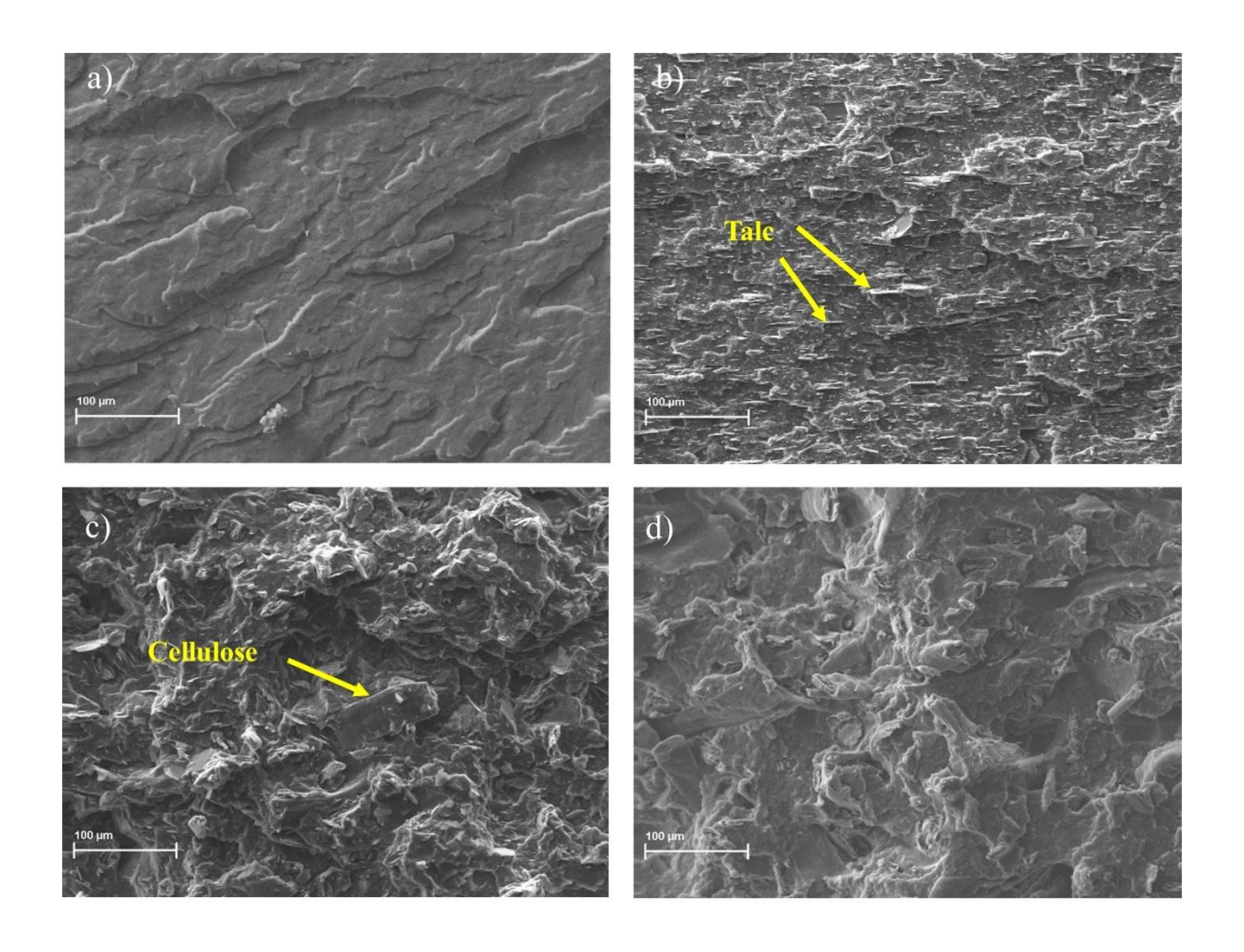


Figure 3.11: SEM micrographs of a) Neat PP Y, b) Talc/Cellulose B (30/0), c) Talc/Cellulose B (15/15) and d) Talc/Cellulose B (0/30).

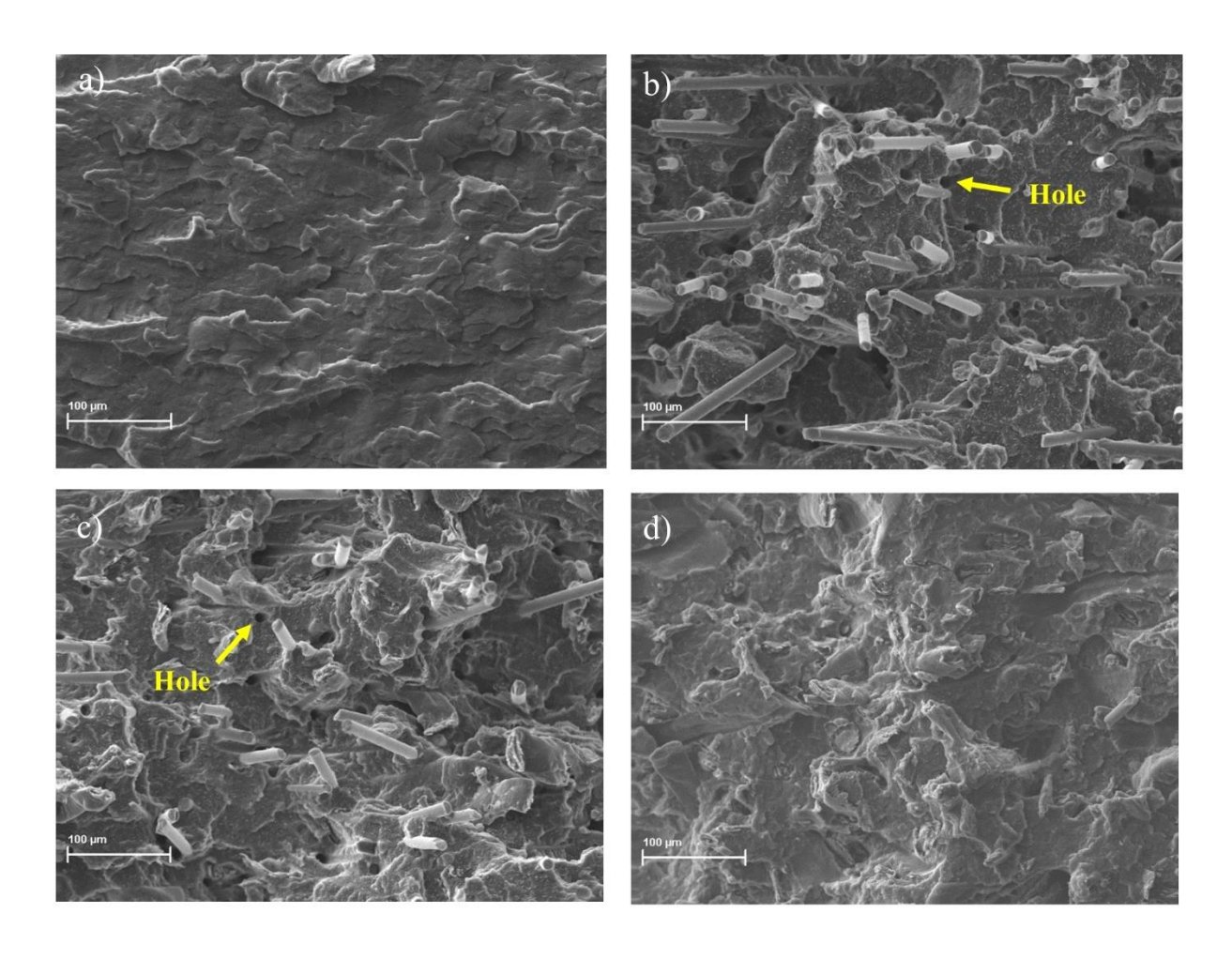


Figure 3.12: SEM micrographs of a) Neat PP Z, b) SGF/Cellulose B (30/0), c) SGF/Cellulose B (15/15) and d) SGF/Cellulose B (0/30).

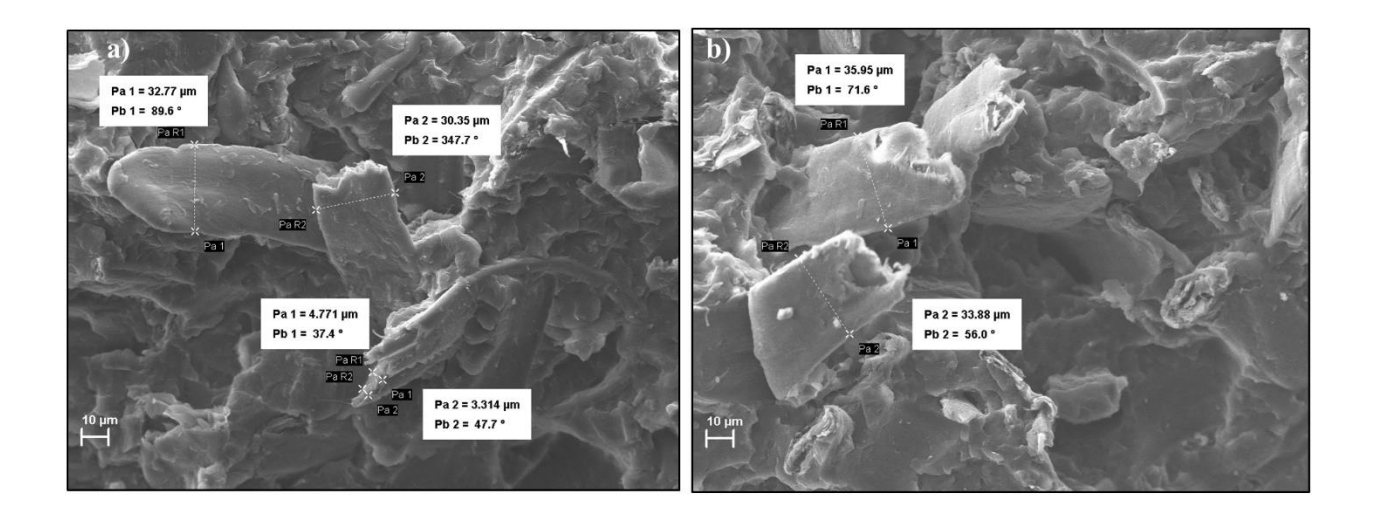


Figure 3.13: SEM micrographs of a) 30wt. % Cellulose A and b) 30wt. % Cellulose B.

Overall, the composites made with this process show good fiber distribution, confirming that the one step injection process with no compatibilizer successfully blended the hybrid materials in the PP. There is an advantage of using these pre-compounded pellets to speed up the process production.

3.4.3 Thermal properties

3.4.3.1 Thermal Gravimetric Analysis (TGA)

Figure 3.14 summarizes the thermal stability of the composites, where T_d is assigned as the temperature at the maximum rate of decomposition determined from the derivative thermogravimetric (DTG) curves. All composites are more stable than the neat PP and the T_d of the inorganic reinforced composites manifested the greatest increases. The incorporation of 30 wt. % cellulose also increased the thermal stability relative to PP but to a lesser degree. The inorganic

reinforcement/cellulose composites reinforced at 20/10, 15/15 and 10/20 (wt. %) have similar thermal stability.

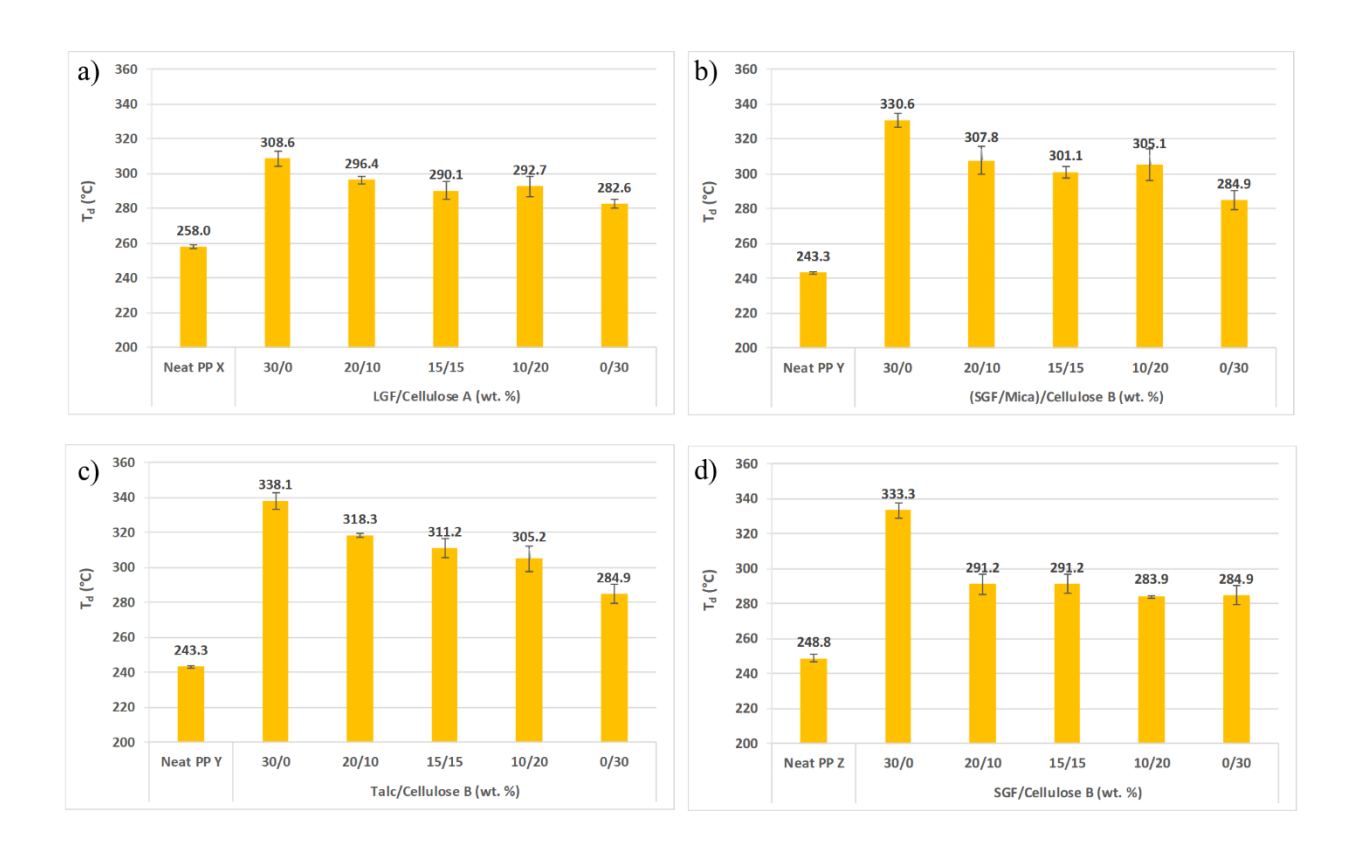


Figure 3.14: Temperature at the maximum rate of decomposition determined from DTG curves for a) LGF/Cellulose A, b) (SGF/Mica)/Cellulose B, c) Talc/Cellulose B and d) SGF/Cellulose B composites along with neat PP.

Thermal stability was also defined by the temperature at which 1% and 10% weight loss occurred, T_1 and T_{10} , respectively, as shown in Figure 3.15 and Figure 3.16. All hybrid composites are more thermally stable than the neat PP. The composites that contain cellulose possess lower T_1 and T_{10} compared to the composites with inorganic reinforcements only. However, this behavior is not observed for LGF/Cellulose A composites (Figure 3.15(a), Figure 3.16(a)).

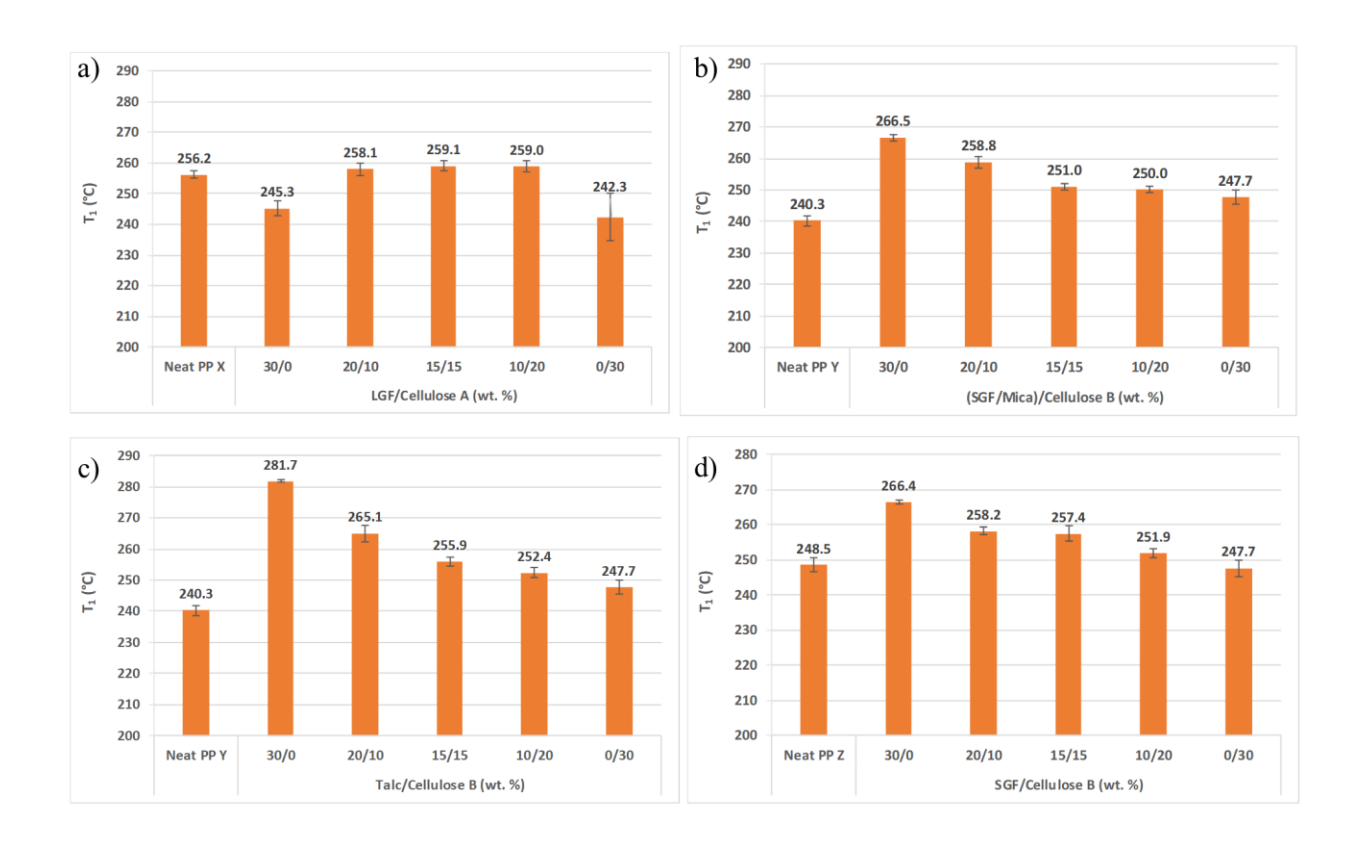


Figure 3.15: Temperature at 1% weight loss from TGA curves for a) LGF/Cellulose A, b) (SGF/Mica)/Cellulose B, c) Talc/Cellulose B and d) SGF/Cellulose B composites along with neat PP.

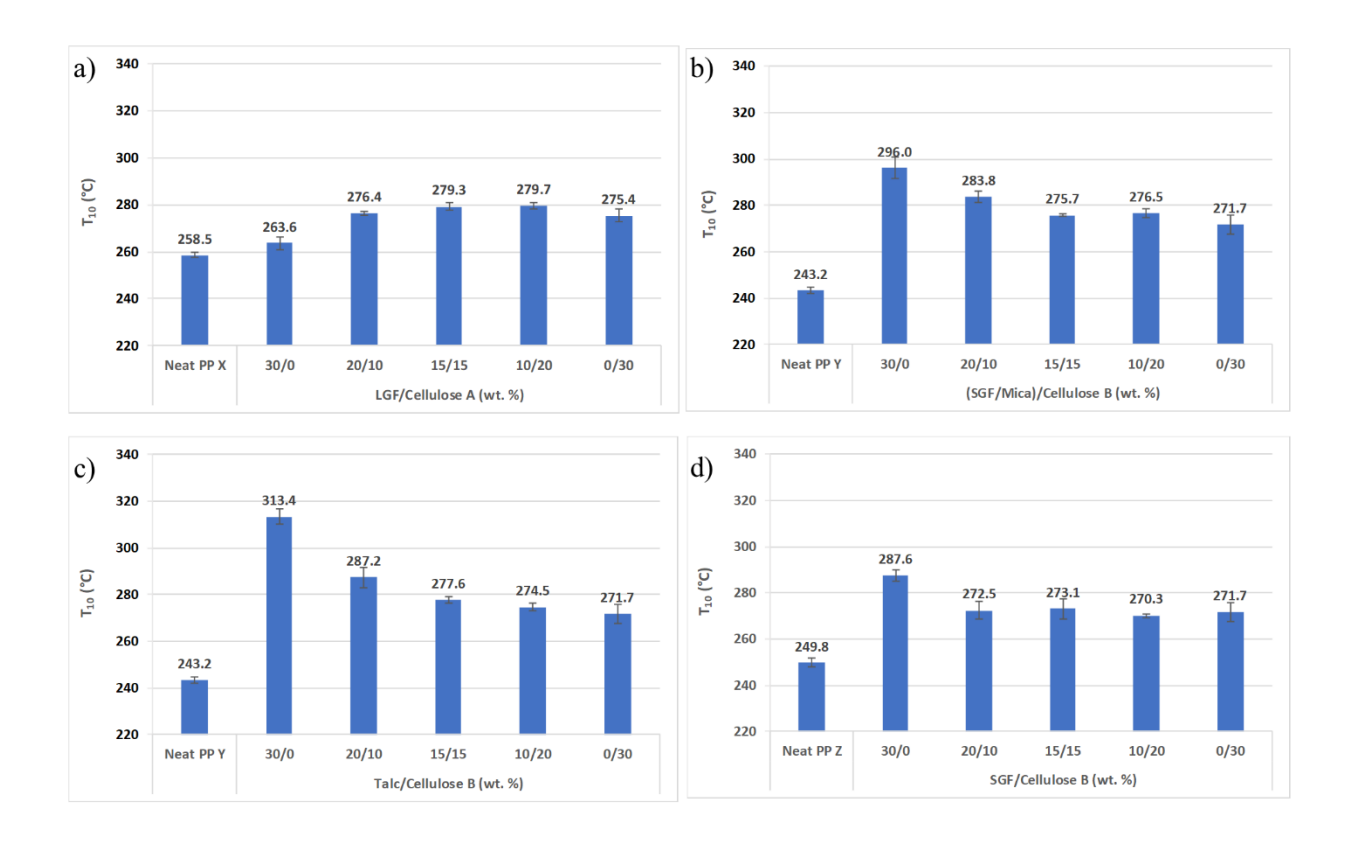


Figure 3.16: Temperature at 10% weight loss from TGA curves for a) LGF/Cellulose A, b) (SGF/Mica)/Cellulose B, c) Talc/Cellulose B and d) SGF/Cellulose B composites along with neat PP.

Figure 3.17 shows the residual weight percent at 587 °C. The residue decreased with cellulose content at this temperature and the residue is mainly from the inorganic reinforcements.

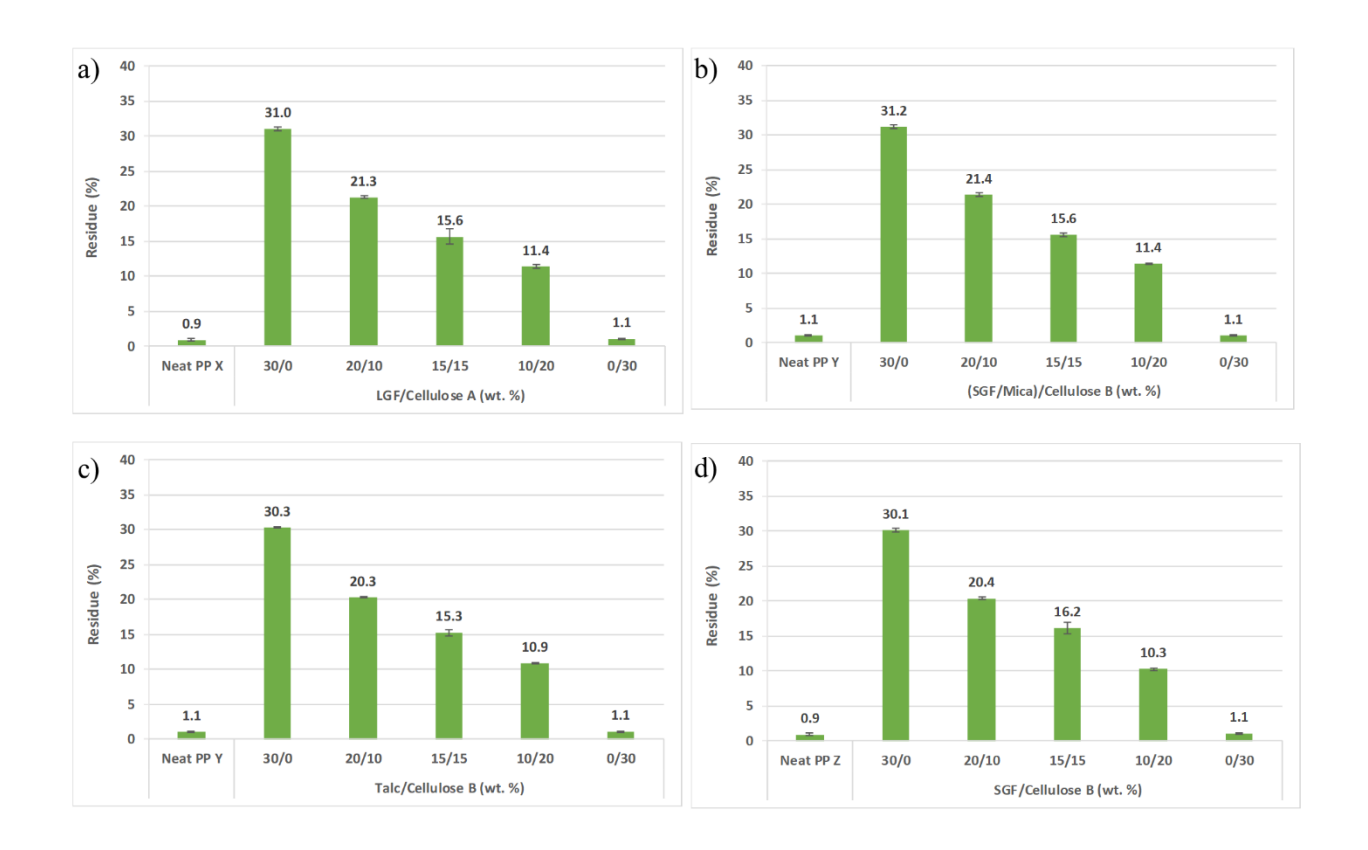


Figure 3.17: Residual weight percent at 587 °C from TGA curves for a) LGF/Cellulose A, b) (SGF/Mica)/Cellulose B, c) Talc/Cellulose B and d) SGF/Cellulose B composites along with neat PP.

These results indicate that hybrid composites made of cellulose can be to be considered for challenging conditions on under-the-hood applications.

3.4.3.2 Differential Scanning Calorimetry (DSC)

Figure 3.18 summarizes the T_c and T_m of PP and the composites. An increase in the T_c for all composites was detected compared to neat PP, which reveals that the fibers act as nucleating agents leading to a faster crystallization of PP matrix. This is a beneficial development which can increase the rate of part production. The DSC measurements indicate that the addition of cellulose had minimal effect on the melting temperatures.

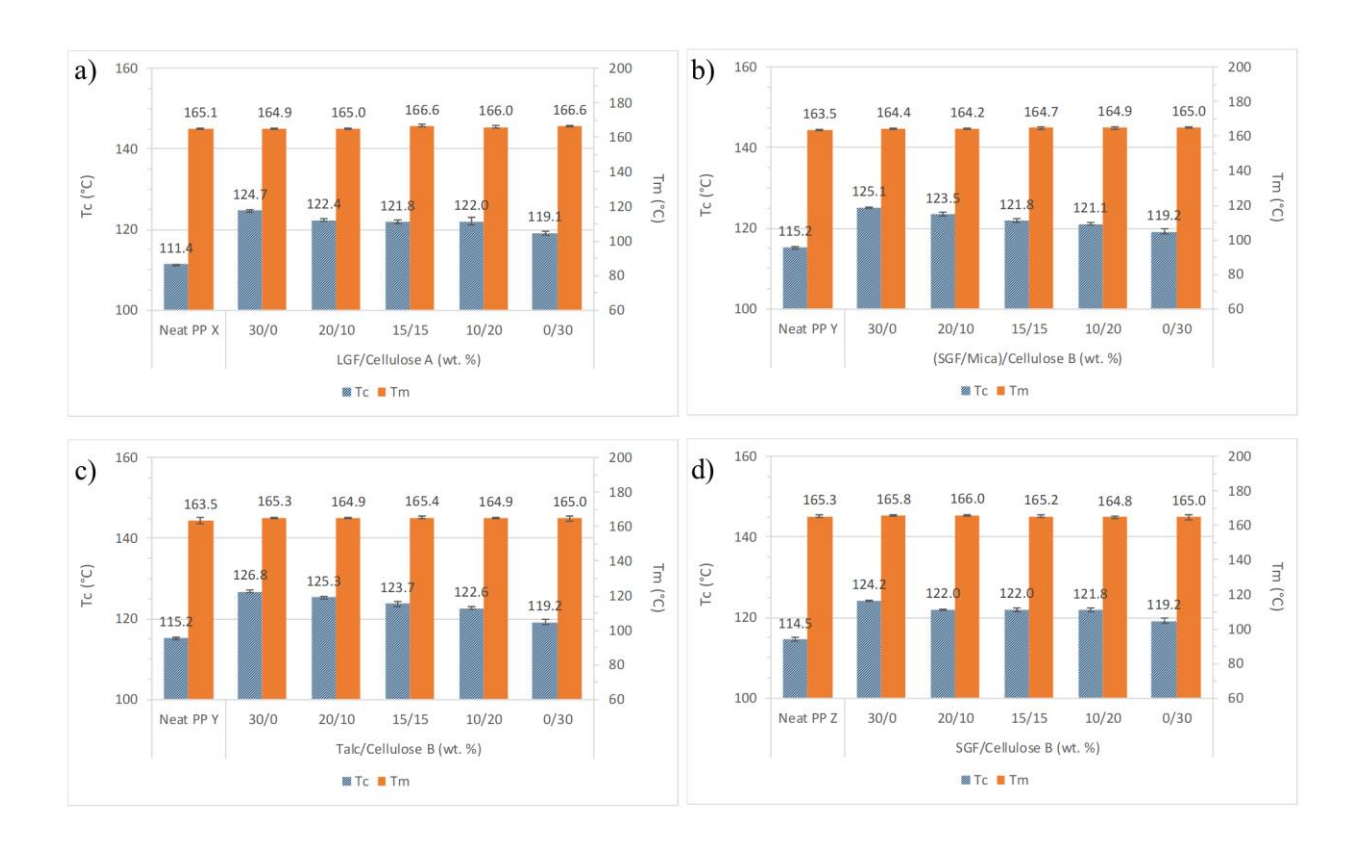


Figure 3.18: Crystallization and melting temperatures for a) LGF/Cellulose A, b) (SGF/Mica)/Cellulose B, c) Talc/Cellulose B and d) SGF/Cellulose B composites.

The ΔH_c and ΔH_m decreased with the incorporation of fibers (Table 3.3 and Table 3.4), with no significant dependence on fiber loading. This trend is in agreement with the results of

Huda *et al.* [15], where a reduction of the melting and crystallization enthalpies of the composites was observed with the addition of recycled newspaper cellulose fibers and talc compared to neat PP. Composites reinforced with 30 wt. % cellulose have, marginally, the lowest enthalpies. It may be that cellulose was hindering polymer chain movement during heat cycling, as observed by Langhorst *et al.* [8].

Table 3.3: Enthalpies of crystallization for neat PP and composites.

Composition	LGF/Cellulose A	(SGF/Mica)/Cellulose B	Talc/Cellulose B	SGF/Cellulose B
(wt. %)	$\Delta H_c (J/g)$	$\Delta H_c (J/g)$	$\Delta H_c (J/g)$	$\Delta H_c (J/g)$
Neat PP X	89.8 ± 3.3	-	-	-
Neat PP Y	-	96.7 ± 0.2	96.7 ± 0.2	-
Neat PP Z	-	-	-	104.6 ± 2.9
(30/0)	75.1 ± 0.6	67.8 ± 1.8	70.1 ± 1.4	73.6 ± 1.6
(20/10)	73.5 ± 1.5	68.7 ± 3.1	71.6 ± 1.7	69.4 ± 3.0
(15/15)	74.3 ± 3.8	69.2 ± 2.8	69.2 ± 2.7	70.6 ± 3.8
(10/20)	70.7 ± 3.2	66.9 ± 2.8	70.6 ± 0.7	73.3 ± 1.0
(0/30)	67.6 ± 3.3	62.3 ± 5.0	62.3 ± 5.0	62.3 ± 5.0

Table 3.4: Enthalpies of melting for neat PP and composites.

Composition	LGF/Cellulose A	(SGF/Mica)/Cellulose B	Talc/Cellulose B	SGF/Cellulose B
(wt. %)	$\Delta H_m (J/g)$	$\Delta H_m \ (J/g)$	$\Delta H_m (J/g)$	$\Delta H_m \; (J/g)$
Neat PP X	86.4 ± 3.6	-	-	-
Neat PP Y	-	95.8 ± 0.3	95.8 ± 0.3	-
Neat PP Z	-	-	-	104.0 ± 5.5
(30/0)	75.7 ± 1.6	67.3 ± 0.8	69.9 ± 1.5	72.0 ± 0.2
(20/10)	73.4 ± 3.4	67.8 ± 3.3	68.6 ± 0.3	67.9 ± 0.3
(15/15)	63.6 ± 6.7	66.8 ± 1.4	64.2 ± 2.6	71.3 ± 3.2
(10/20)	68.1 ± 3.1	68.0 ± 2.6	68.0 ± 1.4	71.6 ± 2.1
(0/30)	63.0 ± 0.6	62.5 ± 5.3	62.5 ± 5.3	62.5 ± 5.3

3.5 Conclusions

In this study, we investigated the hybridization of cellulose fiber with several inorganic fibers to reinforce a PP matrix for automotive applications. Composites were processed by injection molding with total reinforcement content kept at 30 wt. %. Overall, it was found that the composites made with hybrid fibers incorporating cellulose fibers acted as an effective reinforcement. Good improvements on the mechanical, thermal and morphological properties of the hybrid composites were observed.

Results from tensile, flexural and notched Izod impact tests show that in general the mechanical properties decreased with increasing cellulose content. However, composites with an optimum amount of cellulose fiber have sufficient properties which may reduce or replace a portion of the inorganic reinforcements in many applications. LGF/Cellulose A composites exhibited the best mechanical properties. However, when comparing thermal properties, (SGF/Mica)/Cellulose B, Talc/Cellulose B and SGF/Cellulose B composites exhibited similar or even superior properties. The T_c for all composites increased in comparison to neat PP, revealing the fibers ability to act as nucleating agents and speed part production.

Cellulose fiber polymer composite properties can be improved by the hybridization with inorganic reinforcements. The benefits of direct injection molding process include producing complex parts with high output rate, which increases profit margins. In addition, the adequate thermal stability achieved on the composites is important because it means their ability to withstand machinery temperatures and maintain their properties in conditions that would may cause thermal degradation. All these advantages have positive effect on manufacturability.

This work shows that hybridization of cellulose fiber with inorganic reinforcements in polypropylene composites has the potential to reduce the use of inorganic fibers in different automotive applications, leading to weight and cost savings, and contributing to sustainability of composites.

REFERENCES

REFERENCES

- [1] N. Saba, P. Tahir, M. Jawaid, A Review on Potentiality of Nano Filler/Natural Fiber Filled Polymer Hybrid Composites, Polymers (Basel). 6 (2014) 2247–2273. doi:10.3390/polym6082247.
- [2] M. Jawaid, H.P.S. Abdul Khalil, Cellulosic/synthetic fibre reinforced polymer hybrid composites: A review, Carbohydr. Polym. 86 (2011) 1–18. doi:10.1016/j.carbpol.2011.04.043.
- [3] E. Erbas Kiziltas, A. Kiziltas, E.C. Lee, Structure and properties of compatibilized recycled polypropylene/recycled polyamide 12 blends with cellulose fibers addition, Polym. Compos. 39 (2018) 3556–3563. doi:10.1002/pc.24376.
- [4] A. Kiziltas, E.C. Lee, Sustainable Composites Based on Polyamides and Cellulose Fibers, Dearborn, 2014.
- [5] A. Kiziltas, D.J. Gardner, Y. Han, H.-S. Yang, Mechanical Properties of Microcrystalline Cellulose (MCC) Filled Engineering Thermoplastic Composites, J. Polym. Environ. 22 (2014) 365–372. doi:10.1007/s10924-014-0676-5.
- [6] A. Birch, C. Dal Castel, A. Kiziltas, D. Mielewski, L. Simon, Development of cost effective and sustainable polyamide blends for automotive applications, in: 15th Annu. Soc. Plast. Eng. Automot. Compos. Conf. Exhib., Troy (Detroit), 2015.
- [7] J.H. Zhu, A. Kiziltas, E.C. Lee, D. Mielewski, Bio-based polyamides reinforced with cellulose nanofibers-processing and characterization, in: 15th Annu. Soc. Plast. Eng. Automot. Compos. Conf. Exhib., Troy (Detroit), 2015.
- [8] A. Langhorst, A. Kiziltas, D. Mielewski, E. Lee, Selective dispersion and compatibilizing effect of cellulose filler in recycled PA6/ PP blends, in: 15th Annu. Soc. Plast. Eng. Automot. Compos. Conf. Exhib., Troy (Detroit), 2015.
- [9] M.M. Thwe, K. Liao, Effects of environmental aging on the mechanical properties of bamboo–glass fiber reinforced polymer matrix hybrid composites, Compos. Part A Appl. Sci. Manuf. 33 (2002) 43–52. doi:10.1016/S1359-835X(01)00071-9.
- [10] M.M. Thwe, K. Liao, Durability of bamboo-glass fiber reinforced polymer matrix hybrid composites, Compos. Sci. Technol. 63 (2003) 375–387. doi:10.1016/S0266-3538(02)00225-7.
- [11] A. Arbelaiz, B. Fernández, G. Cantero, R. Llano-Ponte, A. Valea, I. Mondragon, Mechanical properties of flax fibre/polypropylene composites. Influence of fibre/matrix modification and glass fibre hybridization, Compos. Part A Appl. Sci. Manuf. 36 (2005) 1637–1644. doi:10.1016/j.compositesa.2005.03.021.

- [12] D. Romanzini, H.L. Ornaghi Junior, S.C. Amico, A.J. Zattera, Preparation and characterization of ramie-glass fiber reinforced polymer matrix hybrid composites, Mater. Res. 15 (2012) 415–420. doi:10.1590/S1516-14392012005000050.
- [13] K. Jarukumjorn, N. Suppakarn, Effect of glass fiber hybridization on properties of sisal fiber–polypropylene composites, Compos. Part B Eng. 40 (2009) 623–627. doi:10.1016/j.compositesb.2009.04.007.
- [14] S. Panthapulakkal, M. Sain, Injection-molded short hemp fiber/glass fiber-reinforced polypropylene hybrid composites—Mechanical, water absorption and thermal properties, J. Appl. Polym. Sci. 103 (2007) 2432–2441. doi:10.1002/app.25486.
- [15] M.S. Huda, L.T. Drzal, A.K. Mohanty, M. Misra, The effect of silane treated- and untreated-talc on the mechanical and physico-mechanical properties of poly(lactic acid)/newspaper fibers/talc hybrid composites, Compos. Part B Eng. 38 (2007) 367–379. doi:10.1016/j.compositesb.2006.06.010.

CHAPTER 4: FLEXIBLE ULTRAVIOLET SENSOR BASED ON CARBON NANOTUBES

This chapter is a result of an internship done by Mariana Desireé Reale Batista at NASA Ames Research Center during the NASA International Internship (NASA I²) program under the mentoring of Dr. Sun Jin Kim¹, Lawrence T. Drzal², Jin-Woo Han¹ and Meyya Meyyappan¹

¹Center for Nanotechnology, NASA Ames Research Center, Moffett Field, California, 94035, United States

²Department of Chemical Engineering and Materials Science, Michigan State University, East Lansing, Michigan, 48824, United States

This project was presented at the NASA Intern Poster Symposium (Dec 2018).

4.1 Abstract

Carbon Nanotubes (CNTs) were used to develop a sensor to detect Ultraviolet (UV) radiation, which is important for space communication, monitoring climate change and human exposure to UV light. Flexible substrates and paper electronics are attracting considerable attention since they offer new capabilities for devices that are not possible with the conventional rigid substrates. In this study, UV sensors were made not only on glass substrates but also on flexible substrates such as Polyimide Film (PI) and Cellulose Paper for comparison purposes. 'As received' CNTs in aqueous solution were diluted to final concentrations of 0.01 wt%, 0.004 wt%, 0.002 wt%, 0.001 wt% and 0.0005 wt% and drop-cast onto the active region between the electrodes of the sensor on each substrate. An optimum CNT concentration was identified and the dispersion and topographies of the nanoparticles on the sensor substrates were investigated by Scanning

Electron Microscopy (SEM) and Atomic Force Microscopy (AFM). All the sensors respond immediately to UV On/Off cycles with a change in resistance due to the ability of the CNTs to adsorb and desorb oxygen on their surface. Results show that sensors with the lowest concentration of CNTs (0.0005 wt%) exhibit the best response. The PI substrate yields the sensor with the highest response at 71% after 21 min of On/Off cycle, while glass and cellulose paper substrates exhibit response at 48% and 39%, respectively. After mechanically bending the flexible sensors at a curvature radius of 10 mm for 1000 times their functionality is maintained, which is an advantage for practical applications. Therefore, the PI sensor was selected for wearable applications using a simple printing technique in which electrodes were printed on the PI substrate and could be tailored for wristband or sunglass use. Outdoor testing under natural sunlight shows that the sensor accurately detects UV radiation and could be further developed for potential commercial applications.

Keywords: Ultraviolet Sensor; Flexible Sensor; Ultraviolet Radiation; Carbon Nanotubes;

4.2 Introduction

Ultraviolet (UV) radiation consists of photons with wavelengths ranging from 10 nm to 400 nm. Most of the UV light from the sun is absorbed by the ozone layer, however photons with wavelengths longer than 280 nm can reach the earth [1] and the intense exposure to this radiation can cause damage to human skin, especially cancer. Therefore, it is important to develop sensors capable of detecting this type of radiation which will help in the prevention of health problems related to this exposure. UV sensors are also widely used in many other applications, including space communication and measurement of UV for climate change studies.

Many UV sensors and materials for sensing UV radiation have been reported [1,2]. Although the traditional Si based photodetectors are commonly used, they exhibit some limitations with respect to UV detection, such as the use of costly and complex filters, and degraded performance with temperature [1,3]. These limitations are overcome with the wide bandgap semiconductors such as AlN, InN, GaN, diamond, and SiC based UV detectors that have not only high selectivity and response speed but also the ability to operate in harsh and high temperature conditions [1].

More recently, one-dimensional nanostructured semiconductors such as Ga₂O₃ nanowires, GaN nanowires, ZnO nanowires or other metal-oxide nanostructures have attracted attention for use as UV detectors due to their wide bandgap and improved photosensitivity [1]. However there are some challenges integrating the nanostructures into UV photodetectors [3] and the high cost related to the low photo response current from the small size of the nanowires as reported by Bai *et al.* [4].

Although those sensors exhibit high performance, they exhibit some limitations and more work is needed for investigating their use on flexible substrate for targeting bending and wearable applications.

Flexible substrates and paper electronics are attracting attention since they offer new possibilities that are not attainable with conventional rigid substrates [5]. They have applicability in displays, detectors, memory and energy storage devices. Cellulose paper [6,7] as well as cotton textile [8] has been used as flexible substrates to fabricate gas and vapor sensors and there is an increasing demand for the development of new sensors that can bend.

Carbon nanotubes (CNTs) consist of one or several graphene planes rolled in a cylindrical shape with diameters of 1 to several dozens of nanometers and lengths of up to several microns [9]. They have been reported as excellent sensor material for gas, vapor and UV sensors [9,10] due to their large specific surface area, high electrical conductivity and solution processability [11,12]. CNTs also exhibit good mechanical properties with a high degree of flexibility that are critical for bendable and stretchable substrates [2,5].

In this work, carbon nanotubes were used as the sensing material to detect UV light. Detection occurs since the radiation affects their resistance as a result of oxygen adsorption and desorption mechanisms on their surface [13,14]. An optimum CNT concentration was identified, and device fabrication, testing and evaluation were completed. UV sensors were fabricated on flexible substrates such as PI film and Cellulose Paper, and rigid glass substrate for comparison purposes. PI was selected since it withstands high temperature applications (around 400 °C), which is important for space mission exploration. Cellulose paper was chosen since it is a low cost, lightweight, ecofriendly and disposable material, leading to an approach for the development of smart papers.

4.3 Experimental section

4.3.1 Materials

As received single walled CNTs (semiconducting and metallic, diameter = $1.0 \sim 1.3$ nm, length = $5 \sim 50$ µm) in aqueous solution (0.1 wt%) from KH Chemicals were further diluted with DI water to final concentrations of 0.01 wt%, 0.004 wt%, 0.002 wt%, 0.001 wt% and 0.0005 wt%. Vortex mixing and sonication were applied to the solutions to avoid CNT agglomeration, which could reduce the overall surface area and therefore impact the sensor sensitivity [12]. The solution

was drop-cast onto the active region between the electrodes (Figure 4.1) and the sensors were allowed to dry overnight at room temperature. The electrodes were made of silver (Ag) conductive epoxy adhesive (M.G. Chemicals) and the distance between electrodes was 3.5 mm. Substrates were: glass slide, PI film and cellulose paper. Initial resistance of the fabricated sensors with 0.0005 wt% CNT was between 1 and 3 k Ω .

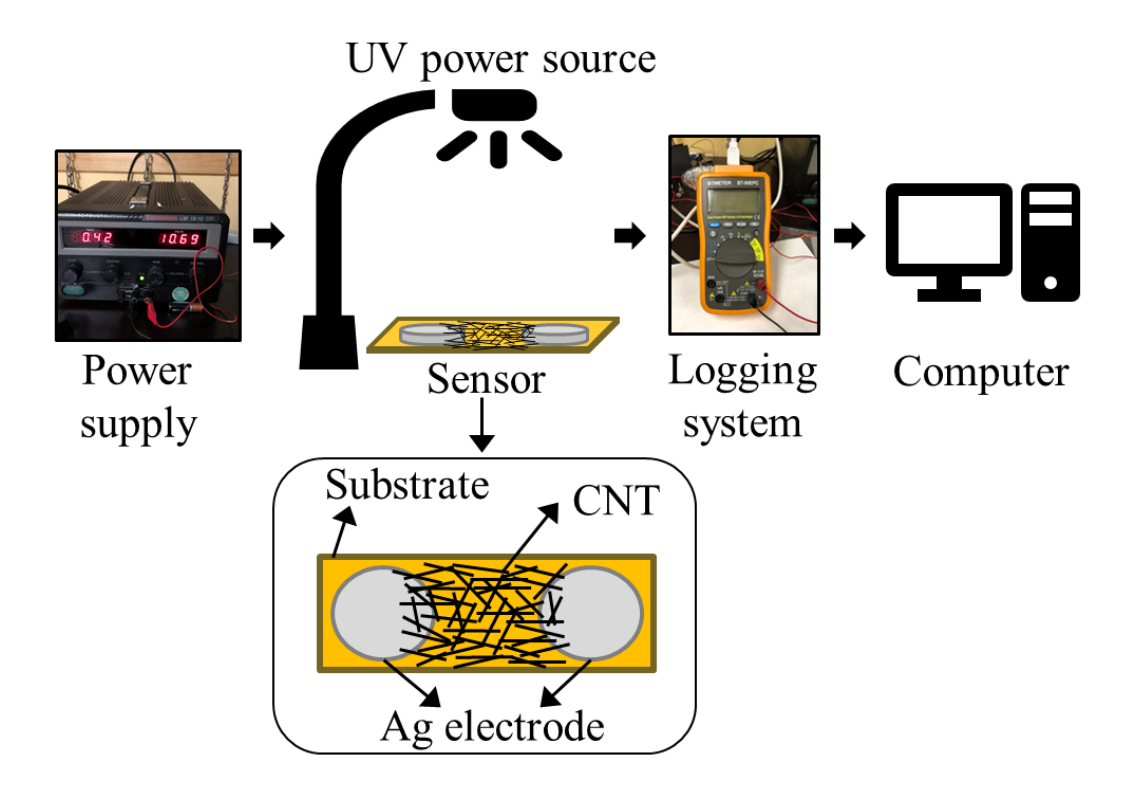


Figure 4.1: Sensor structure and test set up.

4.3.2 Methods

The CNT coated sensor substrates were characterized by SEM on a Carl Zeiss Auriga FIB microscope and topographies were measured by Cypher AFM. The silicon AFM probe has resonant frequency 300 kHz, force constant 40 N/m and operated in tapping mode.

The sensors were exposed to a UV light source with 365 nm wavelength (CHANZON, 11V) mounted on a bench and the resistances were collected every second by a real time monitoring system using a multimeter logging system (BTMETER BT-90EPC), as shown on Figure 4.1. The sensor response was calculated according to Equation 1 as the ratio of resistance shift over the initial resistance:

$$Response = \frac{(R_f - R_i)}{R_i} \tag{1}$$

where R_f and R_i are the resistance upon UV exposure and initial resistance, respectively [2].

The sensor response with variable UV light power density was investigated from 0.5 to 2.5 mW/cm² by changing the distance to the sensor and the calibration was done by a commercial optical power meter (Optical Associates Inc. 306).

4.4 Results and discussion

4.4.1 CNT distribution on sensor substrate

The micrographs of CNT coated substrates are shown in Figure 4.2. The PI (Figure 4.2(a)) and glass (Figure 4.2(b)) illustrate that the nanoparticles uniformly covered the surfaces forming an interconnected network structure that provides a continuous pathway for carrier mobility. For the cellulose paper (Figure 4.2(c)), the distribution of CNTs is not as clear on the paper surface due to its hydrophilicity and surface roughness related to the cellulose fiber arrangement. During the drop-casting process CNTs may have experienced a capillarity force causing concentration into the regions between cellulose fibers [11] and therefore they may not be totally exposed at the surface. Additionally, some CNT network disruption can be noted on the higher magnification macrograph on Figure 4.2(c) that may reduce the carrier mobility. The adhesion of CNT on paper

is due to hydrogen bonding between surface carboxyl and hydroxyl groups of the CNT with hydroxyl groups on cellulose [7,8].

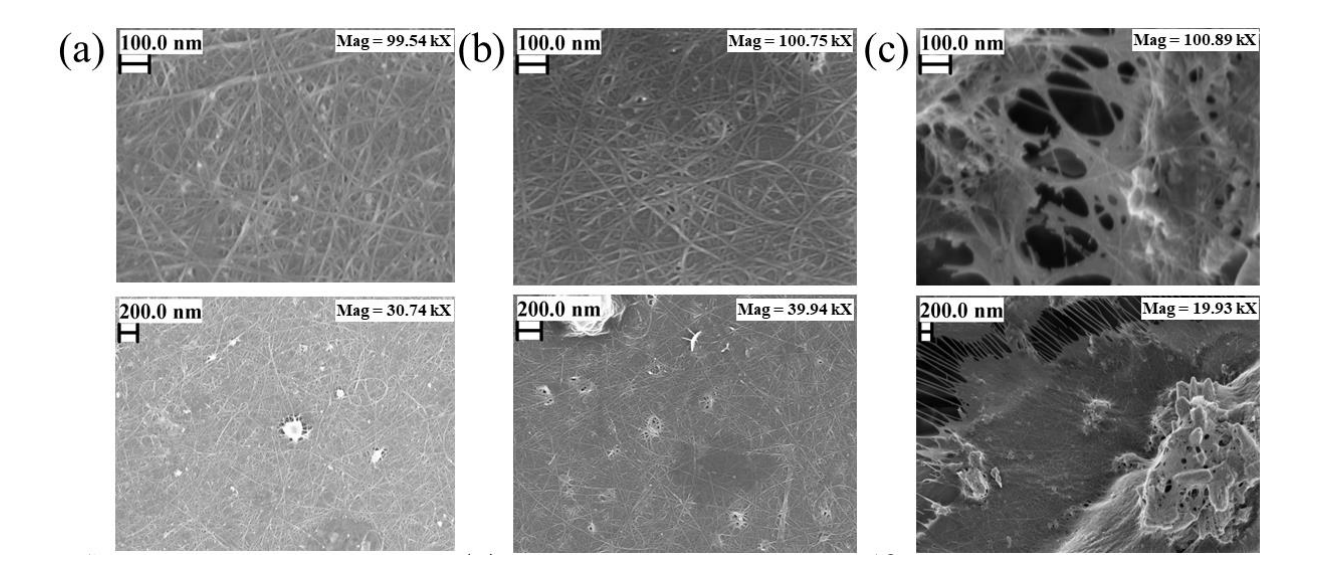


Figure 4.2: SEM micrographs of CNT coated a) PI, b) glass and c) cellulose paper substrate at higher (top) and lower (bottom) magnification.

The AFM observations support the SEM results. The topographies of CNT coated substrates obtained by AFM are shown on Figure 4.3 (5 μ m x 5 μ m area) and Figure 4.4 (1 μ m x 1 μ m area). The presence of CNT on the surface of PI is clearly shown. Other artifacts can also be noticed on the surface. The main difference observed is that overall the cellulose substrate has higher surface roughness (inherent of the paper making process) than the PI or the glass as summarized on Table 4.1 . Due to capillarity forces and surface topographical differences between the macro cellulose fiber and the nanotubes, it will not form a uniform homogeneous distribution of the CNTs on the cellulose surface compared to the PI and glass samples resulting in lower sensor

sensitivity. Glass surface also exhibits artifacts on the surface and a roughness that introduces difficulties in the characterization of the CNT surface using the tapping mode of the AFM.

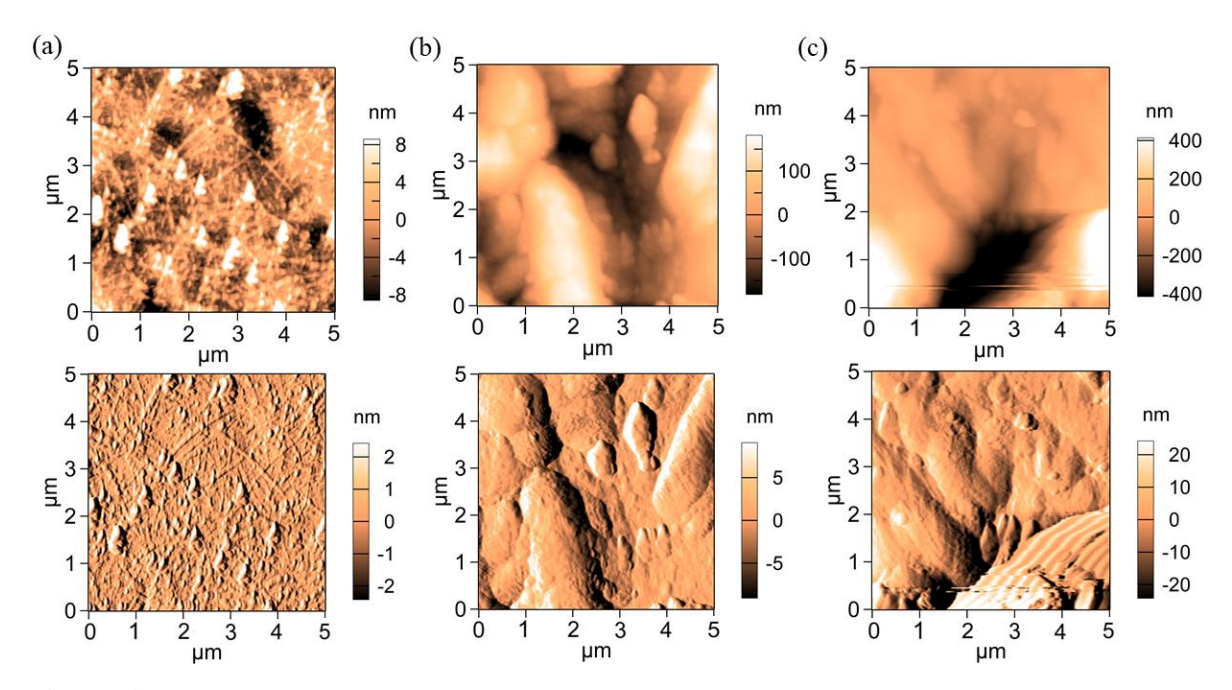


Figure 4.3: Height (top) and amplitude (bottom) profile of CNT coated a) PI, b) glass and c) cellulose paper substrate by AFM on a 5 μ m x 5 μ m area.

Table 4.1: Roughness of CNT coated substrates by AFM (nm) on a 5 µm x 5 µm area.

	PI	Glass	Cellulose paper
Average Deviation	4.4 ± 1.7	46.0 ± 32.7	112.7 ± 31.4

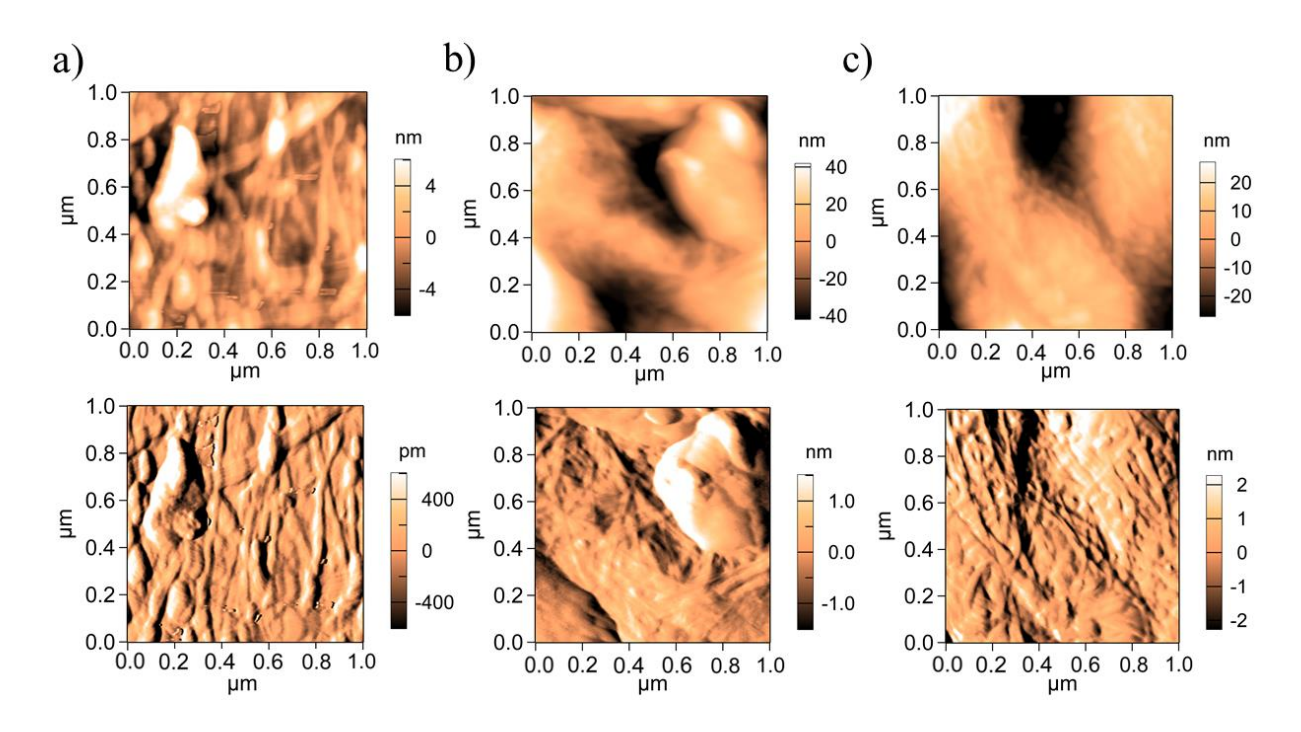


Figure 4.4: Height (top) and amplitude (bottom) profile of CNT coated a) PI, b) glass and c) cellulose paper substrate by AFM on a 1 μm x 1 μm area.

Table 4.2: Roughness of CNT coated substrates by AFM (nm) on a 1 μ m x 1 μ m area.

	PI	Glass	Cellulose paper
Average Deviation	2.3 ± 0.9	20.7 ± 24.2	19.0 ± 11.7

4.4.2 Sensor response to UV light

Figure 4.5 and Figure 4.6 show the response of the sensors calculated according to Equation 1 for all substrates with 0.0005 wt% CNT when exposed to On/Off cycles of UV light with 2.5 mW/cm². In Figure 4.5 the UV light was initially off for 1 min, then turned on for 2 min and finally turned off for 10 min in order to check the recovery. All the samples respond

immediately when the light is turned on with an increase in their resistance. Under UV illumination, the O_2 molecules that normally adsorb on the sidewall of the CNTs, are desorbed from the surface of the nanotubes reducing the hole concentration [13]. Since the CNT has a p-type semiconducting behavior [12] a reduction of hole concentration will increase the resistance, and vice versa. In this cycle the sensors exhibited a maximum response of 38%, 26% and 20% for PI, glass and cellulose paper, respectively.

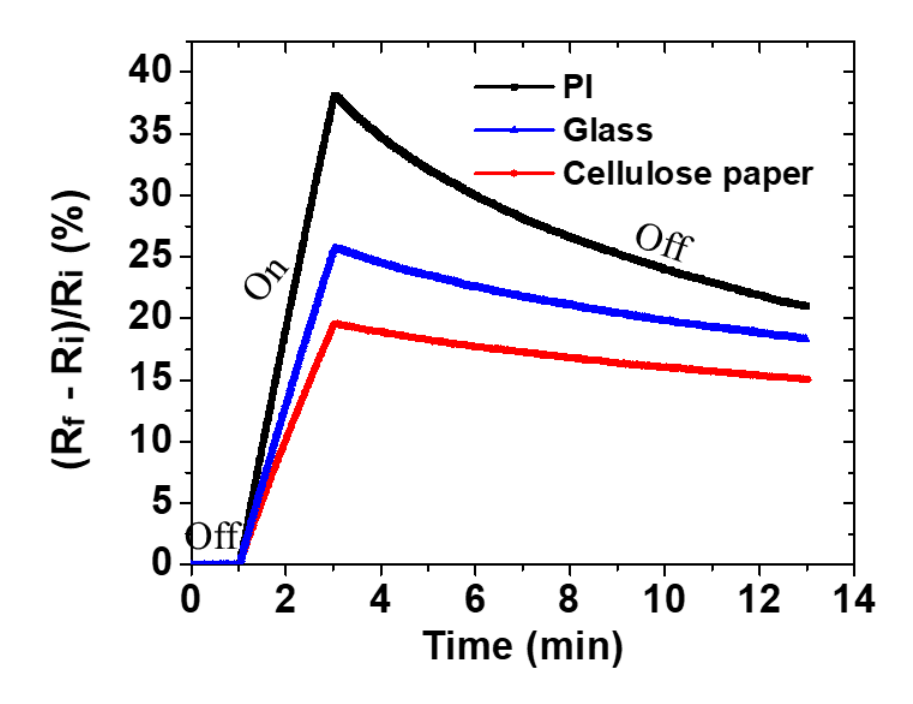


Figure 4.5: Response of sensors under UV illumination.

As soon as the light is turned off the adsorption of O_2 molecules onto the CNT surface begins, increasing the hole concentration and leading to a gradual baseline recovery. As noted in Figure 4.5, the recovery is slower than the sensor response, since the O_2 adsorption is a natural passive process and the O_2 desorption is induced by UV light [13]. Another drawback is that sensors can also exhibit incomplete recovery to the baseline since other types of molecules in the

air may occupy the oxygen sites [13]. To overcome this drawback of slow and incomplete recovery, in previous work Kim et al. [13] proposed a UV sensor encapsulated with a polymer membrane, capable of inhibiting gas exchange between the sensor and the external environment. This strategy yielded a sensor with fast and full recovery to the baseline, due to the constant O₂ trapped in the sensor.

Figure 4.6 show the response of the sensors for a sequence starting with 1 min without UV illumination, then 5 cycles of turning the UV light for 1 min followed by 3 min of UV Off.

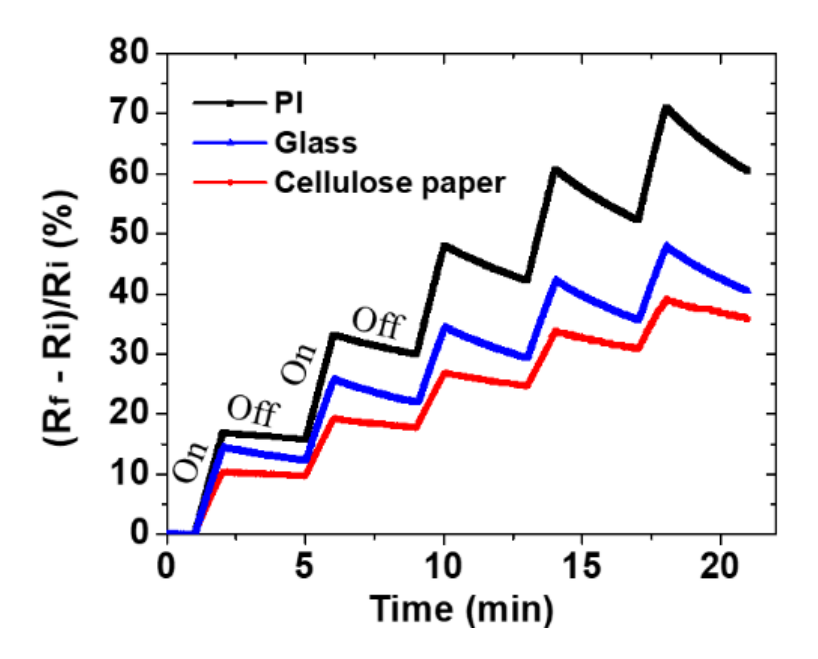


Figure 4.6: Resistance change of sensors under UV On/Off cycling.

As illustrated by Figure 4.6, the PI film yields the sensor with the best response (71% after 21 min of On/Off cycle), while glass and cellulose paper substrates have lower response at 48% and 39%, respectively. One reason for the high sensitivity on PI is due to the uniform distribution

of CNTs on the PI surface. Therefore, the largest surface area of CNTs were exposed and available at the top of the substrate to UV detection mechanism.

On the cellulose paper, during sensor preparation the evaporation of CNT aqueous solution was not uniform with areas in the 'valleys' of the paper evaporating much slower than the higher asperities. This would have the effect of concentrating the CNTs in those areas, making a more non-uniform CNT network. CNTs in the regions between cellulose fibers may not be totally exposed and available to participate in the mechanism of UV light detection, resulting in lower sensor sensitivity. Previous work [7] shows that a gas sensor with CNTs lying directly on paper surface has higher sensitivity than a sensor that was made by mixing and filtering CNT with dissolved paper since a fraction of the nanotubes will be inside the cellulose matrix, leading to a smaller active surface area of the CNT.

The results show that all the CNT based sensors regardless of the substrate type are capable of effectively detecting UV light. It is worth mentioning that after the recovery occurred these sensors were tested repeatedly without loss of function.

Because of the better performance, the PI substrate was chosen for further analysis and an optimum CNT concentration was investigated. As shown in Figure 4.7 after 2 min of UV illumination, sensors with the lowest concentration of 0.0005 wt% CNT exhibit the best response of 38% while the sample with the highest concentration of 0.01 wt% CNT has the lowest response of 0.4%. The sensors with 0.001wt%, 0.002 wt% and 0.004 wt% CNT show a response of 26%, 14% and 9%, respectively. Since the photons are mostly absorbed at the exposed CNT surface, the samples that contain a greater concentration of CNTs will have a lower resistance change due to a 'shadowing' effect for the thicker films where the CNTs below the surface do not participate in

the O_2 adsorption as well those on the surface. This investigation was repeated with the cellulose paper sensors and the same trend was observed. Therefore, the sensors with the lowest concentration of 0.0005 wt% CNT were chosen for further analysis.

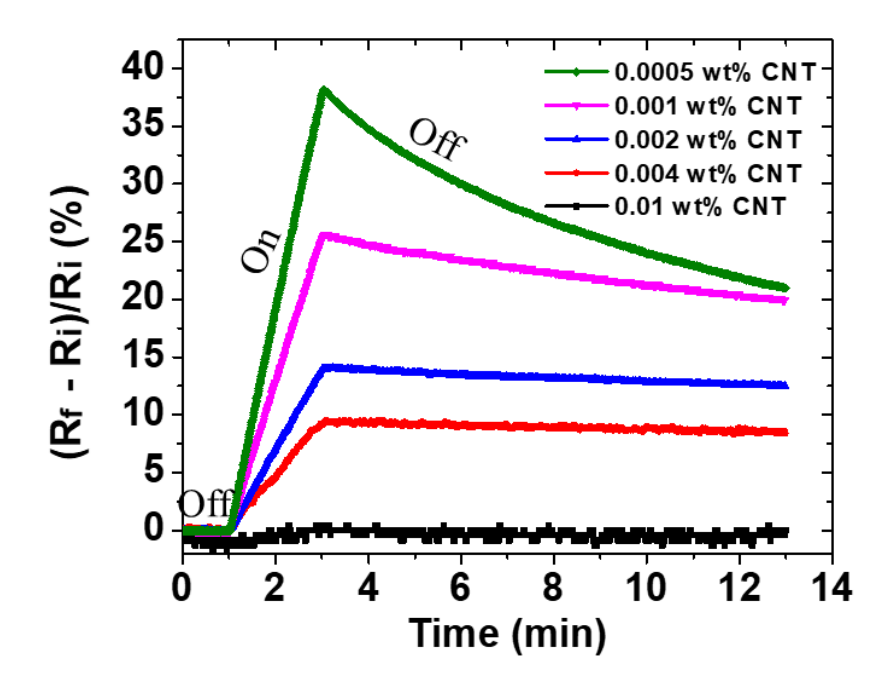


Figure 4.7: Response under UV illumination as a function of CNT weight percent on PI substrate.

Figure 4.8 shows the response measured for PI sensors under different UV power density, with 0.0005 wt% CNT. For 0.5, 1.0, 1.5, 2.0 and 2.5 mW/cm² the maximum response after 21 min of UV On/Off cycle was 13%, 25%, 40%, 46% and 71%, respectively. As noted in previous work [2], the response of CNT based UV sensor is proportional to the photon flux, so greater changes in the resistance occur with higher UV light intensity. Even the lowest density power tested on the sample was capable to quantify the effects of UV light, which implies that even in a day that the sun light is not intense the sensor is able to detect the UV radiation, showing the potential for applications requiring UV detection.

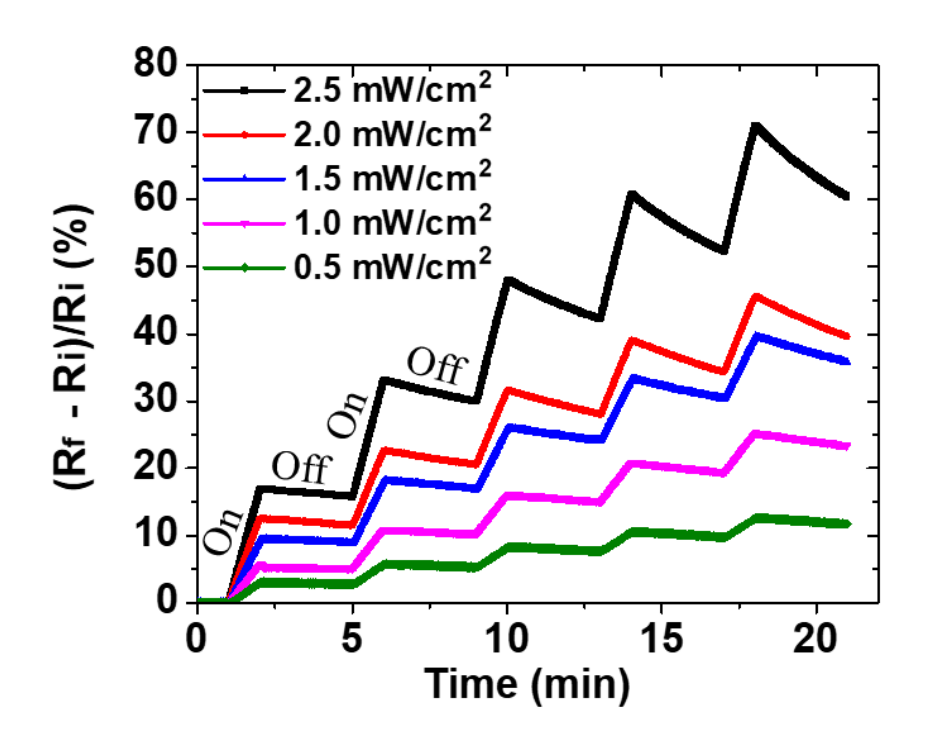


Figure 4.8: Resistance change as a function of power density under On/Off cycle for PI substrate.

4.4.3 Sensor mechanical robustness

The advantage of the present sensors consists on their flexibility and it is essential that they maintain their functionality when deformed from their planar configuration by bending. Assessment of the sensor robustness was conducted by mechanically bending the sensors (Figure 4.9) from flat to a 7.5 mm radius of curvature and measuring the change in their resistance. As summarized on Table 4.3, a maximum change of 4.1% and 4.9% in resistance for the sensors on the PI and cellulose paper substrates, respectively, was observed at the minimum radius of 7.5 mm. After this observation, a conditioning step was carried out by repeatedly bending the sensor up to 1000 times to a radius of curvature of 10 mm to ensure that the sensors reach a stable value of resistance prior to testing their response under UV light.

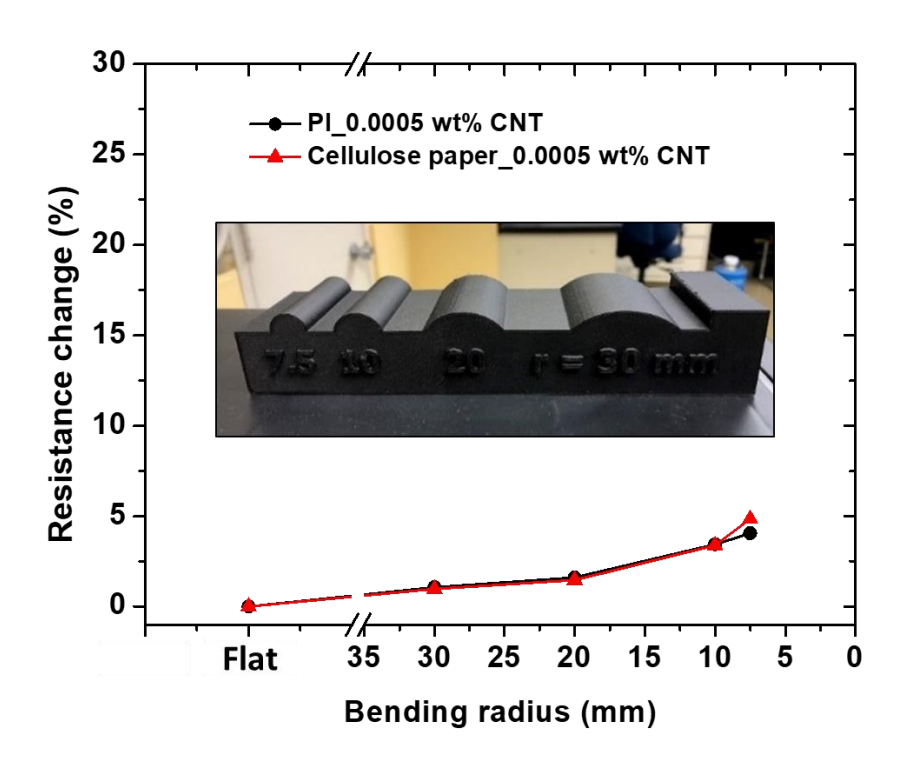


Figure 4.9: Mechanical bending test with varying radius of curvature.

Table 4.3: Resistance change (%) of sensors for varying radius of curvature.

Radius (mm)	PI	Cellulose paper
	Resistance Change	Resistance Change
Flat	0.0	0.0
30	1.1	1.0
20	1.6	1.5
10	3.4	3.4
7.5	4.1	4.9

Figure 4.10 shows that the resistance change increased at the beginning of the test and then was stabilized at 1.5% and 1.2% change for PI and cellulose paper sensor, respectively. After this conditioning step the sensors exhibited a stable internal resistance and were tested under UV light.

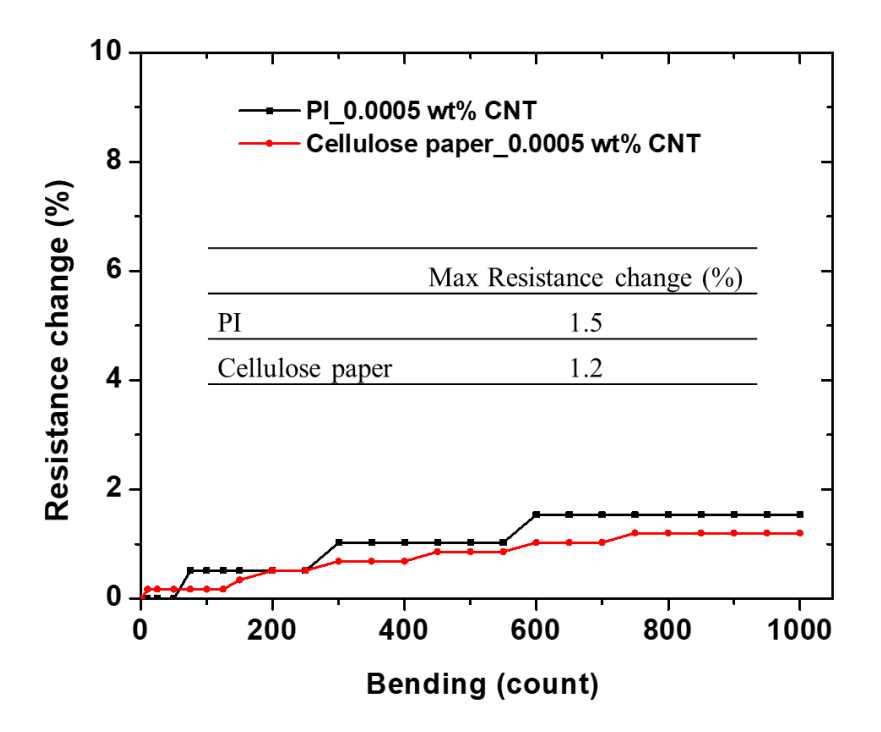


Figure 4.10: Bending cycle test at a curvature radius of 10 mm (conditioning step).

Figure 4.11 shows the UV response of the conditioned sensors under the flat condition and bent with a radius of curvature of 10 mm. As can be clearly noted for PI and cellulose paper sensors the response for both states are nearly the same. The results shown on Figure 4.11 indicate that the sensors can operate without losing their functionality even when mechanically bent 1000 times, and emphasize the flexibility of the sensor and possible suitability for wearable applications.

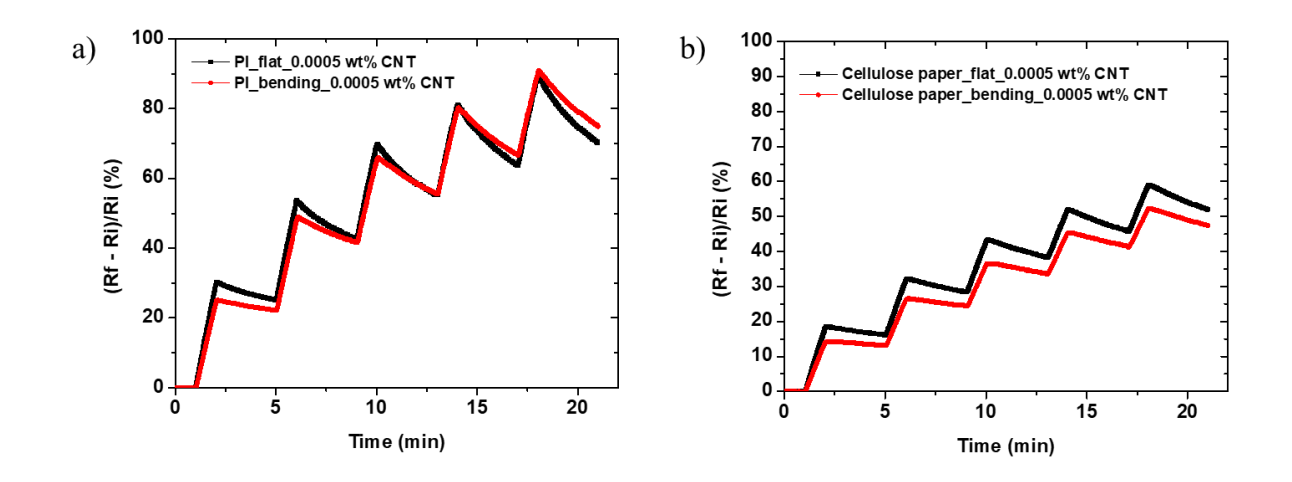


Figure 4.11: UV response of the conditioned a) PI and b) cellulose paper sensors under flat and 10 mm bending state.

4.4.4 Sensor response under natural sunlight

In order to develop functional sensors for general applications, it is essential to evaluate performance under outdoor UV light. The present PI sensor was adapted for wearable applications and tailored for wristband and sunglasses uses, and then tested under natural sunlight. Using a commercially available printer (Voltera V-one), conductive silver ink-based electrodes were printed on the PI substrate (Figure 4.12), and subsequently, 0.0005 wt% CNT solution was drop-casted onto the active region between the electrodes.

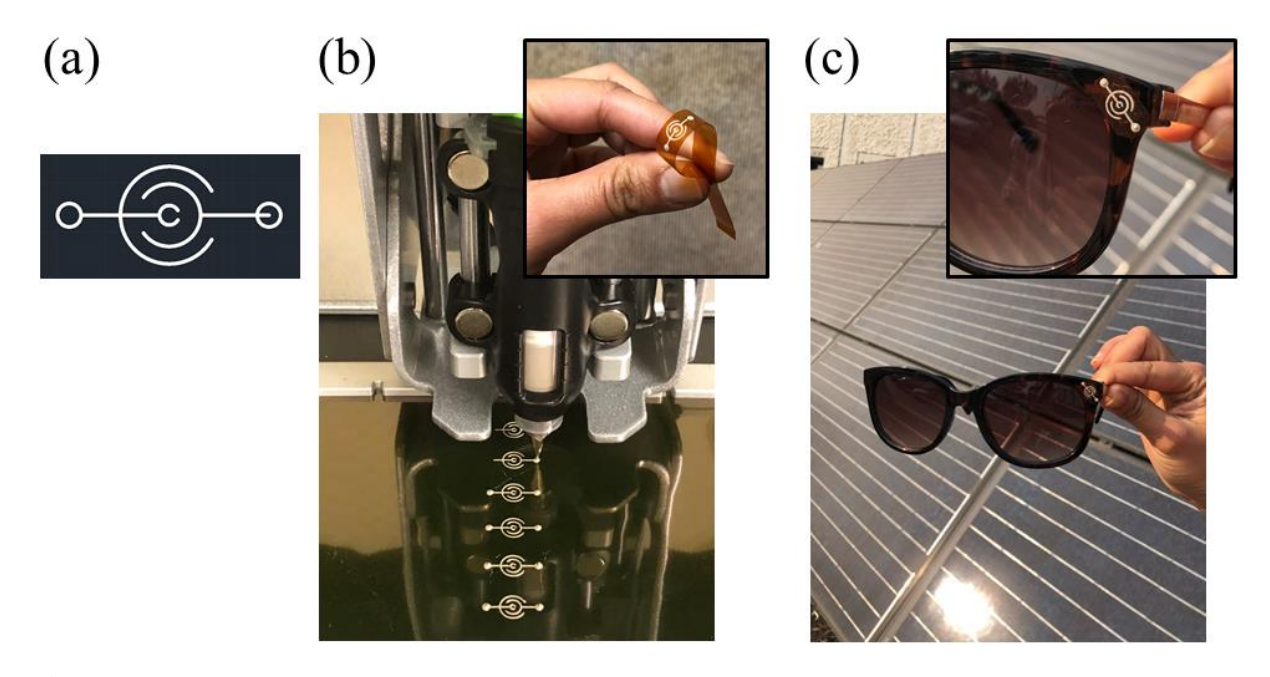


Figure 4.12: a) Design of electrodes and b) printing on PI substrate for c) potential application on sunglasses and wristband.

The sensors were tested outdoors in Mountain View, California, with a sunlight power density measured at 2.2 mW/cm². The sensors were covered with a filter that blocked UV light for 1 min and then they were exposed to the sunlight for 1 min, during 5 cycles. The results are summarized in Figure 4.13 and show that the sensors immediately respond to the UV On/Off cycle and clearly reproduce the results obtained in the laboratory. Results under natural sunlight are consistent with laboratory measurements indicating that these sensors have the potential to be mass produced using this simple printing technique.

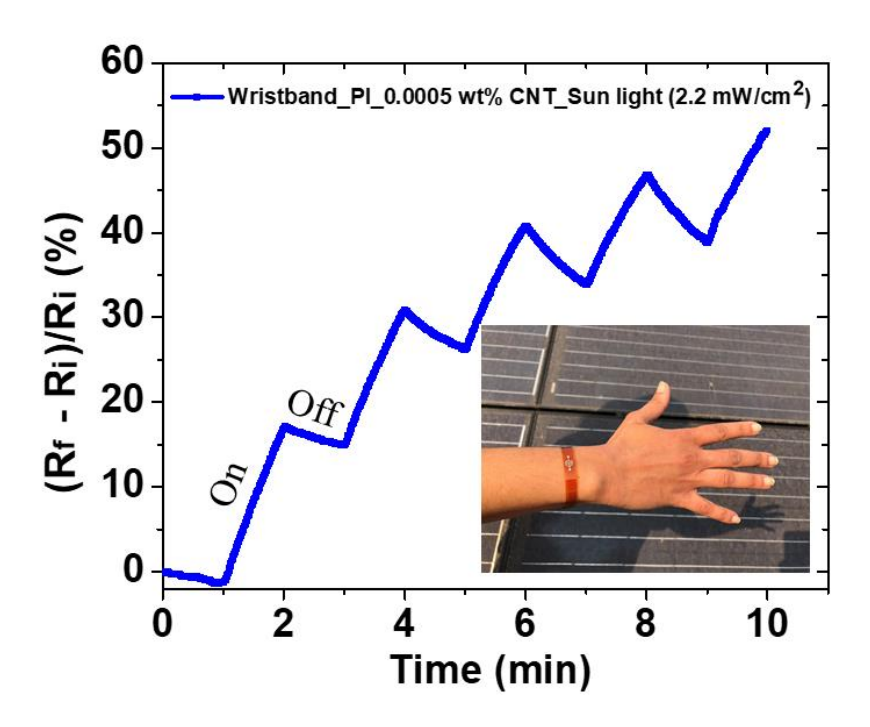


Figure 4.13: Resistance change of UV sensor on wristband under sunlight.

4.5 Conclusions

The results reported here show that CNTs are an excellent candidate for UV sensor development on flexible substrates. An optimum CNT concentration was identified, material characterization was performed and device fabrication, testing and evaluation were investigated. All samples respond to UV On/Off cycles and after the recovery, the sensors were tested repeatedly without loss of function. The PI substrate yields the best response at 71% after 21 min of On/Off cycle exposure. Cellulose paper exhibited a response of 39% but it is still effective and is an approach for the development of smart papers taking advantage of its low cost, lightweight, ecofriendly and disposable characteristics. Additional research may also lead to improvements in recovery time.

Bending tests conducted under a varying radius of curvature showing that sensors can operate without losing functionality even when mechanically cycled 1000 times. Sensors work effectively even when exposed to a low density power of 0.5 mW/cm². Response to UV radiation was measured under natural sunlight, and results are consistent with laboratory measurements, which demonstrates the potential of the sensors for wearable applications such as wristband and sunglasses. This work identifies a simple process to print electrodes on PI film (or cellulose paper) that can potentially be scaled-up for targeting high temperature applications for space mission exploration as well as for earth based exposure to UV light.

4.6 Acknowledgements

We thank the NASA International Internship (NASA I²) program, specially Porsche Parker, and the support of NASA Nanotechnology group specially Dongil Lee, Dong-Il Moon, Myeong-Lok Seol and Beomseok Kim. We want to acknowledge Michigan State University, especially Per Askeland for the SEM measurements at the Composite Materials and Structures Center, and Eric Goodwin and Reza Loloee for the AFM measurements at the Department of Physics and Astronomy. I also thank my sponsors Coordenação de Aperfeiçoamento de Pessoal de Nível Superior (CAPES) through the Brazil Scientific Mobility Program [99999.013655/2013-02] and Agência Espacial Brasileira (AEB).

REFERENCES

REFERENCES

- [1] L. Sang, M. Liao, M. Sumiya, A comprehensive review of semiconductor ultraviolet photodetectors: From thin film to one-dimensional nanostructures, Sensors (Switzerland). (2013). doi:10.3390/s130810482.
- [2] S.J. Kim, D.-I. Moon, M.-L. Seol, B. Kim, J.-W. Han, M. Meyyappan, Wearable UV Sensor Based on Carbon Nanotube-Coated Cotton Thread, ACS Appl. Mater. Interfaces. 10 (2018) 40198–40202. doi:10.1021/acsami.8b16153.
- [3] D. Gedamu, I. Paulowicz, S. Kaps, O. Lupan, S. Wille, G. Haidarschin, Y.K. Mishra, R. Adelung, Rapid fabrication technique for interpenetrated ZnO nanotetrapod networks for fast UV sensors, Adv. Mater. (2014). doi:10.1002/adma.201304363.
- [4] S. Bai, W. Wu, Y. Qin, N. Cui, D.J. Bayerl, X. Wang, High-performance integrated ZnO nanowire UV sensors on rigid and flexible substrates, Adv. Funct. Mater. (2011). doi:10.1002/adfm.201101319.
- [5] T. Takahashi, K. Takei, A.G. Gillies, R.S. Fearing, A. Javey, Carbon nanotube active-matrix backplanes for conformal electronics and sensors, Nano Lett. (2011). doi:10.1021/nl203117h.
- [6] S. Ammu, V. Dua, S.R. Agnihotra, S.P. Surwade, A. Phulgirkar, S. Patel, S.K. Manohar, Flexible, all-organic chemiresistor for detecting chemically aggressive vapors, J. Am. Chem. Soc. (2012). doi:10.1021/ja300420t.
- [7] J.W. Han, B. Kim, J. Li, M. Meyyappan, A carbon nanotube based ammonia sensor on cellulose paper, RSC Adv. (2014). doi:10.1039/c3ra46347h.
- [8] J.W. Han, B. Kim, J. Li, M. Meyyappan, A carbon nanotube based ammonia sensor on cotton textile, Appl. Phys. Lett. (2013). doi:10.1063/1.4805025.
- [9] I. V. Zaporotskova, N.P. Boroznina, Y.N. Parkhomenko, L. V. Kozhitov, Carbon nanotubes: Sensor properties. A review, Mod. Electron. Mater. (2016). doi:10.1016/j.moem.2017.02.002.
- [10] D. Wen, Y. Liu, C. Yue, J. Li, W. Cai, H. Liu, X. Li, F. Bai, H. Zhang, L. Lin, A wireless smart UV accumulation patch based on conductive polymer and CNT composites, RSC Adv. (2017). doi:10.1039/c7ra10789g.
- [11] L.R. Shobin, S. Manivannan, Carbon nanotubes on paper: Flexible and disposable chemiresistors, Sensors Actuators, B Chem. (2015). doi:10.1016/j.snb.2015.06.030.
- [12] P. Teerapanich, M.T.Z. Myint, C.M. Joseph, G.L. Hornyak, J. Dutta, Development and improvement of carbon nanotube-based ammonia gas sensors using ink-jet printed interdigitated electrodes, IEEE Trans. Nanotechnol. (2013).

- doi:10.1109/TNANO.2013.2242203.
- [13] S.J. Kim, J.W. Han, B. Kim, M. Meyyappan, Single Walled Carbon Nanotube Based Air Pocket Encapsulated Ultraviolet Sensor, ACS Sensors. (2017). doi:10.1021/acssensors.7b00585.
- [14] R.J. Chen, N.R. Franklin, J. Kong, J. Cao, T.W. Tombler, Y. Zhang, H. Dai, Molecular photodesorption from single-walled carbon nanotubes, Appl. Phys. Lett. (2001). doi:10.1063/1.1408274.

CHAPTER 5: SURFACE MODIFICATION OF BAMBOO IN EPOXY

COMPOSITES

5.1 Abstract

Bamboo fibers (BFs) have very good mechanical properties and are a candidate

reinforcement for epoxy matrix composites. However, to achieve improved performance, good

fiber-matrix interaction is required in BF reinforced composites. In this work, unidirectional long

BF reinforced epoxy composites at fiber volume content of 22%, 40% and 50% were made by

compression molding. A sodium hydroxide (NaOH) treatment process was used to modify the

surface of the BFs in the matrix. Flexural coupons for unidirectional BF/epoxy composites made

with 40v% NaOH modified BF showed an improvement of 29% and 26% for flexural modulus

and strength, respectively, compared to the untreated BF/epoxy composites. Additional

improvement in mechanical properties was achieved after the NaOH modified BF was coated with

graphene oxide (GO). 40v% NaOH/GO modified BF composites exhibited a considerable increase

of 43% and 29% for flexural modulus and strength, respectively, compared to the 40v% untreated

BF composites. Surface modification of the BF after the NaOH and NaOH/GO was confirmed by

scanning electron microscopy (SEM) and X-ray photoelectron spectroscopy (XPS). This BF

surface modification approach with NaOH/GO has the potential to increase the use of sustainable

plant fibers as alternatives to synthetic fibers.

Keywords: Unidirectional composites; Bamboo fiber; Surface Treatment; Graphene

Oxide; Epoxy Composite; Fiber/matrix adhesion;

123

5.2 Introduction

Bamboo fibers compared to other natural fibers are an excellent candidate which can be used as reinforcements in polymer composites [1] because of the widespread availability of bamboo species globally, their rapid growth of up to 21 cm per day, their mechanical properties and durability and their abundant availability [2].

In general, 40% of the bamboo culm accounts for fibers, while 50% is parenchyma (ligneous matrix) and 10% is conducting tissue [3,4]. Fiber bundles (technical fibers) can be extracted from the culm by a mechanical process, chemical process or a combination of both techniques. The fiber bundle is composed of elementary tubular fibers that have hexagonal and pentagonal cross sectional shapes, with a small hole in the middle called lumen [2], as shown in Figure 5.1. Elementary fibers can have diameters from 10 to 40 μ m and length from 1.0 to 4.3 mm, with lumen sizes from 2 to 20 μ m [2].

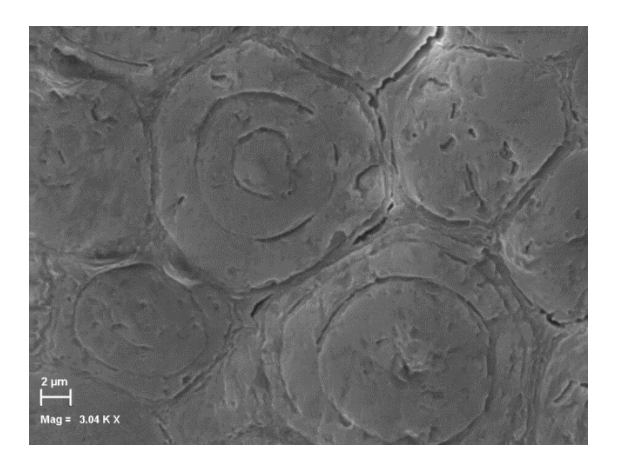


Figure 5.1: SEM of polished surface of cross section of bamboo fiber bundle embedded in epoxy.

The Young's modulus of the technical bamboo fiber varies from 19 to 43 GPa and strength varies from 341 to 860 MPa depending on the species, growth conditions, etc. [2]. However, the

hydrophilic nature of the BFs may lead to weak bonding between the fibers and the relatively hydrophobic polymer matrices, which can negatively impact the mechanical properties of the composites [5]. In addition, the presence of hemicellulose and lignin, which are noncellulosic materials, can lower the crystallinity and affect the properties of natural fibers [6]. Therefore, many surface modification have been reported to improve the interfacial adhesion between the composite constituents, with alkali treatment being one of the simplest and most effective methods [7].

Alkali treatment using sodium hydroxide (NaOH) solutions is one of the most common methods for treating bamboo fiber bundles [8] and can enhance not only the interfacial adhesion between natural fibers and polymeric matrices but also the mechanical, physical and thermal properties of the fibers [9,10]. This treatment promotes solubilization of hemicellulose and lignin [8,11] and separates the fibers into fibrils, which increases the available surface area of the fiber to be wet by the polymer matrix enhancing the interfacial bonding [10]. The treatment is also capable of increasing the chemical reactivity of the fiber by breaking hydrogen bonds and increasing the number of free hydroxyl groups [10,11]. Bonding in the composite interphase can also occur by mechanical anchoring since the treatment increases the roughness of the fiber surface [11].

Graphene is a two dimensional crystal with excellent mechanical, electrical, thermal and optical properties [12]. Graphene nanoplatelets are obtained by intercalation and exfoliation of natural graphite. After strong oxidation, single layers of graphene are reconstituted as graphene oxide. The surface of graphite oxide possesses many oxygen-containing groups that can be exfoliated in water, yielding individual sheets [13]. Exfoliated sheets containing one layer of carbon atoms like graphene are named graphene oxide (GO) [12]. GO has a mean lateral dimension of approximately 1 µm [14], with hydroxyl and epoxide groups on the basal plane, and carbonyl

and carboxyl groups along the sheet edge [12,15]. GO can be easily dispersed in water due to its hydrophilic nature caused by the presence of the polar oxygen functional groups [16] which also show good chemical reactivity. This assists in chemical functionalization and dispersion in polymer matrices to produce composites [14,17].

The use of GO and GO-derived graphene materials as a filler in polymer composites have increased the elastic modulus, tensile strength, electrical conductivity, and thermal stability of composites [16]. Defect-free graphene has a Young's modulus of 1.0 TPa and a fracture strength of 130 GPa, along with large interfacial area and high aspect ratio, therefore a small amount of filler is required to give good improvements [16]. By adding 0.7 wt% GO in poly(vinyl alcohol) (PVA) an increase of 62% in Young's modulus and 76% in tensile strength were achieved due to efficient load transfer between the GO and the matrix [18].

Many studies have been reported on the coating of synthetic fibers with GO to increase the mechanical and interfacial properties [6,19]. GO sheets were added in a sizing for carbon fiber reinforced epoxy composites and improvements on the tensile properties were obtained as well as an increase of 70.8% in the interfacial shear strength (IFSS) [6,20]. The covalent grafting of GO sheets onto glass fibers enhanced the strength and toughness of the composite interfacial region [21]. GO was also added in glass fabric/epoxy composites leading to an increase of 32.7% of the interlaminar shear strength [22].

In regards to natural fibers, alkali treated jute fibers (HA) were coated with varying concentration of GO (from 0.25 to 1 wt.%) [6] leading to an increase of their Young's modulus and tensile strength compared to untreated jute fibers (UT), as shown on Figure 5.2, as well as an increase in the IFSS in epoxy matrix.

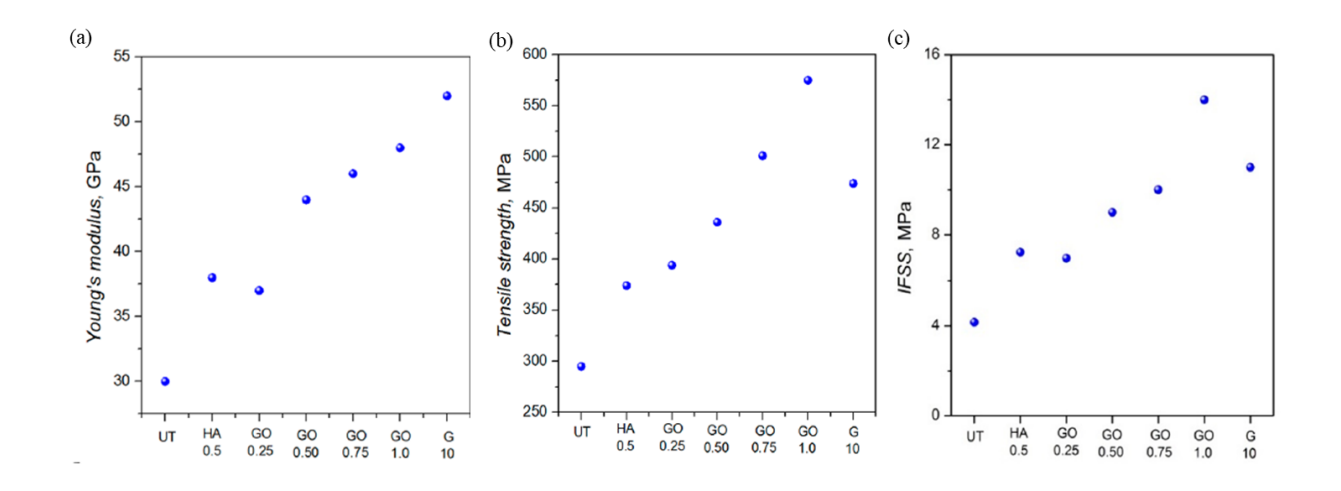


Figure 5.2: (a) Young's modulus, (b) tensile strength and (c) IFSS of untreated, GO-treated, and Graphene flake-coated jute fibers [6].

In this study, long BFs were surface treated with NaOH to improve their mechanical and interfacial properties for the preparation of unidirectional BF reinforced epoxy composites. To further improve the performance of the composites, alkali treated BF were coated with GO by a simple dipping technique. The effects of modifying the BF surface with NaOH and GO on the morphological, flexural and interfacial properties were investigated. The flexural modulus of the composites reinforced at 40v% BF has increased 29% and 43% after modifying the BF with NaOH and NaOH/GO, respectively. The flexural strength increased 26% and 29% after treating the BF with NaOH and NaOH/GO, respectively.

5.3 Experimental

5.3.1 Materials

Long bamboo fibers (15 - 25.4 cm) were obtained by a combination of a chemical and mechanical extraction technique and were kindly provided by Sunstrand Company. Their properties provided by the supplier are listed on Table 5.1. As received BFs were rinsed multiple time with deionized water (DI) and dried at 60° C for 3.5 h prior utilization.

Table 5.1: Bamboo Fiber Material Specifications.

Property	Value	
Density	$\rho = 1.4 \text{ g/cm}^3$	
Mean Fiber Diameter	$\emptyset = 256 \ \mu m$	
Mean Ultimate Tension Strength	$\sigma_{\rm UTS} = 451 \text{ MPa}$	
Mean Modulus of Elasticity	$E_T = 31 \text{ GPa}$	
Specific Strength	$\sigma_S = 322 \text{ MPa/(g/cm}^3)$	
Specific Modulus	$E_T = 22 \text{ GPa/(g/cm}^3)$	

NaOH was purchased from Avantor (Macron Fine Chemicals) and was chosen to treat the surface of BFs. GO in water was kindly provided by the University of Tennessee with a concentration of 2.8 mg/mL. The GO flakes possess lateral dimensions of approximately 1 µm and average thickness of approximately 1 nm that corresponds to 2–3 GO layers, and detailed information is provided elsewhere [23]. The epoxy matrix used was EPONTM resin 828 (viscosity

of 110 – 150 P at 25°C) supplied by Hexion Inc. and the curing agent was m-Phenylenediamine (mPDA) supplied by ACROS Organics.

5.3.2 Methods

5.3.2.1 Surface treatment of BFs with NaOH

BFs were soaked in 5 wt.% NaOH solution at room temperature for 5 h. The mass ratio of water and BFs was 30:1. The treated fibers were rinsed with DI water several time until reaching a neutral pH. The treated BFs were dried at room temperature for 20 h, followed by oven drying at 60 °C for 3.5 h. These fibers are identified NaOH modified BFs.

5.3.2.2 Surface treatment of NaOH modified BFs with GO

The NaOH modified BFs were immersed in the GO solution for approximately 34 min. The fibers were dried in vertical position in an oven at 80 °C for 35 min followed by drying at 60 °C for 3 h. These fibers are named NaOH/GO modified BFs.

5.3.2.3 Processing of unidirectional composites

Unidirectional composites were prepared by aligning BFs on the cavity of a mold and processing by compression mold (Carver Laboratory Press) as shown on Figure 5.3. Before making the composite, BFs were dried to remove moisture. The epoxy and curing agent were heated at 75°C, then mixed at a concentration of 14.5 phr mPDA and degassed in a vacuum oven. The mold containing the long BFs was also pre heated and degassed to remove trapped air in the mold. Then the resin system was carefully added into the mold to cover the BFs. The mold was closed, and the assembly was sealed with vacuum, which caused the excess resin to flow out of

the mold. The closed mold was transferred to the compression press for curing. Pressure was increased and the displacement and final thickness of the composite specimen was controlled by use of a rigid spacer. The composite plate was cured at 75°C for 2 h and postcured at 125°C for 2 h. The vacuum was vented after the first 5 min of compression. Cured composite plates were cut into coupons in the longitudinal direction of the fibers for flexural tests and conditioned in the laboratory atmosphere.

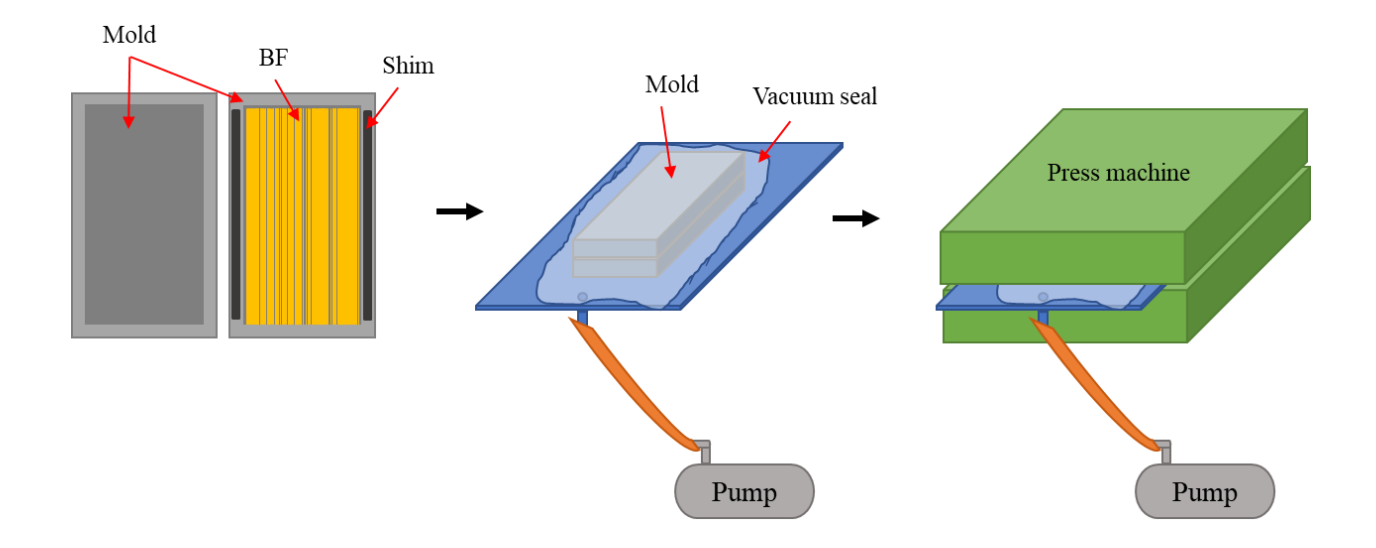


Figure 5.3: Processing of BF reinforced epoxy composite.

Composites were made with non-treated BF at fiber volume content of 22%, 40% and 50%. Based on the mechanical results, a fiber content of 40 vol.% was selected for the composites made of treated BFs. All the composites composition and the corresponding fiber surface treatment are shown on Table 5.2. Void content was below 6% and its effect among the composites seems negligible since they have similar void content.

Table 5.2: Composites composition and fiber surface treatment.

Composite name	Fiber volume content (%)	Fiber treatment
22 v% BF	22	None
40 v% BF	40	None
50 v% BF	50	None
40 v% NaOH modified BF	40	NaOH
40 v% NaOH/GO modified BF	40	NaOH and GO

5.3.3 Characterization methods

5.3.3.1 Scanning Electron Microscopy (SEM)

BFs, NaOH modified BFs and NaOH/GO modified BFs were examined with a Carl Zeiss Auriga FIB scanning electron microscope at an accelerating voltage of 5 keV. Fibers were mounted on the SEM sample holder on top of carbon tape. The fracture surface of flexural coupons was also observed. All samples were sputter-coated with tungsten to prevent surface charging.

5.3.3.2 X-ray photoelectron spectroscopy (XPS)

BFs, NaOH modified BFs and NaOH/GO modified BFs were characterized by XPS using a Physical Electronics 5400 ESCA. Survey spectra were collected at 187.85 eV pass energy and higher resolution spectra were collected with 29.35 eV pass energy. Prior to XPS investigation, NaOH/GO modified BFs were rinsed multiple time with DI water to remove physically bonded GO.

5.3.3.3 Flexural test

Flexural tests were conducted in an United Testing Systems SFM-20 load frame in general compliance to ASTM D790-10. The flexural tests used a 100 lbf or 1000 lbf load cell, a support span-to-depth ratio of 16:1 and the rate of crosshead motion was calculated per ASTM D790-10. The flexural samples had dimensions of approximately 77 x 12.7 x 2.3 mm. Tests were terminated at 5% strain (or before it if break occurred), and the flexural strength, flexural modulus and strain were calculated.

5.3.3.4 SBSS test

The composites were characterized by testing modified short beam shear specimens in a United Testing Systems SFM-20 load frame. A 1000 lbf load cell was used and the span-to-measured thickness ratio was set to 4:1. The specimen length was 6 times the thickness and the specimen width was 2 times the thickness as recommended by ASTM D2344/D2344M. Although samples are not multi-layer unidirectional specimens, they consist of unidirectional composites specimen test for SBSS and it is expected that they will experience same stress field.

5.4 Results and discussion

5.4.1 Characterization of surface treated BFs

Figure 5.4 displays SEM images of the surface morphologies of non-treated BFs, NaOH modified BFs and NaOH/GO modified BFs. Over 90% of the bamboo mass is cellulose, hemicellulose and lignin, with lesser concentrations of soluble polysaccharides, waxes, ashes and others [3,5]. As noted by the red arrows in Figure 5.4 (a), the surface of non-treated BFs has some

features, such as the presence of soft cells and soft parenchyma cells [3], which make the measurement of the fiber diameter more difficult [11].

As shown on Figure 5.4 (b), after the alkali treatment with NaOH solution, the surface materials (consisting of hemicelluloses, lignin, pectin, wax, and other impurities[6]) were partially removed making it easier to identify the single BFs. The surface of the BF became rougher due to the removal of the surface materials. This roughness may be beneficial to promote mechanical interlocking between the BF and the epoxy matrix and improve the adhesion [7,10]. It has been reported that treatment with excessive concentration of NaOH can remove cellulose and degrade the integrity of the fibers, resulting in decrease of the fiber strength [7]. Therefore, the treatment with 5 wt.% NaOH solution used in this work was effective in cleaning the surface without degrading the fiber mechanical properties.

The fibers that were coated with GO exhibited a similar surface morphology. The GO can be identified on the BF surface by the yellow arrows at the higher magnification micrograph in Figure 5.4 (c).

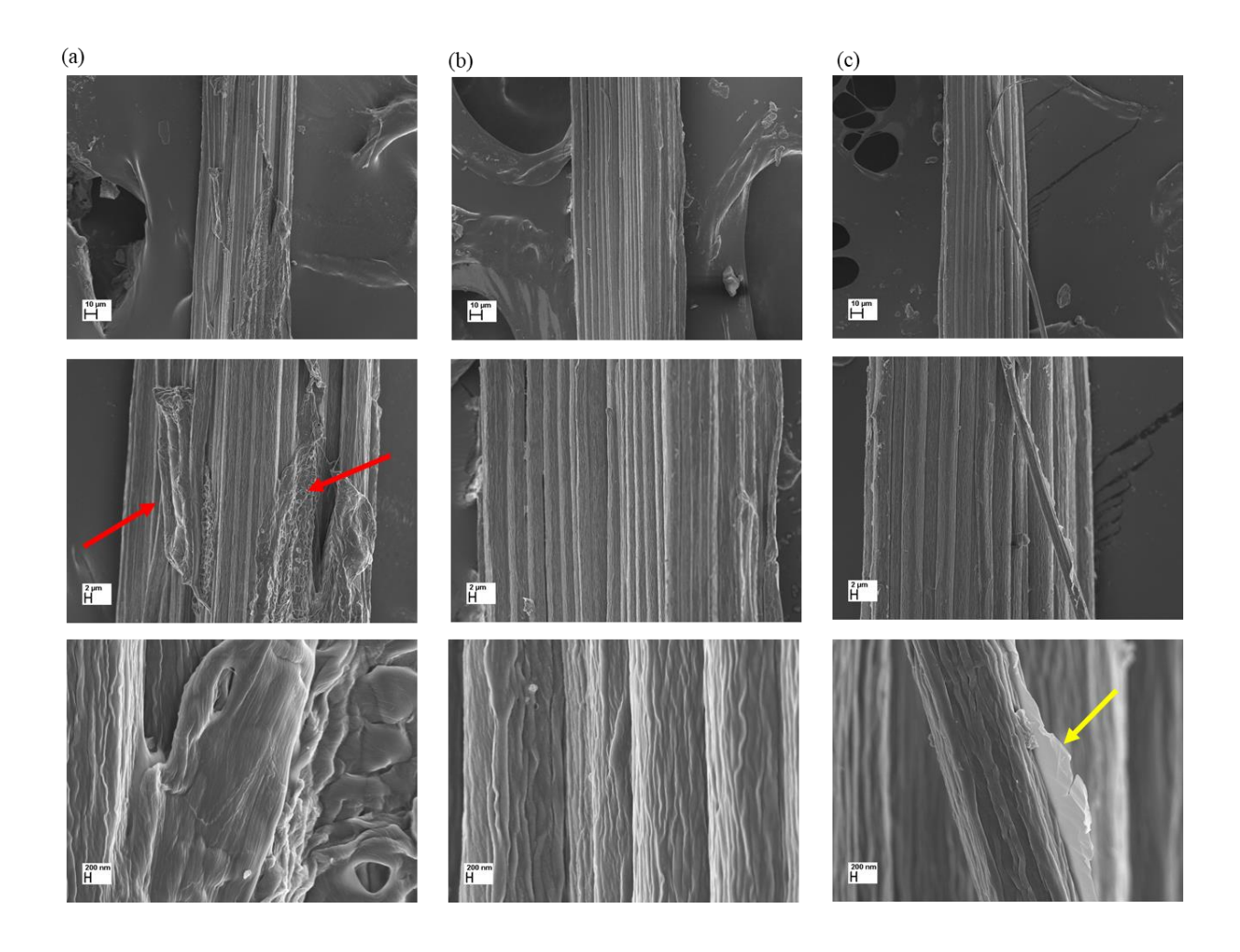


Figure 5.4: SEM images of the surface of (a) BFs, (b) NaOH modified BFs and (c) NaOH/GO modified BFs, top is lower magnification (377X) and bottom is higher magnification (9000X).

The surface chemical composition of BFs and the treated BFs was determined by XPS. The wide-scan survey spectra with elemental assignments are shown on Figure 5.5.

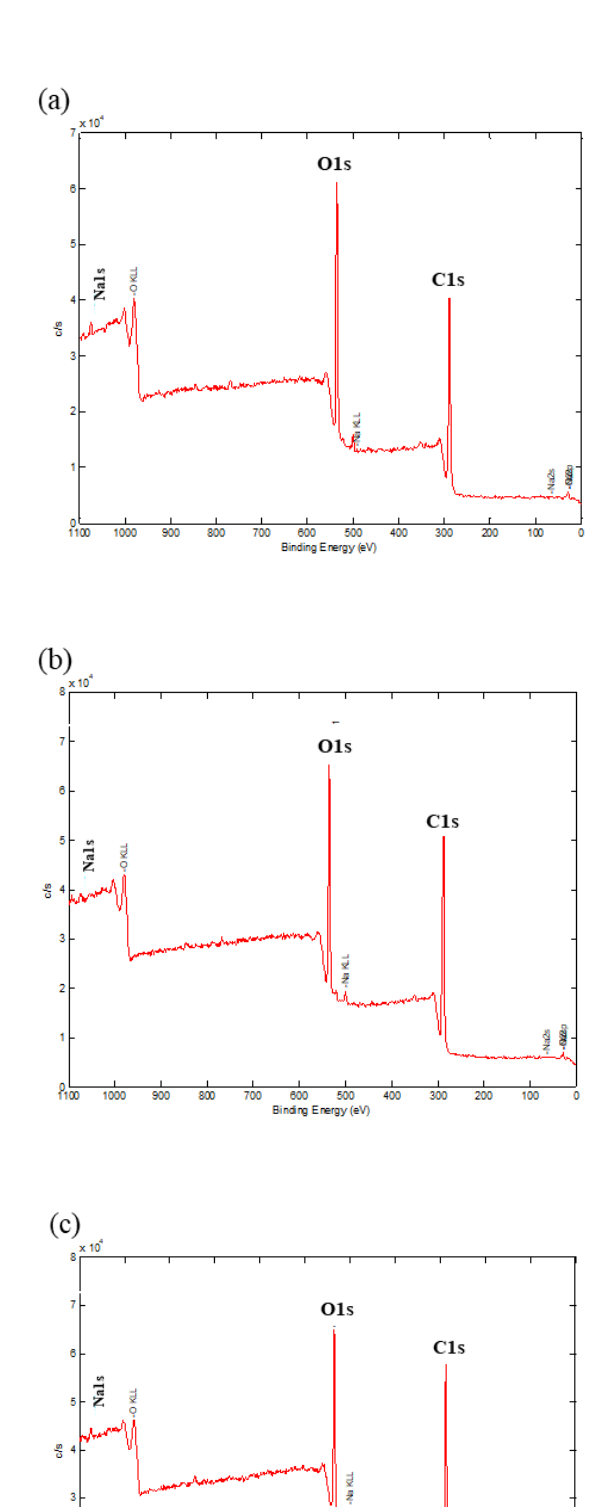


Figure 5.5: XPS survey of (a) BF, (b) NaOH modified BF and (c) NaOH/GO modified BF.

All the spectra exhibited the main BF surface constituent peaks assigned to carbon (C1s) and oxygen (O1s) and also detected a sodium peak (Na1s), due to the alkali treatment. Even the non-treated BFs have a small amount of Na (0.9%) resulting from the NaOH to extract the fibers from the bamboo culm at the supplier.

The elemental atomic composition and the carbon to oxygen ratio (C/O) of the fibers are summarized on Table 5.3. BFs had a carbon content of 65.5% that increased to 69.7% and 72.5% after treatment with NaOH and NaOH/GO, respectively. An increase on carbon content from $41.98\% \pm 0.13\%$ to $46.7\% \pm 0.11\%$ was observed on jute fiber after treating the fibers for 24 h with 0.5% NaOH [10].

As a result of the coating of the NaOH modified BFs with GO, the C/O ratio increases from 2.4 to 2.9 due to the presence of the GO (GO C/O ratio is approximately 3:1). Even after rinsing the NaOH/GO modified BFs multiple time with DI water, the change in the C/O ratio was detected, which indicates that GO reacted chemically with the BFs.

Table 5.3: Percent element composition for BF, NaOH modified BF and NaOH/GO modified BF.

Sample	C/O	C1s	O1s	Na1s	Ca2p
BF	2.0	65.5	32.9	0.9	0.6
NaOH modified BF	2.4	69.7	29.2	0.7	0.4
NaOH/GO modified BF	2.9	72.5	25.2	1.7	0.6

The deconvolution of C1s peak for BF, NaOH modified BF and NaOH/GO modified BF are given in Figure 5.6. Table 5.4 summarizes the relative amount of C1s components, which includes C1: C-C, C2: C-O and C3: O-C-O, C=O. The C1s spectrum of BFs and NaOH modified BFs are relative similar, while the surface modification with GO greatly changed the relative amount of C1s components. The C1 relative amount increased from 44.9% for BFs and 45.1% for NaOH modified BFs up to 68.7% for the NaOH/GO modified BFs. The increase in C1 can be assigned to the SP3 carbon of the GO. The intensity of C2 and C3 peaks decreased after coating the fibers with GO.

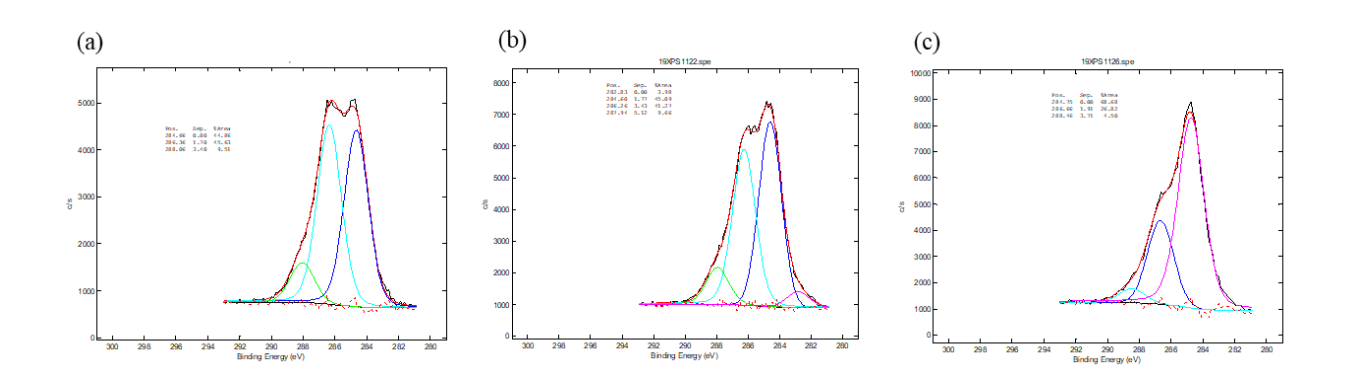


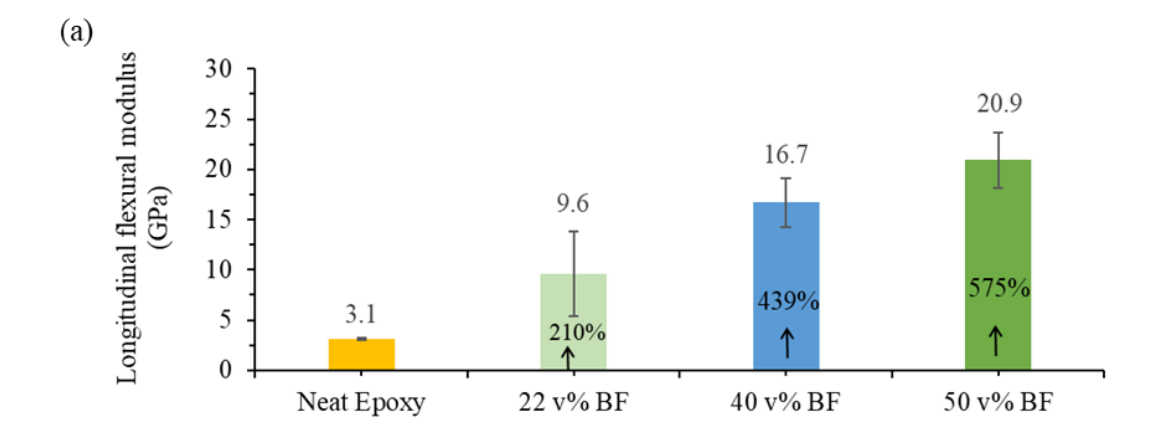
Figure 5.6: Deconvolution of C1s peak for (a) BF, (b) NaOH modified BF and (c) NaOH/GO modified BF.

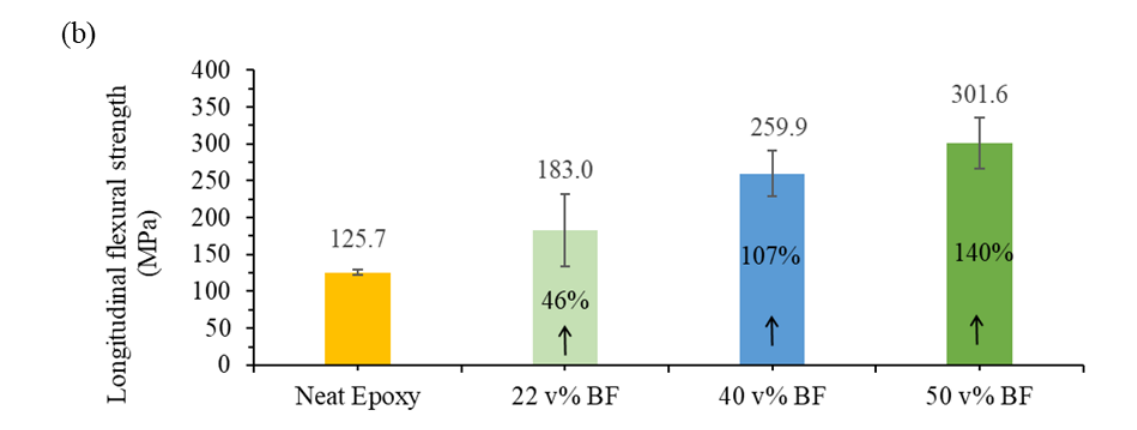
Table 5.4: Relative amount of C1s components (%) for BF, NaOH modified BF and NaOH/GO modified BF.

Sample	C1	C2	C3
BF	44.9	45.6	9.5
NaOH modified BF	45.1	41.3	9.7
NaOH/GO modified BF	68.7	26.8	4.5

5.4.2 Mechanical properties of BF reinforced epoxy composites at 22 v%, 40 v% and 50 v% BFs

Figure 5.7 shows the flexural properties along the fiber longitudinal direction for composites reinforced with untreated BFs at 22 v%, 40 v% and 50 v% compared to neat epoxy. The flexural modulus (Figure 5.7 (a)) and flexural strength (Figure 5.7 (b)) of all composites are superior compared to the neat epoxy, and as expected these properties increase with an increase in fiber content. A similar increase was noted by Takagi and Ichihara [24]. They combined short BFs into a starch-based resin and the flexural and tensile strength of the composites increase with increasing fiber content from 10 to 50 wt %. No significant difference for flexural strain (Figure 5.7 (c)) was observed among the composites.





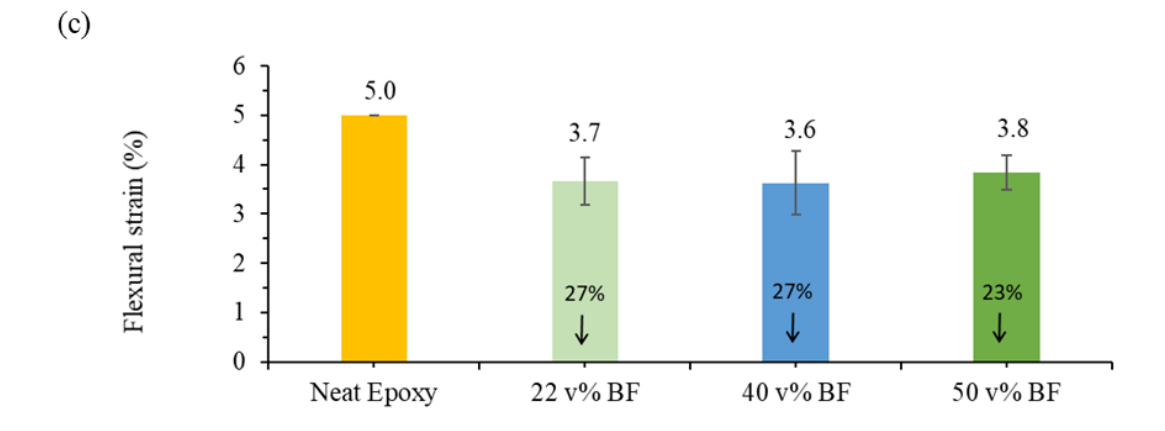


Figure 5.7: (a) Flexural modulus, (b) flexural strength and (c) flexural strain along the fiber longitudinal direction for neat epoxy and epoxy composites reinforced at 22 v%, 40 v% and 50 v% BF.

Composites with fiber volume greater than 50% were not made due to the possibility of excessive void formation during processing that could lower the mechanical properties, as observed by Thwe and Liao [25] who observed that the composite tensile strength can decrease at high BF content in polypropylene due to voids and micro crack formation under loading.

Epoxy matrix composite reinforced with BFs at 40v% were chosen for further investigation as this fiber content gave a considerable increase of 439% and 107% for flexural modulus and strength, respectively, compared to neat epoxy, with the lowest standard deviation among the composites.

5.4.3 Mechanical properties of NaOH and NaOH/GO modified BF reinforced epoxy composites at 40 v% BFs

Figure 5.8 shows the flexural properties of the composites reinforced with 40v% BF with different surface treatments. By treating the BFs with a solution of 5wt% NaOH, an increase of 29% and 26% in the composite flexural modulus and strength, respectively, was achieved compared to BFs without treatment. As show on the SEM images on Figure 5.4 (b), after the alkali treatment the fiber surfaces are relative clean of impurities, with no apparent damage and greater chemical reactivity due to the free hydroxyl groups. These advantages and greater surface roughness can all contribute to the interfacial bonding and mechanical interlocking into the epoxy matrix [5]. Moreover, the exposure of the fibers and greater surface area available after the alkali treatment also facilitate the impregnation of the fibers by the epoxy enhancing the interfacial bonding.

The increase in the composite mechanical properties for the NaOH modified BFs can also be attributed to an increase on the mechanical properties of the BF itself due to the alkali treatment.

Sarker et al. [6] observed that jute fibers after alkali treatment can easily rearrange themselves along the direction of a tensile force due to the removal of the non-cellulosic components that act as a constraint in the interfibrillar region of the fibers. As a result, when stretched the fibrils can better sustain and share the load between themselves and contribute to higher strength development [10]. This same behavior was observed by Zhang et. al [7] that showed that 2 wt.% NaOH treatment on BF had minimal effect on the tensile properties of BFs since the large amount of surface substances were preventing the fibrils from rearranging themselves along the direction of the tensile force during test. However, when they used higher concentration of NaOH of 6 wt.%, the tensile strength and the Young's modulus of the BFs were greatly increased due to the removal of the non-cellulosic components and increase of the cellulose crystallinity.

A slight reduction in the flexural strain Figure 5.8 (c) was observed for the alkali treated BFs reinforced composites. A reduction of extension of jute fibers during tensile testing was observed in other work [6] and it was possibly due to the removal of lignin from the intercellular region of jute fibers.

The composites made of fibers that were coated with GO exhibited the highest improvement on the mechanical properties at 43% and 29% for the flexural modulus and strength, respectively, compared to composites made of untreated BFs. The greater performance of NaOH/GO modified BF reinforced composites is related to the increased chemical bonding between the functional groups of GO and the alkali treated BFs, as was observed by SEM on Figure 5.4 (c) and the XPS results. The BFs coated with GO possess oxygen functional groups such as hydroxyl (-OH), epoxide (C-O-C), carbonyl (C=O) and carboxyl (O-C=O) that have the potential to chemically bond with the groups of the epoxy resin [6]. C-N bonds through ring opening polymerization may also occur with the amine curing agent (mPDA) [6]. In addition, since

GO possesses high modulus, its presence will stiffen the BFs [6] and consequently enhance the properties of the composites.

Overall, alkali treatment is a simple process to remove non-cellulosic components and impurities from the BF surface and increase the properties of the fiber for effective reinforcement of polymer composites. The alkali treatment also reduces the hydrophobicity of the fibers which may contribute to better interphase bonding [10]. The coating of NaOH treated BFs with GO is an alternative to further increase the mechanical properties, and the resulting reinforced epoxy composites showed considerable improvement in flexural modulus and strength.

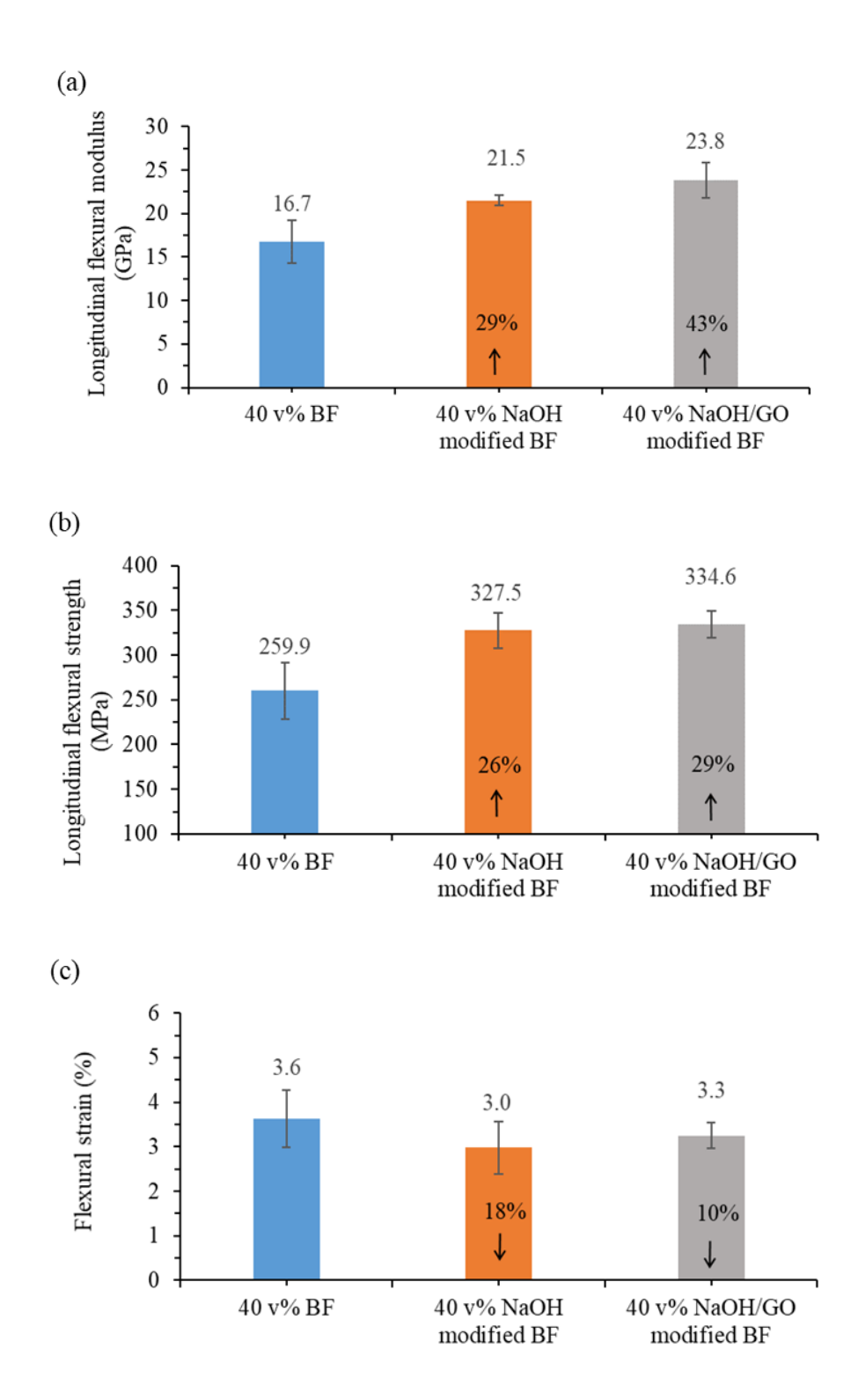


Figure 5.8: (a) Flexural modulus, (b) flexural strength and (c) flexural strain along the fiber longitudinal direction for epoxy composites reinforced at 40 v% BF, 40 v% NaOH modified BF and 40 v% NaOH/GO modified BF.

5.4.4 SEM observation of composites fracture surface

The fracture surfaces of the composites after flexural testing were analyzed by SEM revealing the presence of fiber pull out, some fiber breakage, brittle regions and relative good BF distribution as shown on Figure 5.9.

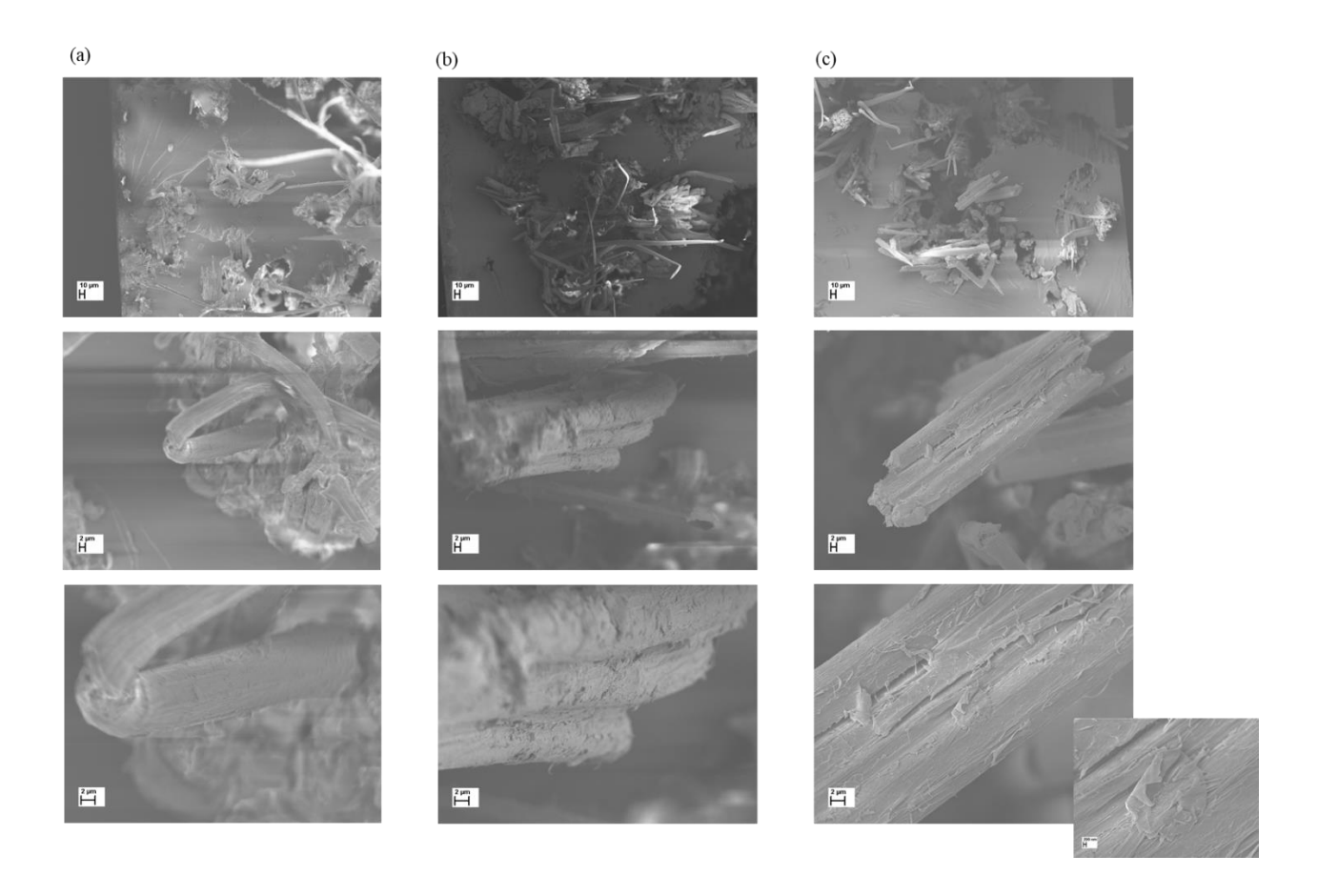


Figure 5.9: Flexural fracture surface for epoxy composites reinforced at (a) 40 v% BF, (b) 40 v% NaOH modified BF and (c) 40 v% NaOH/GO modified BF, top is lower magnification (177X) and bottom is higher magnification (2500X).

Figure 5.9 (a) reveals that composites reinforced with non-treated BFs exhibit little epoxy matrix adhering to the fiber surface, which is an indication of poor interfacial adhesion between the untreated fiber and matrix. Hydrophilic BF materials and impurities on the fiber surface does

not facilitate the bonding. Gaps, interfacial debonding and parenchyma cells can be clearly observed on Figure 5.10. Their presence helps explain the lowest mechanical properties for the composites reinforced with untreated fibers.

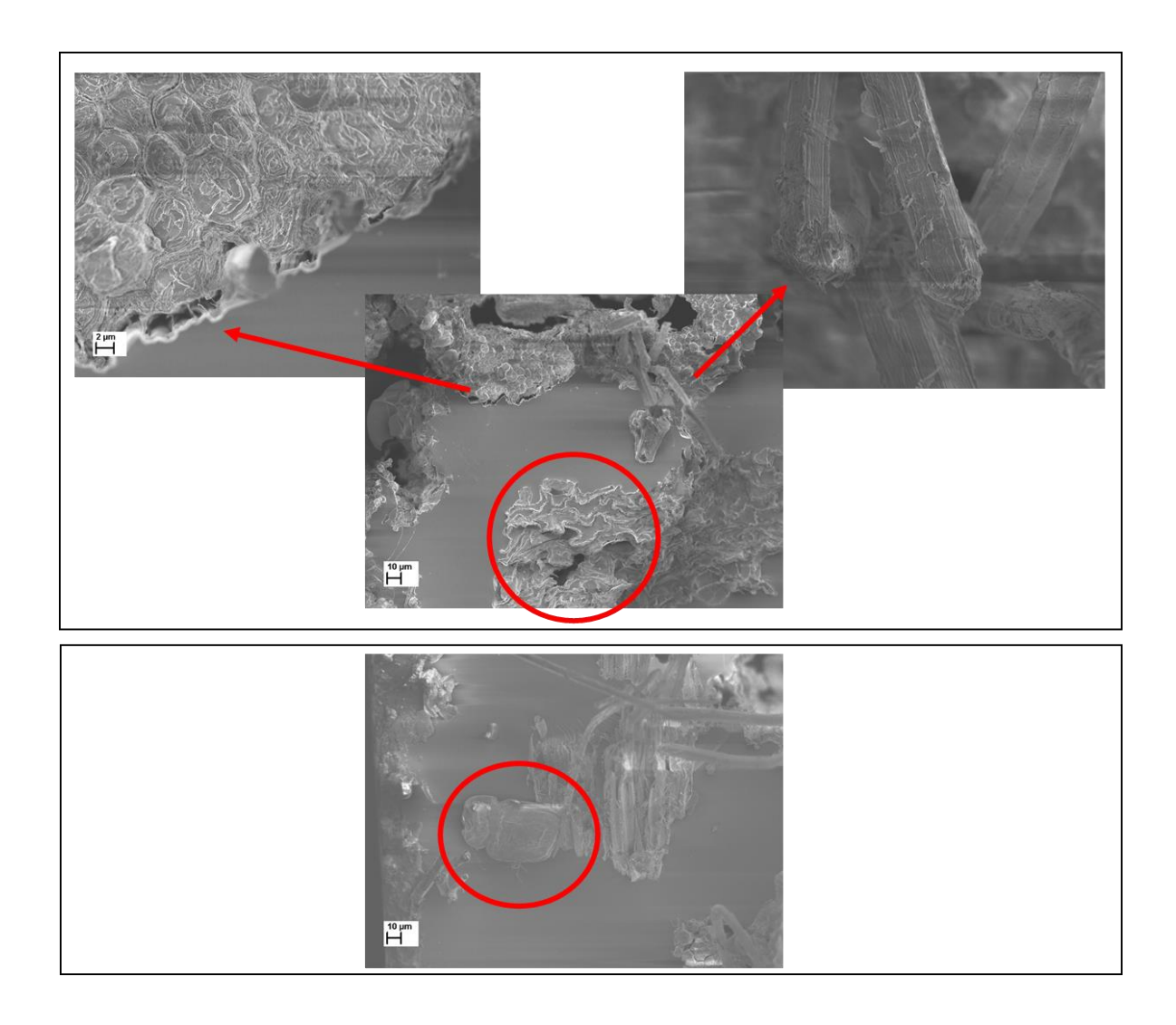


Figure 5.10: Flexural fracture surface for epoxy composites reinforced at 40 v% BF.

Figure 5.9 (b) shows composites reinforced at 40v% NaOH modified BF where considerable amount of epoxy resin can be observed covering the fiber surface. Alkali treated fibers have increased roughness for mechanical interlocking of the matrix as well cleaner surface and oxygen functional groups available for chemical reactions with the epoxy (as discussed in

section 5.4.3) and for improved interfacial bonding [7]. Figure 5.11 shows that the alkali treatment favors the exposure of fibrils facilitating the impregnation of the fibers with the epoxy matrix [11] that is correlated to the improvement in the composite mechanical properties compared to the untreated fiber reinforced composites.

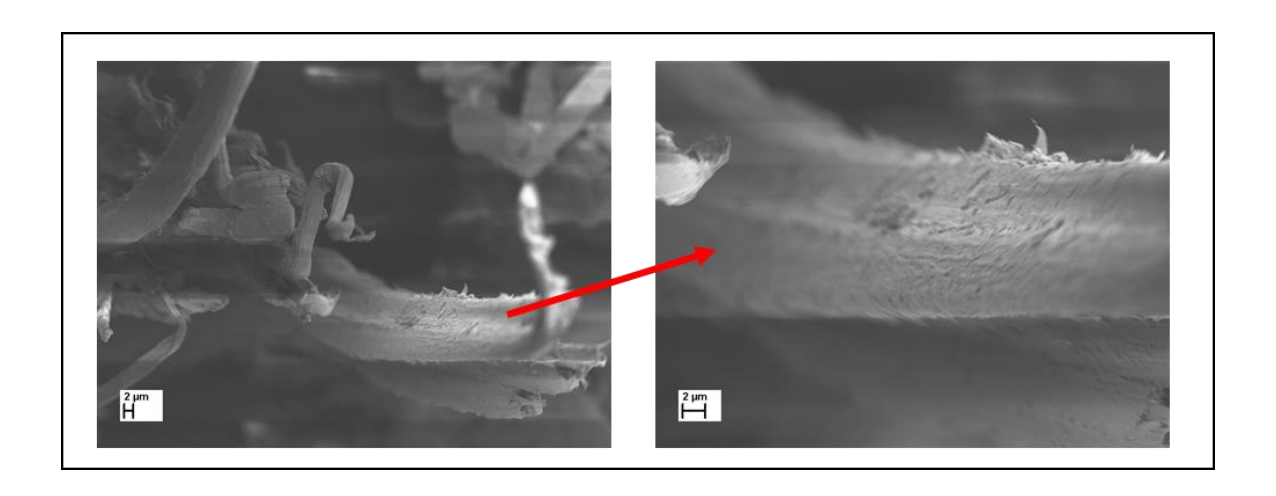


Figure 5.11: Flexural fracture surface for epoxy composites reinforced at 40 v% NaOH modified BF.

Although it is difficult to observe GO on the fracture surface of the 40v% NaOH/GO modified BF composite as shown on Figure 5.9 (c), a considerable amount of epoxy resin is noted on the fiber surface, which is an indication of good bonding between the fiber and the matrix.

Some GO peeling can be noted on Figure 5.12 and Wang et. al [19] also noted peeling and tearing of GO grafted on surface of carbon fiber reinforced epoxy composite during Mode I opening mode test that was beneficial for crack propagation resistance. By coating carbon fiber with GO and polydopamine (PDA), they observed that the crack propagated through the GO and PDA layers with tearing and peeling of GO sheets from fibers, which improved the load transfer effectiveness and absorbed more energy.

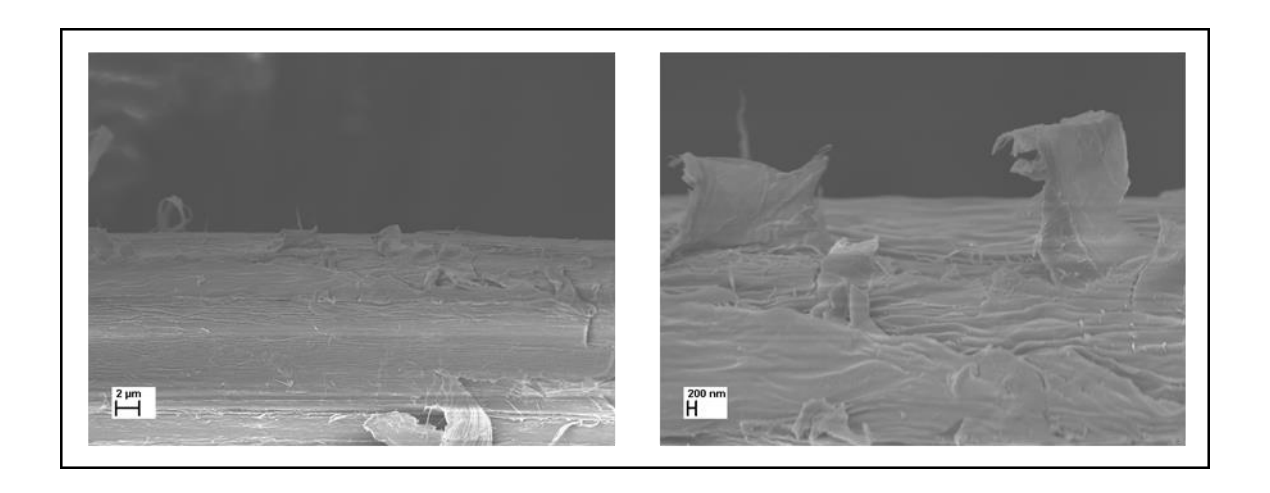


Figure 5.12: Flexural fracture surface for epoxy composites reinforced at 40 v% NaOH/GO modified BF.

Overall, the composite fracture surface observations are in agreement with the mechanical properties discussed on section 5.4.3.

5.4.5 Evaluation of the short beam strength

The short beam test is an efficient way to determine the shear strength on composites, which dictates the efficiency of the stress transfer from the matrix to the fibers and is correlated to the level of interfacial bonding. Figure 5.13 shows the short beam strength results for the composites made on this study.

The composites processed with non-treated BFs possess the lowest value of strength at 34.5 MPA due to the non-cellulosic components present on the fiber surface as discussed on the previous sections, that prevents a good interfacial bonding into the epoxy matrix. By treating the BFs with NaOH, the composites exhibited an increase of 14% compared to the composites with non-treated BFs. This increase is possibly attributed to the mechanical interlocking of the rougher fibers into the matrix.

Compared to 40v% BF reinforced composites, the 40v% modified NaOH/GO BF reinforced composites showed a slight increase of 6%. This may be due the low concentration of GO in water as low as 2.8 mg/mL, that was not sufficient to provide greater improvements. Sarker et. al [6] measured the IFSS at a jute fiber/epoxy matrix interface by single-fiber microbond pull-out test and showed that IFSS increases with the increase of GO concentration.

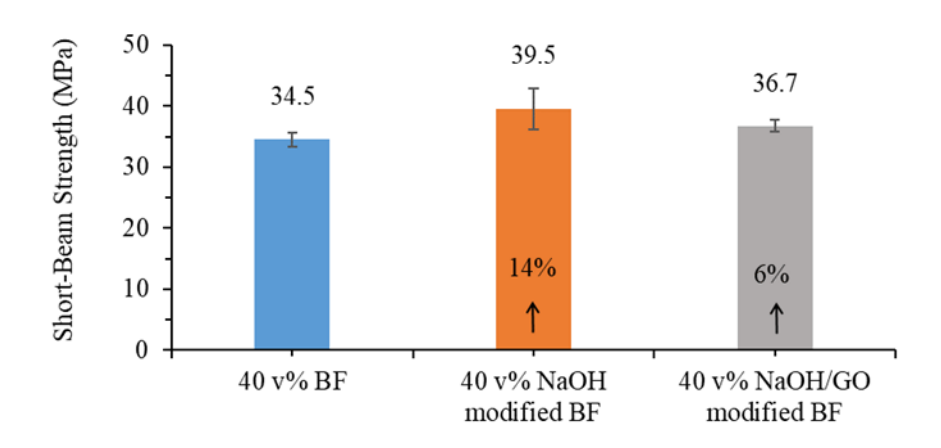


Figure 5.13: Short beam strength for epoxy composites reinforced at 40 v% BF, 40 v% NaOH modified BF and 40 v% NaOH/GO modified BF.

The increase on the short beam shear strength supports the conclusion that the treatment of the BFs with NaOH and GO enhances the interfacial properties, however, greater concentrations of GO could be more effective.

5.5 Conclusions

This work presents encouraging results for the treatment of BFs and their application as reinforcement for epoxy composites. BFs were treated with NaOH solution and then coated with GO. The mechanical properties of the corresponding composites reinforced with fiber volume

content of 40% were greatly improved. By treating the BFs with a solution of 5wt% NaOH, an increase of 29% and 26% on the composite flexural modulus and strength, respectively, was achieved compared to composites processed with BFs without the treatment. The composites made of fibers that were coated with GO exhibited the highest improvement on the mechanical properties at 43% and 29% for the flexural modulus and strength, respectively.

The alkali treatment removes hemicelluloses, lignin, pectin, wax, and other impurities from the fiber surface, opening up the fiber bundles to facilitate the impregnation with the polymeric resin, increasing the chemical reactivity with the free hydroxyl groups available to establish covalent bonding as well as increasing the surface roughness for better mechanical interlocking with the matrix. Consequently, better mechanical properties of the composite were achieved. GO further increased the composite performance due to the stiffening of the BFs and establishment of chemical bonding upon the oxygen functional groups on GO surface that chemically bond with the fibers and the groups of the epoxy resin. Fiber surface treatment was confirmed by XPS, and the SEM observations support the mechanical properties findings.

The BF natural fiber reinforced epoxy composites developed in this investigation offer a useful approach to reduce the utilization of synthetic fibers, produce a low density structural composite, made from a renewable resource, bamboo fibers. These BF composite materials have potential to be used in automotive industry (door panels, seat cushions, backrests, trim parts in dashboards) and household sectors (furniture and low cost housing materials) [1].

REFERENCES

REFERENCES

- [1] H. Banga, V.K. Singh, S.K. Choudhary, Fabrication and Study of Mechanical Properties of Bamboo Fibre Reinforced Bio-Composites, Innov. Syst. Des. Eng. 6 (2015) 84–98. http://citeseerx.ist.psu.edu/viewdoc/download?doi=10.1.1.823.1104&rep=rep1&type=pdf.
- [2] D.E. Depuydt, N. Sweygers, L. Appels, J. Ivens, A.W. van Vuure, Bamboo fibres sourced from three global locations: A microstructural, mechanical and chemical composition study, J. Reinf. Plast. Compos. (2019) 1–16. doi:10.1177/0731684419828532.
- [3] X. Wang, H. Ren, B. Zhang, B. Fei, I. Burgert, Cell wall structure and formation of maturing fibres of moso bamboo (Phyllostachys pubescens) increase buckling resistance, J. R. Soc. Interface. 9 (2012) 988–996. doi:10.1098/rsif.2011.0462.
- [4] L. Nayak, S.P. Mishra, Prospect of bamboo as a renewable textile fiber, historical overview, labeling, controversies and regulation, Fash. Text. 3 (2016) 2. doi:10.1186/s40691-015-0054-5.
- [5] H.P.S. Abdul Khalil, I.U.H. Bhat, M. Jawaid, A. Zaidon, D. Hermawan, Y.S. Hadi, Bamboo fibre reinforced biocomposites: A review, Mater. Des. 42 (2012) 353–368. doi:10.1016/j.matdes.2012.06.015.
- [6] F. Sarker, N. Karim, S. Afroj, V. Koncherry, K.S. Novoselov, P. Potluri, High-Performance Graphene-Based Natural Fiber Composites, ACS Appl. Mater. Interfaces. 10 (2018) 34502–34512. doi:10.1021/acsami.8b13018.
- [7] K. Zhang, F. Wang, W. Liang, Z. Wang, Z. Duan, B. Yang, Thermal and Mechanical Properties of Bamboo Fiber Reinforced Epoxy Composites, Polymers (Basel). 10 (2018) 608. doi:10.3390/polym10060608.
- [8] K. V, C. DP, K. S, K. K, Study on the Performance of Bamboo Fibre Modified with Different Concentrations of Sodium Hydroxide and Chlorine Containing Agents, J. Text. Sci. Eng. 08 (2018). doi:10.4172/2165-8064.1000362.
- [9] M.I. Ibrahim, M.Z. Hassan, R. Dolah, M.Z.M. Yusoff, M.S. Salit, Tensile behaviour for mercerization of single kenaf fiber, Malaysian J. Fundam. Appl. Sci. 14 (2018) 437–439. doi:10.11113/mjfas.v14n4.1099.
- [10] A. Roy, S. Chakraborty, S.P. Kundu, R.K. Basak, S. Basu Majumder, B. Adhikari, Improvement in mechanical properties of jute fibres through mild alkali treatment as demonstrated by utilisation of the Weibull distribution model, Bioresour. Technol. 107 (2012) 222–228. doi:10.1016/j.biortech.2011.11.073.
- [11] M.M.E. Costa, S.L.S. Melo, J.V.M. Santos, E.A. Araújo, G.P. Cunha, E.P. Deus, N. Schmitt, Influence of physical and chemical treatments on the mechanical properties of bamboo fibers, Procedia Eng. 200 (2017) 457–464. doi:10.1016/j.proeng.2017.07.064.

- [12] S. Pei, H.-M. Cheng, The reduction of graphene oxide, Carbon N. Y. 50 (2012) 3210–3228. doi:10.1016/j.carbon.2011.11.010.
- [13] J.I. Paredes, S. Villar-Rodil, A. Martínez-Alonso, J.M.D. Tascón, Graphene Oxide Dispersions in Organic Solvents, Langmuir. 24 (2008) 10560–10564. doi:10.1021/la801744a.
- [14] D.A. Dikin, S. Stankovich, E.J. Zimney, R.D. Piner, G.H.B. Dommett, G. Evmenenko, S.T. Nguyen, R.S. Ruoff, Preparation and characterization of graphene oxide paper, Nature. 448 (2007) 457–460. doi:10.1038/nature06016.
- [15] S. Stankovich, D.A. Dikin, R.D. Piner, K.A. Kohlhaas, A. Kleinhammes, Y. Jia, Y. Wu, S.T. Nguyen, R.S. Ruoff, Synthesis of graphene-based nanosheets via chemical reduction of exfoliated graphite oxide, Carbon N. Y. 45 (2007) 1558–1565. doi:10.1016/j.carbon.2007.02.034.
- [16] Y. Zhu, S. Murali, W. Cai, X. Li, J.W. Suk, J.R. Potts, R.S. Ruoff, Graphene and Graphene Oxide: Synthesis, Properties, and Applications, Adv. Mater. 22 (2010) 3906–3924. doi:10.1002/adma.201001068.
- [17] D.R. Dreyer, S. Park, C.W. Bielawski, R.S. Ruoff, The chemistry of graphene oxide, Chem. Soc. Rev. 39 (2010) 228–240. doi:10.1039/B917103G.
- [18] J. Liang, Y. Huang, L. Zhang, Y. Wang, Y. Ma, T. Guo, Y. Chen, Molecular-Level Dispersion of Graphene into Poly(vinyl alcohol) and Effective Reinforcement of their Nanocomposites, Adv. Funct. Mater. 19 (2009) 2297–2302. doi:10.1002/adfm.200801776.
- [19] P. Wang, J. Yang, W. Liu, X.-Z. Tang, K. Zhao, X. Lu, S. Xu, Tunable crack propagation behavior in carbon fiber reinforced plastic laminates with polydopamine and graphene oxide treated fibers, Mater. Des. 113 (2017) 68–75. doi:10.1016/j.matdes.2016.10.013.
- [20] X. Zhang, X. Fan, C. Yan, H. Li, Y. Zhu, X. Li, L. Yu, Interfacial Microstructure and Properties of Carbon Fiber Composites Modified with Graphene Oxide, ACS Appl. Mater. Interfaces. 4 (2012) 1543–1552. doi:10.1021/am201757v.
- [21] J. Chen, D. Zhao, X. Jin, C. Wang, D. Wang, H. Ge, Modifying glass fibers with graphene oxide: Towards high-performance polymer composites, Compos. Sci. Technol. 97 (2014) 41–45. doi:10.1016/j.compscitech.2014.03.023.
- [22] X.-J. Shen, L.-X. Meng, Z.-Y. Yan, C.-J. Sun, Y.-H. Ji, H.-M. Xiao, S.-Y. Fu, Improved cryogenic interlaminar shear strength of glass fabric/epoxy composites by graphene oxide, Compos. Part B Eng. 73 (2015) 126–131. doi:10.1016/j.compositesb.2014.12.023.
- [23] S. Hu, E.L. Ribeiro, S.A. Davari, M. Tian, D. Mukherjee, B. Khomami, Hybrid nanocomposites of nanostructured Co 3 O 4 interfaced with reduced/nitrogen-doped graphene oxides for selective improvements in electrocatalytic and/or supercapacitive properties, RSC Adv. 7 (2017) 33166–33176. doi:10.1039/C7RA05494G.

- [24] H. TAKAGI, Y. ICHIHARA, Effect of Fiber Length on Mechanical Properties of "Green" Composites Using a Starch-Based Resin and Short Bamboo Fibers, JSME Int. J. Ser. A. 47 (2004) 551–555. doi:10.1299/jsmea.47.551.
- [25] M.M. Thwe, K. Liao, Effects of environmental aging on the mechanical properties of bamboo–glass fiber reinforced polymer matrix hybrid composites, Compos. Part A Appl. Sci. Manuf. 33 (2002) 43–52. doi:10.1016/S1359-835X(01)00071-9.

CHAPTER 6: SUMMARY AND FUTURE WORK

6.1 **Summary**

The research presented in this dissertation investigated cellulose fibers in its various forms from the nano-level to the macro-level as a potential ecofriendly alternative to replace synthetic fibers in reinforced composites. Cellulose fiber was investigated at the macro scale as the main reinforcement in a polymer matrix composite and at the nanoscale (CNCs) as a reinforcement at the polymer-composite interphase. Cellulose fibers by themselves made into a cellulose paper were investigated as a substrate for flexible electronics. This study showed that cellulose in all of its forms, can effectively reinforce different polymer matrices such as thermosetting (epoxy) and thermoplastic (PP) targeting different applications as well as being useful for flexible sensors.

Chapter 2 investigated how functionalized CNCs can be used as a sizing agent to increase the interfacial adhesion between CF and epoxy in composites. An increase in the IFSS was achieved for CFs sized with APTES-CNCs as well as an improvement in the failure mode as detected by the birefringent stress pattern seen during the SFFT. This supports the assumption that adding the APTES-CNCs at the composite interphase greatly enhances the stress transfer from the matrix to the fiber. CFs sized with APTES-CNCs at a concentration of 1.0 wt% resulted in the highest increase on IFSS of 77% and 81% for 12k tow sized CF and individually sized CF, respectively, compared to unsized CFs. This beneficial enhancement on IFSS was achieved by the establishment of covalent bonding coupled with an increase of the modulus at the composite interphase.

Mechanical, thermal and morphological properties of hybrid composites of celluloseinorganic fibers targeting automotive applications were investigated and reported in Chapter 3. In general, inorganic reinforcing fibers led to the greatest improvements in mechanical properties. However, hybridizing an optimum concentration of cellulose fiber with inorganic reinforcement in the composite showed a positive effect and an opportunity to reduce or even replace a portion of the inorganic fibers in some automotive applications. Hybrid composites with 15 wt% SGF and 15 wt% Cellulose B exhibited a 58% and 171% increase in tensile stress and modulus, respectively, compared to neat PP Z, producing a composite material suitable for body interior (console substrate, wiring harness) and under-the-hood (battery and power distribution box covers) applications. Hybrid composites are more thermally stable than the neat PP, which may offer an opportunity for hybrid composites made of cellulose to be considered for challenging under-the-hood applications. The T_c of these composites also increased compared to the neat PP, due to the fibers acting as nucleating agents, which can increase the rate of part production.

Chapter 4 investigated CNT based UV sensors that were fabricated on flexible cellulose paper substrates. Sensors fabricated on cellulose paper respond immediately to UV On/Off cycle, and can also operate without losing functionality after being mechanically bent. Results show that cellulose has the potential to be part of electronic devices and provide advantages in terms of low cost, lightweight, ecofriendly and disposable characteristics.

Unidirectional long bamboo fiber reinforced epoxy composites were fabricated at a 40% fiber volume content and their mechanical properties were investigated in Chapter 5. The results show that the treatment of BFs with a solution of NaOH greatly improves the composite flexural modulus and flexural strength by 29% and 26%, respectively, compared to composites processed with non-treated BFs. Greater improvement of 43% and 29% for the composite flexural modulus and flexural strength, respectively, is achieved by adding GO at the BFs surface. The fracture surface observation of the composites by SEM is in agreement with the mechanical properties

showing that treated BFs have more resin attached to their surface meaning better impregnation of the epoxy and better interfacial bonding, while non-treated BFs are relative clean of resin which is an indication of lower adhesion. Therefore, the treatments developed on this work were beneficial for the development of natural fiber reinforced epoxy composites.

6.2 Future work

6.2.1 Sizing CF with APTES-CNC

The sizing of CF with APTES-CNC was shown to produce benefical composite interfacial properties. One area of concern is that the increase in the interphase modulus by itself can lower the strain to failure, which would tend to embrittle the material. However, the insertion of nanoparticles at the interphase is a balance to increase the composite modulus and to provide crack deflection which can improve the toughness. Future work should be undertaken to investigate these two effects simultaneously. Improving the uniformity of the sizing, investigating the optimum content of the APTES-CNC on surface of coated CFs and relating the IFSS improvement to other composite mechanical properties would be a significant contribution to the composite field.

6.2.2 Adding compatibilizer to hybrid composites

SEM observation of the fracture surface of hybrid composites showed good fiber distribution, however due to the inherent lack of compatibility between cellulosic fibers and polymeric matrices such as PP, the use of a compatibilizer is recommended as future work to improve the adhesion of the fiber to the PP matrix. This can lead to even greater mechanical and thermal performance of the hybrid composites. Thus, a method to functionalize the cellulose fiber by adding chemical groups to its surface or adding a compatibilizer during the processing, such as

maleic anhydride, should be developed. With such a development, the potential for facilitating chemical bonding between the cellulosic fiber and the matrix could lead to improved mechanical properties of the composite.

6.2.3 Improving recovery time of UV sensors

Although the sensors developed in this study proved to be effective for detecting UV light, there still may be opportunities for improvement in the recovery time of the sensors. A polymer membrane to encapsulate the sensor and inhibit gas exchange with the external environment, could be added to the sensor configuration. An investigation to determine the improvement in the time for full recovery to the baseline should be conducted. Factors that need to be investigated include both the variability of the paper composition and the variability of cellulose fiber arrangement during the paper making process to assess their impact on the UV response.

6.2.4 Increasing the concentration of GO on BF reinforced epoxy composites

The insertion of GO as a coupling agent between the BF and the polymer matrix showed a slightly increase of 6% for the SBSS in 40v% BF reinforced composites. Future investigations should seek to determine the optimum GO concentration in the coating solution through determination of the effect of the GO concentration and functionalization on the interfacial bonding of the BFs into the matrix as well as on the composite mechanical properties such as the transverse properties (flexural strength at 0 ° direction) and fracture toughness to assess the level of adhesion between the coated BFs and the epoxy matrix.